HYDROPHOBIC, FLUORINATED SILICA XEROGEL FOR LOW-k APPLICATIONS

Zhengping Zhang, B.S.

Dissertation Prepared for the Degree of

DOCTOR OF PHILOSOPHY

UNIVERSITY OF NORTH TEXAS

May 2004

APPROVED:

Richard F. Reidy, Major Professor
Dennis W. Mueller, Co-Advisor
Nandika D'Souza, Committee Member and
Graduate Advisor
Mohamed El Bouanani, Committee Member
Michael J. Kaufman, Chair of the Department of
Materials Science and Engineering
Oscar N. Garcia, Dean of the College of
Engineering
Sandra L. Terrell, Interim Dean of the Robert B.
Toulouse School of Graduate Studies

Zhang, Zhengping, Hydrophobic, fluorinated silica xerogel for low-k applications., Doctor of Philosophy (Materials Science and Engineering), May 2004, 122 pp., 12 tables, 59 illustrations, references, 164 titles.

A new hydrophobic hybrid silica film was synthesized by introducing one silicon precursor (as modifiers) into another precursor (network former). Hybrid films have improved properties.

Hydrolysis and condensation of dimethyldiethoxysilane (DMDES) (solvent (EtOH) to DMDES molar ratio R = 4, water to DMDES molar ratio r = 4, 0.01 N HCl catalyst) was analyzed using high-resolution liquid ^{29}Si NMR. It was found that after several hours, DMDES hydrolyzed and condensed into linear and cyclic species.

Films from triethoxyfluorosilane (TEFS) have been shown to be promising interlayer dielectric materials for future integrated circuit applications due to their low dielectric constant and high mechanical properties (i.e., Young's modulus (E) and hardness (H)). Co-condensing with TEFS, linear structures from DMDES hydrolysis and condensation reactions rendered hybrid films hydrophobic, and cyclic structures induced the formation of pores.

Hydrophobicity characterized by contact angle, thermal stability by thermogravimetric analysis (TGA), Fourier transform Infrared spectroscopy (FTIR), contact angle, and dynamic secondary ion mass spectroscopy (DSIMS), dielectric constant determined by impedance measurement, and mechanical properties (E and H) determined by nanoindentation of TEFS and TEFS + DMDES films were compared to study the effect of DMDES on the TEFS structure. Hybrid films were more hydrophobic and thermally stable. DMDES incorporation affected the dielectric constant, but showed little enhancement of mechanical properties.

ACKNOWLEDGMENTS

The funding for this research provided by the Texas Advanced Technology Program is gratefully acknowledged.

I give my deep thanks to my advisor Dr. Richard Reidy for his continual support and encouragement throughout my graduate study. Thank him for his patience and understanding for all my mistakes. Moreover, I am grateful to Dr. Reidy and Dr. Dennis Mueller for their insightful advice and discussions.

I would like to acknowledge the people for their kind help while I carried out my experiments: Dr. Phil Matz (TI), Dr. B.P. Gorman (Dept. Phys., UNT), Dr. Huiping Jia (Max) (UT Dallas), Mrs. Georgeanne (UT Arlington), Miss Padma, and Mr. Suman (Engineering College, UNT), Miss Haritha (Engineering College, UNT), Miss Marylin (Dept. Chem., UNT). Thank you all for your kind help.

I would like to acknowledge all the members in the research group. Thank you for maintaining an amicable team environment for me. I would like to thank Dr. Mohamed Bouanani for his time and teaching in NRA analysis and Dr. Nandika D'Souza for her valuable advice.

Finally, I would like to express my appreciation to my wife Jing Wang and friends for their love and support. Without them, I would not have been so successful in this endeavor.

TABLE OF CONTENTS

Page

Chapter

LIST OF TABLES

LIST OF ILLUSTRATIONS

CHAPTER 1

INTRODUCTION

1.1 Sol-Gel Processing

Sol-gel processing is a wet chemistry method to synthesize inorganic and / or organic-inorganic hybrid materials mixed at a molecular level [1]. It has attracted sustained attention for more than two decades primarily because of homogeneous and highly pure products, and low processing temperatures [2]. Usually sol-gel processing involves dissolving a precursor into a solvent or solvents to generate colloidal suspensions ("sol") that are subsequently converted into gels and then processed to desired shapes or structures [3]. In principle, sol-gel processes have five stages including: hydrolysis, condensation (polymerization), gelation, aging, and drying. However, some of these steps are quite difficult to separate. In fact, for most precursors, several steps are interwoven, such as hydrolysis and condensation that makes the detailed kinetic analysis very difficult or impossible.

Sol-gel processing has several intrinsic advantages, which include lower processing temperature, higher purity products, molecular level mixing, ease to fit different shapes, and mild chemical conditions. Some disadvantages are often expensive precursors, large-scale limitations, and long reaction times [3]. As more precursors have become available at lower prices, sol-gel methods have gained wider application. Sol-gel products can be formed into monoliths, powders, films, and single- or multi-component fibers. This method has been used to produce high temperature superconductor and ferroelectrics, nonlinear optics, ultraviolet photonics [4]. Due to the possible mild chemistries in sol-gel processing, it has been used to encapsulate biological species such as RNA, DNA, antibodies, enzymes or even whole cells into porous materials, bridging the gap between ceramic and biomaterials [5, 6]. Various other applications include: biosensors, membranes, optical coatings, and hard coatings on plastics [7].

For the past two decades, the common silicon precursors (tetramethoxysilane (TMOS) and tetraethoxysilane (TEOS)) have been intensively studied. Complicated reaction sequences with overlapping hydrolysis and condensation occur in these systems; however, six different exchange reactions can be used to generally describe this sol-gel process [1].

- Hydrolysis:

$$\equiv \mathrm{Si-OR} + \mathrm{H_2O} \xrightarrow{k_h} \equiv \mathrm{Si-OH} + \mathrm{ROH} \qquad (1)$$

- Esterification:

$$\equiv \mathrm{Si-OH} + \mathrm{ROH} \xrightarrow{k_e} \equiv \mathrm{Si-OR} + \mathrm{H_2O} \qquad (2)$$

- Water-producing condensation:

$$\equiv \mathrm{Si-OH} + \mathrm{HO-Si} \equiv \xrightarrow{k_{cw}} \equiv \mathrm{Si-O-Si} \equiv + \mathrm{H_2O} \qquad (3)$$

- Alcohol-producing condensation:

$$\equiv \mathrm{Si-OH} + \mathrm{RO-Si} \equiv \xrightarrow{k_{ca}} \equiv \mathrm{Si-O-Si} \equiv + \mathrm{ROH} \qquad (4)$$

- Siloxane hydrolysis:

$$\equiv \mathrm{Si-O-Si} \equiv + \mathrm{H_2O} \xrightarrow{k_{sh}} \equiv \mathrm{Si-OH} + \mathrm{HO-Si} \equiv \qquad (5)$$

- Siloxane alcoholysis:

$$\equiv \mathrm{Si-O-Si} \equiv + \mathrm{ROH} \xrightarrow{k_{sa}} \equiv \mathrm{Si-OH} + \mathrm{RO-Si} \equiv \qquad (6)$$

where R is an organic functional group (e. g., R = CH_3, C_2H_5) and the reaction of only one group for each silicon atom is shown in each equation.

The kinetic constants for $R'_nSi(OR)_{4-n}$ hydrolysis are defined as (R', R = CH_3, C_2H_5 or F):

$$R'_nSi(OR)_{4-n} + H_2O \xrightarrow{k1} R'_nSi(OR)_{3-n}(OH) + ROH$$

$$R'_nSi(OR)_{3-n}(OH) + H_2O \xrightarrow{k2} R'_nSi(OR)_{2-n}(OH)_2 + ROH$$

and so on. In principle, for each silicon atom, more than one functional group can participate in one of these six reactions.

In addition to type of precursor, many other parameters such as solvent type and concentration, water concentration, temperature, catalyst type and concentration and even the catalyst-adding sequence can affect hydrolysis / condensation rates and the final products [8].

1.2 Organic / Inorganic Hybrid (Ormosils)

Ormosil stands for <u>or</u>ganically <u>mo</u>dified <u>sil</u>icates. One of the most attractive features of sol-gel processing is that it is a viable pathway to prepare numerous types of new organic / inorganic hybrid materials which are either extremely difficult or impossible to synthesize by other processes [9]. By introducing non-cleavable organically bonded units into inorganic matrix, the organic and inorganic components can be chemically connected. When silica is the inorganic matrix from sol-gel process, the products are called Ormosils (organically modified silica).

There are several ways to prepare Ormosils. It is convenient if at least one precursor includes a chemically bonded organic group that can survive sol-gel processing. In the silicon precursor family ($R'_nSi(OR)_{4-n}$, R' and R can differ), organic group-bearing precursors can have one organic group (methyltriethoxysilane (MTES), methyltrimethoxysilane (MTMS), etc.), two organic groups (dimethyldiethoxysilane (DMDES), dimethyldimethoxysilane (DMDMS), etc.) and three organic groups (trimethylmethoxysilane (TMMS), etc.). When precursors having non-cleavable silicon carbon bonds are introduced into other matrix-forming precursors to undergo sol-gel processing, these organic moieties will be preserved in the gel and open a new door for sol-gel processing applications, including optics, microelectronics.

Usually silica matrix-forming precursors are TEOS and TMOS. TEOS and TMOS both have four functional groups undergoing hydrolysis and condensation. To form three dimensional silica networks, a minimum of three hydrolyzable and condensable functional groups is needed. Theoretically both $R'Si(OR)_3$ and $Si(OR)_4$ can be a silica matrix former, no matter what R' is. A variety of R' can be used to further modify silica matrix, such as fluorine in triethoxyfluorosilane (TEFS, $FSi(OC_2H_5)_3$).

1.3 Low-k Films

Interconnect technology is a core technology for integrated circuit development. As the device feature sizes shrink, interconnect delays have become comparable to or even exceeding the intrinsic delays of the transistors. To alleviate these issues, the insulating materials between metal lines must have lower dielectric constants to make the effective k values low ($k_{eff} = (1 - \rho)\, k_{dense} + \rho\, k_{pore}$, k_{eff} is effective dielectric constant, k_{dense} is fully dense material dielectric constant, k_{pore} is the dielectric constant for materials in the pores, and ρ is the porosity (pore volume versus total sample volume)). Low-k interlayer dielectrics (ILD) reduce parasitic capacitance, crosstalk, power dissipation, and RC delay that can limit IC features.

The dielectric constant, k, is the ratio of the permittivity of a substance to that of free space [10]. High dielectric constant, k, arises from of dipole formation including electronic polarization (bound electrons around ion cores are distorted and lead to polarization), ionic polarization (electric field distorts ion positions and temporarily creates dipoles), and orientation polarization (molecule have non-uniform electron density distribution) contributions. Accordingly, there are two possible ways to reduce k: decreasing dipole strength or the number of dipoles, which means to use lower density or lower polarizability materials.

Following that rule, numerous materials with k's ranging from k = 2 – 3 (dense polymers or porous inorganic/organic films) to k = 3 – 3.6 (fluorinated silica) have been successfully demonstrated. However, only a limited number of candidates have been introduced into production line due to the integration and reliability issues. Xerogels are a unique class of porous silica dielectrics that offer tunable porosity that is dependent on the pore size and distribution. Since porosity influences the effective dielectric constant and pore diameter affects mechanical strength, porosity and pore size must be optimized for both reliability and performance.

1.4 Low-k at UNT

A new silicon precursor - triethoxyfluorosilane (TEFS) was chosen as a fluorinated silica low-k precursor. Spin-on films from this precursor have low dielectric constant (k = 2.2 as deposited) and robust mechanical properties (Young's modulus E = about 12 GPa, hardness H = about 1 GPa) [11].

Fluorinated silica films from TEFS are hydrophilic. Measurements determined a contact angle of about 35° using deionized (DI) water as test liquid. So low-k films from TEFS will absorb moister and make effective k values increase.

Dimethyldiethoxysilane (DMDES) is another silicon precursor. DMDES itself will not gel because each silicon atom has two bonds terminated by methyl groups so it cannot form a three-dimensional network. Using high-resolution liquid ^{29}Si NMR, hydrolysis and polymerization products of DMDES with acid catalyst were determined. It is found that after hydrolysis and condensation of DMDES for a period of time, two species are formed: linear and ringed structures [12]. Each linear structure has two hydroxyl (OH) groups, which may connect the linear structure onto SiO_2 network, giving silica matrix hydrophobicity. And the ring structures can be used as nano-templating agent to affect pore size.

1.5 References

1. C.J. Brinker, and G.W. Scherer, Sol-Gel Science: the Physics and Chemistry of Sol-Gel Processing, Academic Press, San Diego, 1990.
2. L.L. Hench, and J.K. West, Chem. Rev. 90 (1990) 33.
3. J.D. Wright, and N.A. Sommerdijk, Sol-Gel Materials, Chemistry and Applications, Gordon and Breach Science Publisher, 2001.
4. D.R. Ulrich, J. Non-Cryst. Solids, 121 (1990) 465.
5. W. Jin, and J.D. Brennan, Analytica Chimica Acta, 461 (2002) 1.
6. I. Gill, Chem. Mater., 13 (2001) 3404.
7. D.R. Uhlmann, and G. Teowee, J. Sol-Gel Sci. Techn., 13 (1998) 153.

8. H. Dong, PhD dissertation, Dept. of Materials Science and Engineering, Univ. of North Texas, 2003.
9. J.D. Mackenzie, and E.P. Bescher, J. Sol-Gel Sci. Techn., 13 (1998) 371.
10. D. Shamiryan, T. Abell, F. Lacopi, and K. Maex, Materialstoday, 1 (2004) 34.
11. B.P. Gorman, R.A. Orozco-Teran, J.A. Roepsch, H. Dong, D.W. Mueller, and R.F. Reidy, App. Phys. Lett., 79 (2001) 410.
12. Z. Zhang, B.P. Gorman, H. Dong, Rosa A. Orozco-Teran, D.W. Mueller, and R.F. Reidy, J. Sol-Gel Sci. Techn., 28 (2003) 159.

CHAPTER 2

HYPOTHESIS

Triethoxyfluorosilane (TEFS) low-k films have low dielectric constants and robust mechanical properties, but hydrophilic from contact angle measurements. Dimethyldiethoxysilane (DMDES) itself cannot form a gel but develops linear and ringed species after hydrolysis and condensation. The purpose of this work is to show that DMDES hydrolysis and condensation products introduced into a TEFS matrix make the resulting silica with low dielectric constant, mechanically robust, and hydrophobic.

Under high-resolution liquid ^{29}Si nuclear magnetic resonance (NMR), linear and ringed structures from DMDES pregelation under acid catalyst were determined. Each linear structure has two functional groups, which can connect the linear structure onto the SiO_2 network. Methyl groups in linear structures can render SiO_2 network hydrophobic. Ringed structures are inert and have specific diameter. Ringed structures can be used as nano-templates to affect the pore size.

To evaluate viability, experiments were conducted to determine DMDES pregelation time and optimal DMDES to TEFS molar ratio. Film properties from DMDES + TEFS composite were compared with TEFS films including hydrophobicity, thermal stability, calculated k values, and mechanical properties (E and H).

CHAPTER 3

LITERATURE REVIEW

3.1 Kinetics of Alkoxysilane

3.1.1 Kinetics of Tetralkoxysilanes

Several models for the early stage of hydrolysis and condensation of tetralkoxysilanes, specifically, tetramethoxysilane (TMOS) and tetraethoxysilane (TEOS) have been proposed. By changing the water to alkoxide ratio (r), Pouxviel et al. analyzed the early stages of acid-catalyzed TEOS hydrolysis and condensation using ^{29}Si nuclear magnetic resonance (NMR) [1]. These experiments were conducted at moderate water concentration (r = 4) and assumed that during the initial stage of hydrolysis water concentration was constant. This assumption described first order kinetics for each hydrolysis step; thus, the rate constant ratios were estimated to be: $k_2 / k_1 = 5$, $k_3 / k_1 = 12$, and $k_4 / k_1 = 5$, showing that the hydrolysis rate is strongly affected by the degree of substitution of the monomers. The global hydrolysis and condensation kinetic constants were: $k_H = 1.4 \times 10^{-1}$ (for short time) and $k_C = 1.5 – 6.4 \times 10^{-2}$ l (mol hr)$^{-1}$ (for long time). After assigning the NMR peaks to different species, they found that non-hydrolyzed monomer (TEOS) did not participate in polymerization. Assink et al. [2] analyzed TMOS hydrolysis and water-producing and alcohol-producing condensation reactions under acid catalyst by changing the r values and found that the hydrolysis rate constant was greater than 0.2 liter / (mol hr)$^{-1}$, which is slightly larger than reported by Pouxviel. The water-producing and alcohol-producing condensation rate constants were determined to be 0.006 and 0.001 liter / (mol hr)$^{-1}$, respectively. However, under similarly catalyzed TEOS sol-gel systems, the water-producing condensation rate constant is more than 20 times greater than the alcohol-producing condensation rate constant [3].

Jaglid et al. analyzed the hydrolysis of TEOS in methanol solutions under base catalyst [4]. By following specific peak integrated area changes, they determined that the first hydrolysis constant was approximately 0.33 liter/(mol hr)$^{-1}$. In order to follow the water-producing and alcohol-producing condensations, Chojnowski et al. dissolved TEOS, H_2O and HCl in dilute dioxane solutions and, using ^{29}Si NMR, deduced the hydrolysis and condensation rates [5]. Using initial concentrations of [HCl] = 0.5 × 10^{-2} M (mole per liter), [TEOS] = 1.5 M, r = 0.73, ethanol to TEOS ratio (R) = 2, the hydrolysis and condensation kinetic constants were: k_1 = 1.5 × 10^{-3}, k_2 = 2.5 × 10^{-2}, k_3 = 0.72, k_4 = 1.46, water-producing condensation k_{WC} = 0.51, and alcohol-producing condensation rate k_{AC} = 0.1 × 10^{-2} l / (mol sec)$^{-1}$. Some other kinetic constants and assumptions used are tabulated in Table 1.

Table 1: Summary of TEOS and TMOS hydrolysis data

Literature data summary for the hydrolysis of TEOS or TMOS at room temperature			
Authors	Assumptions	initial system compositions	rate constants for monomer and intermediates hydrolysis
Aelion et al.[6]	global hydrolysis without reversibility	[TEOS]: 0.21 M	k_H = 0.374 l / (mol hr)
		[H_2O]: 1.2 M	
		[HCl]: 1.6×10^{-3} M	
		in dioxane solution	
Yang at al[7]	pseudo first order without reversibility	[TEOS]: 1.89 M	k_1 = 0.86 hr^{-1}

		$[H_2O]$: 7.57 M	$k_2 = 3.84$ hr^{-1}
		[HCl]: 9.6×10^{-4} M	$k_3 = 17.4$ hr^{-1}
		in ethanol solution	$k_4 = 78$ hr^{-1}
Pouxviel et al.[8]	a particular set of reactions	[TEOS]: 1.95 M	$k_1 / k_{-1} = 0.26 / 0.026$ l /(mol hr)
		$[H_2O]$: 7.8 M	$k_2 / k_{-2} = 1.36 / 0.082$ l /(mol hr)
		[HCl]: 5.1×10^{-4} M	$k_3 / k_{-3} = 5.12 / 0.34$ l /(mol hr)
		[EtOH]: 7.4 M	$k_4 / k_{-4} = 9.22 / 1.54$ l /(mol hr)
Ro et al.[9]	statistic with irreversible condensation	[TEOS]: 9.3 M	$k_1 / k_{-1} = 0.328 / 0.014$ l /(mol hr)
		$[H_2O]$: 1.6 M	$k_2 / k_{-2} = 0.282 / 0.026$ l /(mol hr)
		[HCl]: 10-3 M	$k_3 / k_{-3} = 0.164 / 0.042$ l /(mol hr)
		[EtOH]: 7 M	$k_4 / k_{-4} = 0.082 / 0.056$ l /(mol hr)
Kay and Assink[2, 10, 11]	statistic without reversibility	[TMOS]: 2.24 M	$k_1 = 48$ l /(mol hr)
		$[H_2O]$: variable	$k_2 = 36$ l /(mol hr)
		[HCl]: 1.6×10^{-3} M	$k_3 = 24$ l /(mol hr)
		in methanol	$k_4 = 12$ l /(mol hr)
Sanchez and McCormick[12]	reversibility without pseudo first order	[TEOS]: 2.07 M	$k_1 / k_{-1} = 0.35$ / - (>50) l /(mol hr)
		$[H_2O]$: 4.15 M	$k_2 / k_{-2} = 1.56 / 0.06$ l /(mol hr)
		[HCl]: 5.04×10^{-4} M	$k_3 / k_{-3} = 11.5 / 1.7$ l /(mol hr)
		[EtOH]: 7.94 M	$k_4 / k_{-4} = 22.4 / 8.2$ l /(mol hr)
		[TMOS]: 3.32 M	$k_1 / k_{-1} = 0.35$ / - (>50) l /(mol hr)
		$[H_2O]$: 6.25 M	$k_2 / k_{-2} = 0.71$ / - (>50) l /(mol hr)
		[HCl]: 1.47×10^{-4} M	$k_3 / k_{-3} = 1.42 / 0.12$ l /(mol hr)
		[MeOH]: 10.96 M	$k_4 / k_{-4} = 4.53 / 1.55$ l /(mol hr)

3.1.2 Hydrolysis and Condensation of Dimethyldiethoxysilane (DMDES)

Using high-resolution ^{29}Si NMR, hydrolysis and condensation of DMDES were studied under various conditions: pH values, r, solvent type and R, etc.

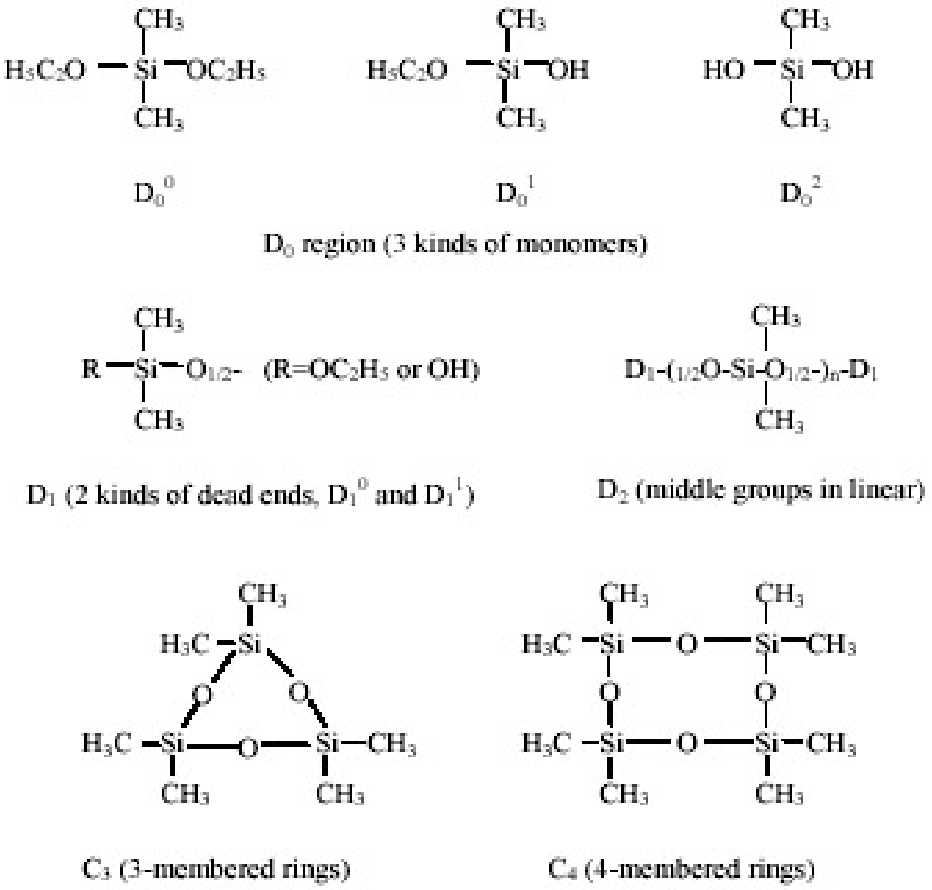

Figure 1: Notations used in the dissertation to describe DMDES species

Using high resolution ^{29}Si NMR and varying water to DMDES ratios (r) and acidic catalyst concentration, Sugahara et al. studied the DMDES hydrolysis and initial condensation behavior [13]. They found that at r = 4, DMDES hydrolyzed and condensed as follows:

- a large concentration of fully hydrolyzed monomer, D_0^2, was built up,
- dimer D_1^1 - D_1^1 was formed,
- dimer D_1^0 - D_1^1 and trimer D_1^1 - D^2 - D_1^1 occurred,
- trimer D_1^0 - D^2 - D_1^1 and tetramer D_1^1 - D^2 - D^2 - D_1^1 appeared,
- later cyclic trimer C_3 and cyclic tetramer C_4 developed.

Lux et al. identified the signals up to 7 – 8 silicon atoms by combining D_1 and D_2 ^{29}Si NMR spectra [14, 15]. They stated that the hydrolysis ratio and pH values strongly affected the nature and the proportion of the species formed. Higher acid catalyst concentrations (lower pH values) made the monomers disappear more rapidly and more cyclic tetramers C_4 formed. Alam used Distortionless Enhancement of Polarization Transfer (DEPT) heteronuclear polarization transfer pulse sequence to assign the ^{29}Si NMR peaks [16]. Instead of using acidic catalyst, Suda et al. analyzed the effects of sodium ions on the hydrolysis and condensation of DMDES and found that ^{29}Si NMR signals shifted with time [17]. They believed that the shift depended on both OH^- and Na^+ ion concentrations and was attributed to the exchange reaction between sodium ion and proton of Si – OH at pH values higher than 13.5. This exchange made sodium ions act as terminators and limited the whole polymerization. Table 2 summarizes the signal chemical shifts related to TMS.

Table 2: DMDES hydrolysis and polymerization species chemical shift summary

structures	Chemical shift (ppm)			
D_0^0	-2.4	-3.47		
D_0^1	-3.0	-4.03		-.379
D_0^2	-3.5	-4.47		-4.38
$D_1^{0(a)}D_1^{1(b)}$	(a): -11.6	(a): -12.53		(a): -12.50
	(b): -12.5	(b): -13.25		(b): -13.37
$D_1^1D_1^1$	-12.2	-12.92	-11.11	-13.05
C_3	-8.2	-8.86		-9.02
$D_1^{0(a)}D^{2(b)}D_1^{1(c)}$	(a): -11.7	(a): -12.57		(a): -12.67
	(b): -21.0	(b): -21.56		(b): -21.84
	(c): -12.8	(c): -13.47		(c): -13.71
$D_1^{1(a)}D^{2(b)}D_1^1$	(a): -12.4	(a): -12.95	(a): -11.98	(a): -13.25
	(b): -20.7	(b): -21.46	(b): -20.11	(b): -21.72
C_4	-18.8	-19.44		-19.69
$D_1^{1(a)}D^{2(b)}D^2D_1^1$	(a): -12.8	(a): -13.42	(a): -12.14	(a): -13.67
	(b): -21.3	(b): -21.84	(b): -21.00	(b): -22.12
sources	Sugahara et al.[13]	Lux et al.[14, 15]	Harris et al.[18]	Suda et al.[17]

To quantify the hydrolysis and polymerization kinetics of DMDES and its intermediates in acidic conditions, Hook conducted a series of experiments to compare the alkyl group and alkoxy group effects [19]. He found that the hydrolysis of SiOR to SiOH generally causes a downfield shift because the electronegativity of the oxygen is decreased due to OH having an ionic character greater than OR. But some factors other than inductive effects led to the trend to higher fields upon successive hydrolysis of DMDES. Methyl groups on silicon atoms could increase the rate of initial hydrolysis by seven times (one substituted methyl group, MTES) and twenty five times (two methyl groups, DMDES) faster than TEOS. For initial condensation, the trend was the same, - an increase of methyl groups on silicon atoms could increase the condensation rate by three times (one substituted methyl group, MTES) and eleven times (two methyl groups, DMDES) compared to TEOS. Inductive effects were thought to cause the trend: methyl group was a weak electron donor while the ethoxy group is a mild electron acceptor. Sequential substitution of ethoxy groups by methyl groups would lead to a decrease in partial positive charge on silicon atoms. This decrease could consequently increase the degree of protonation and lead to faster hydrolysis. Condensation and hydrolysis can influence each other. Faster hydrolysis can cause faster condensation. And the inductive effects ensure that, as more methyl groups are bound to a silicon atom, the protonated intermediates become more stable, and the condensation rate is increased. In steric terms, fewer ethoxy groups can decrease the bulkiness and make it easier for condensation. It was found that the second substitution of an ethoxy by a methyl group did not have the same pronounced effects on hydrolysis and condensation as the first substitution. By including non-random branching, cyclization, and reversibility effects, Rankin et al. systematically studied the methyl-substituted ethoxysilane [20]. Several striking features were deduced: hydrolysis reached steady state, both hydrolysis and condensation were accelerated by methyl substitution, and methyl groups facilitated ring structure formation.

3.2 Hybrid Materials (Ormosils)

For ormosils, both Si – C and Si – O bonds coexist through sol-gel processing from silicon alkoxides. Unhydrolyzable organic groups can behave as not only network modifiers, but also network formers if they are polymerizable under certain conditions. Such hybrid materials bear unique properties and open a new door for a wide range of applications: scratch resistant coatings, micro-porous materials, and optical matrices [21].

Due to the unlimited possible combinations of precursors, precursor relative ratios, solvent and / or water concentrations, and catalyst, products with enhanced properties (decreasing the brittleness of silica films, hydrophobicity, meso- or micro-porosity), and, more importantly, products that are difficult or even impossible to achieve using conventional ceramic processing now can be routinely synthesized. Sol-gel based hybrid materials are the subject of intense interest by industrial and academic groups [22, 23]. Three types of hybrid materials have been reported:

- type I: co-polymerization of $R'Si(OR)_3$ and $Si(OR)_4$ [22,24];
- type II: polymerization of $(OR)_3\,Si\,R''Si(OR)_3$ [25];
- type III: polymerization of $R'Si(OR)_3$ [26]

where the organic groups R′ and R″ can be varied in length (e.g., CH_3, C_3H_7, etc.), rigidity (e.g., phenyl, acetyl, etc.), or functionality (e.g.,CH_2CH_2CN, $CH_2CH_2CH_2NHCH_2CH_2NH_2$, etc.) [27].

Difunctional alkoxides such as DMDES cannot act as network formers due to insufficient functionalities to form three-dimensional networks. But its tendency to form chains can be used to provide some flexibility to the oxide network. DMDES can render the network hydrophobic, a property that can repel polar solvents such as water out of the gel network. This repellant effect can make sequential drying or heating unnecessary and avoid bulk sample shrinking or thick film cracking [21].

In a TEOS – MTES – DMDES system, Glaser et al. changed the relative ratios of the three precursors under acid catalyst [28]. They assumed that, although the initial reactivities of the individual precursor species were different, the reactivities for successive sites after one or more sites on a precursor had reacted could be equivalent, or at least on the same order of magnitude. Since each precursor has more than one functional group, over a period of time, there is a high probability of different components interconnecting or condensing. Under solid state ^{29}Si NMR, they found that, the overall degree of reaction for functionality (the ratio of OR groups to silicon atoms in precursor) less than 3.00 exhibited a consistently high value (> 96%) but for functionality greater than 3.00 showed a low value regardless of the initial precursor ratios. In a DMDES and TEOS system under acidic conditions, van Bommel et al. believed that the hydrolysis and condensation reaction rates of DMDES were far higher than the reaction rates of TEOS under the same conditions [29]. The higher hydrolysis rate of DMDES caused a lower degree of hydrolysis of TEOS, especially at short hydrolysis times. At longer hydrolysis times, secondary water from the result of strong self-condensation effects of DMDES silanols became available for the hydrolysis of TEOS and this caused the increase of gelation time. Babonneau et al. found that the organic modified network made of 1:1 molar ratio of TEOS to DMDES with acid catalyst was more condensed than pure silica gel and higher thermal stability under argon or air [30]. Using isopropanol (IPA) and tetrahydrofuran (THF) co-solvent and HCl catalyst, Iwamoto et al. found the signals from the co-polymerization of TEOS and DMDES under liquid ^{29}Si NMR [31]. Increasing reaction temperature from room temperature to 70°C could increase the condensation but the condensation was almost insensitive to water content in r changes from 2 to 4.

After pregeling DMDES / EtOH / H_2O (1:1:1 and pH = 1) for some time, Babonneau introduced DMDES into $Ti(OPr^i)_4$ and $Zr(OPr^n)_4$ precursors [21, 32]. Using ^{29}Si and ^{17}O NMR, both Si – O – Ti and Si – O – Zr bonds were found indicating co-condensation between DMDES and other precursors. In a DMDES and TEOS system, Si signal peaks at -11.5 ppm (corresponding to D_1 - Q) and -16.5, -18.8, and -20.1 ppm (corresponding to Q - D_2 - Q or D - D_2 - Q) were observed in liquid ^{29}Si NMR spectra. Brus et al. verified ab-initio calculations for DMDES – TEOS co-condensation using solid-state ^{29}Si NMR results [33].

To study the effects of DMDES additions to TEOS sol-gel processes, Mah et al. varied the amount of DMDES added to TEOS solutions and the DMDES pregeling time [34]. Under acid catalysis, small amounts of DMDES decreased the TEOS gelation time due to the rapid reaction of DMDES with TEOS and consequent suppression of cyclic species formation from TEOS. However, additional increases of DMDES increased TEOS gel times because of a decreased average functionality and increased concentration of cyclic species, both of which prevent the formation of siloxane networks. When the addition of DMDES was delayed, the DMDES – TEOS co-condensation was suppressed and heterogeneous reactions were promoted. By mixing DMDES and TEOS at the same time, De Witte et al. discovered that introduction of organic groups into the silica gel network caused a reduction of surface area, pore volume, and pore size distribution [35]. The maximum decrease occurred at DMDES to TEOS molar ratio of 10:90. The presence of methyl groups at the gel surface was proposed to reduce the capillary tension and prevent gel network collapse during drying. The initial decrease of surface area and pore volume for the gels was attributed to the reduction of the degree of network connectivity due to the incorporation of Si atoms with lower functionality. Methyl groups could make the resulting structure more flexible and possibly survive stronger contraction during drying. After a surface area and pore volume minimum, capillary tension dominated in determining the gel texture, which counteracted the effects of reduced network connectivity from methyl groups. At higher DMDES concentrations, more methyl groups were located at the gel surface, strongly influencing the interaction between the pore fluid and gel surface during drying. Methyl groups mainly affect the network connectivity when embedded in a silica network; however, methyl groups could only slightly modify the network connectivity at the gel surface as methyl groups replaced hydroxyl groups.

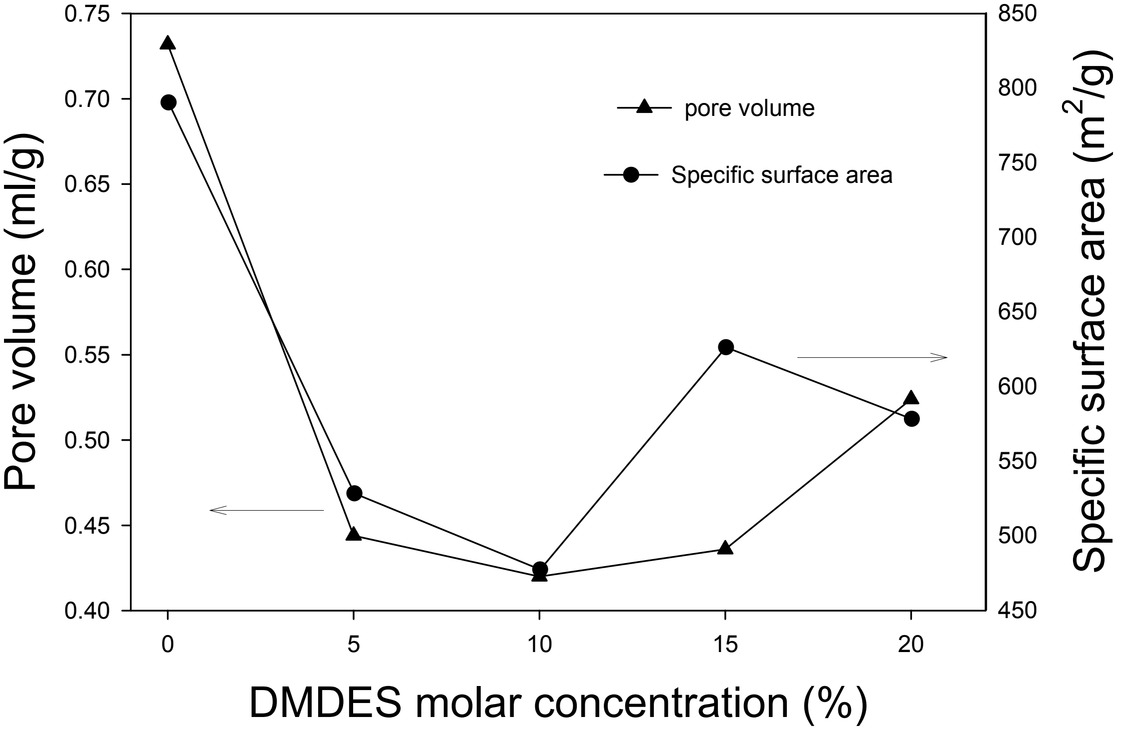

Figure 2: Pore volume and specific surface area changes with DMDES molar portion in DMDES + TEOS system. Data were taken from reference [35].

3.3 Low-k Films

Both organic and inorganic materials can be processed to have low dielectric constants. Some low-k films were listed in Table 3.

Table 3: Candidates for low-k interconnect applications [36]

Materials	Dielectric constant	Deposition method
Ultra low-k materials (k ≤ 2.2)		
Teflon-AF	1.9 – 2.1	Spin on
Teflon-microemulsion	1.9 – 2.1	Spin on
Porous materials		
Porous Silk®	2.2	Spin on
Silica aerogels	1.1 – 2.2	Spin on
Silica Xerogels	1.5 – 2.2	Spin on
Mesoporous silica	1.9 – 2.2	Spin on

Fluorine doped silicon dioxide (FSG, k = 3.3 - 3.7) was successfully introduced into 180 nm technology node and new insulating materials with k = 2.8 will be introduced at the 90 nm node. The measurable performance benefit obtained from FSG, spurred the aggressive introduction of lower k materials (k <3.0) into subsequent generations. The new low-k materials span organic spin-on-polymers (SOP) and both spin-on and PECVD inorganic / organic hybrid materials. Although incorporation of fluorine into low-k materials reduced dielectric constant approximately 10%, ideal ultra-low-k material (k <2.5) should have a closed pore structure and uniformly distributed pores with a maximum pore diameter less than 10% of the technology node. And a tight pore size distribution is also desirable.

Table 4: List of fluorinated Low-k material examples and corresponding dielectric constants

Materials	Dielectric constant	Deposition process
Teflon	2.3	Spin on [36]
TEFS spin-on xerogel	2.3	Spin on [37]
Templated TEFS spin-on xerogel	1.7	Spin on [38]

Porosity has been introduced into several materials, such as silica-based gels or polymer films to further reduce the dielectric constants. However, the introduction of pores severely deteriorates the film mechanical strength. In addition, the target effective dielectric constants require compatible barrier / ILD systems with similarly low dielectric constants. Future interlayer dielectric materials must demonstrate thermal, chemical, and mechanical stabilities to withstand a variety of processes such as wet and dry etching, rapid thermal anneal, and chemical mechanical planarization (CMP).

Silica and fluorinated silica glass (FSG) have been used as ILD's. To further reduce the effective dielectric constant, several approaches have been taken: introduction of porogen (pore producing agents removed in later thermal treatments) into silica films (xerogels), and organic / inorganic hybrid silica films. The inclusion of porosity will affect silica films in following way:

1. Reduction of dielectric constant
2. Lowering of positive mechanical properties

As porosity increases, the effects of surface groups, bonding, compositional variations and interconnectivity within the solid network become critical factors in film dielectric constant and mechanical properties because specific surface area (surface area of unit weight) increases significantly as porosity increases. Surface species, chemical bonding, and local composition influence the polarization contributions to the dielectric constant. Bindings within the network and at inter-particle junctions determine the mechanical properties of the film. Modeling studies by Ma et al. indicate that few of the particle chains within an aerogel network carry significant load [39]. Therefore, the bonding between and within particles will determine the mechanical robustness of a film. The development of robust ultra low-k films require a sound understanding of these issues that to date have not been effectively explored.

Several ways were tried to decrease the effective dielectric constant [40, 41]. One way is to introduce fluorine into either inorganic or organic dielectric materials; however, there are limits to the effects of fluorine on k. The lowest dielectric constant available for fluorinated dense materials is around 1.9. In most materials, incorporation of pores is a more efficient method to reduce dielectric constant. For porous materials, the dielectric constant is a combination of air and that of the dense phase, which offers the extendibility to multiple technology nodes because they have tunable dielectric constants.

At present, most porous low-k materials are produced using either templating or sol-gel technology. In templating, precursors containing thermally labile or non-hydrolyzable groups are co-deposited. The thermally labile components can be removed upon thermal treatment, leaving pores in the dielectric films. In a sol-gel approach, pores are formed during hydrolysis and poly-condensation of alkoxides such as TEOS or $R_xSi(OR')_y$ ($x + y = 4$). Dielectric films such as silica xerogels and porous methylsilsesquioxane (MSQ) films are deposited using this technique. Both sol-gel and templated processes were used in the deposition of surfactant templated porous silica films [42, 43].

Just as the dielectric constant of a porous material is between that of its dense phase and air, mechanical properties such as Young's modulus and hardness also fall between that of its dense phase and air. Young's modulus of a porous material depends strongly on its density and can exhibit a power law relationship, $E \sim (\rho / \rho_0)^n$ where E is the Young's modulus, ρ is the porous material density, and ρ_0 the fully dense matrix density. Changing the density, and therefore the porosity, will have a significant impact on the mechanical properties [44].

Using two-step catalysis of TEOS (B2, base catalyst follows acid catalyst), Jain et al. formed a series of silica xerogel films [45]. After surface modification of the silica xerogel films with trimethylchlorosilane (TMCS), high porosity (58 – 88%) and uniform thickness (0.4 – 2 μm) were obtained. k values ranged from 2.4 to 1.55 were calculated from capacitance measurements. To improve the poor thermal conductivity of methyl containing films, Sugahara et al. tried to incorporate alkane groups into a SiO_2 matrix [46]. Films were deposited by liquid phase (LPD) from $X_3Si – R – SiX_3$ where X can be hydrogen, halogen, alkyl and alkoxy groups and R is C_nH_{2n} group. Films of dielectric constant as low as 2.9 were attained with good thermal conductivity but relatively poor oxidation resistance calculated by ab-initio molecular orbital calculation. Park et al. studied the sol viscosity and aging effects on resulting xerogel microstructures and ensuing dielectric properties [36, 47]. After TMCS modification, stable SiO_2 xerogel films of 47.5 – 73.5 % porosity could be prepared with dielectric constants of 2.45 to 1.99 correspondingly by acid – base two-step catalysis. If the gels were aged at 70°C for two hours, film dielectric constants could be further reduced to 1.42 after TMCS treatment. To enhance film hydrophobicity, Yu et al. used co-precursors of TEOS and MTES [48] and then modified it with TMCS or hexamethyldisilazane (HMDS) [49] to make films with k = 2.0 and porosity about 57%.

3.4 Xerogel

3.4.1 Fluorinated Xerogel

Incorporation fluorine into silica matrix to form Si – F bonding can reduce the dielectric constant in several ways [50]. First, fluorine has the highest electronegativity and draws the electron cloud of the Si – F bond closer to it. This leads a bonding change in the Si – O network deforming the Si – O tetrahedral sp^3 hybrid orbital to the more planar sp^2 orbital, which is less polarizable. Secondly, fluorine can shorten the Si – O bonds in silica xerogel network, make Si – O bonding much stronger. Thirdly, substitution of fluorine for oxygen can lead to lower electronic polarization. Fluorine can also reduce the number of OH groups at the xerogel pore surface, eliminating a highly polarizable source.

Although there has been disagreement among scientists regarding fluorine in the microstructures of the materials studied to date, fruitful results for fluorine reducing k values have been observed. Usami et al. studied plasma enhanced chemical vapor deposited (PECVD) fluorine-doped silicon dioxide films using TEOS and C_2F_6 [51]. Si – F bond formation was confirmed by FTIR and X-ray photoelectron spectroscopy (XPS) and the reduced k value could be 3.6 at 14 atomic percentage of fluorine with good gap filling ability. They observed atomic fluorine outgassing beginning at 350°C but there was still some fluorine left even after 800°C heat treatment for 30 minutes. Homma compared three technologies for deposition of fluorinated silica low-k films: room temperature chemical vapor deposition, liquid phase deposition, and spin-on glass with fluorine-contained alkoxysilane vapor treatment [52]. The dielectric constant at frequency of 1 MHz could be reduced from 3.9 to 3.7 by fluorination of silica films from thermal SiO_2. They believed that the reduction of dielectric constant was mainly due to the reduction of electronic polarization at the Si – F bonds.

By changing the radio frequency (RF) power, Kitoh et al. studied the PECVD method using TEFS as gas precursor. The relative dielectric constant of the films deposited was 3.5 with better Si – F bond stability and less moisture absorption, compared with films deposited by PECVD using C_2F_6 added TEOS precursor [53]. But using CF_4 adding to SiH_4 / N_2O as gas sources for PECVD, Lim et al. deposited fluorine-doped silica films with dielectric constants as low as 2.3 and good step coverage with low porosity [54]. Combining capacitance-voltage (CV) measurement at

1 MHz, FTIR data, and ellipsometry data, they believed that the decrease in dielectric constant was mainly due to the decrease in the ionic polarization. And the change in Si – O stretching mode due to fluorine addition seemed to be the most important factor in the decrease in dielectric constants. Changing the gas flow to SiH_4 mixed with SiF_4, O_2, and Ar, Denison et al. deposited fluorine-dope silica films using electron cyclotron resonance high-density oxygen plasma [55]. Fluorine concentration was found uniform throughout the films by nuclear resonance analysis (NRA). The minimum observed k was 3.55 at 10.5 atomic percentage of fluorine.

Using SiF_4 / TEOS / O_2 mixing gas, Bhan et al. deposited fluorine doped silica films with dielectric constant of 3.5 at fluorine concentration of 2.4 %, as determined by FTIR spectra Si – F / Si – O peak area ratio [56]. Below fluorine concentration of 3 %, they believed that only Si – F bonding existed, but no Si – F_n bonding. Si – F bonding was robust up to 600°C, did not absorb moisture, and showed stable dielectric constants. After exposure to humid environment, Yoshimaru et al. found both Si – F and Si – F_2 were hydrolyzed by water, although F – Si – F sites were more interactive with water than Si – F sites [57]. F – Si – F bonds could be hydrolyzed at low temperatures and generated Si – OH bonds after reaction. F – Si – F sites increased as fluorine concentration increases and consequentially increased the amount of water absorbed when exposed to ambient humidity. To overcome such a problem, they used silicon nitride as cap layer and the lowest k value was 2.8 at 11.5 atomic percent fluorine. Using FTIR and Raman data, they found that fluorine doping could decrease Si – OH groups and three-membered ring structures in film [58]. Fluorine atoms reacted with strained Si – O – Si bonds in silica and relaxed the silica host network. Although fluorine could form Si – F and F – Si – F, increases in Si – F bonds saturated, while F – Si – F bonds increased linearly as fluorine source gas flow increased. In 2001, a spin-on fluorinated silica xerogel film was developed with very low dielectric constant (2.1 as processed and 2.3 after heat treatment at 450°C in air) by our group [37]. Xerogel films displayed very good mechanical, electrical, and micro-structural properties. These films were intrinsically hydrophobic, which deserves further research and characterization.

3.4.2 Templated Xerogel

Addition of pores can further decrease dielectric constant [59]. Properties such as pore shape, pore size and pore size distribution have an effect on dielectric constant while the spatial pore distribution is expected to influence the dielectric constant to a greater extent, as determined by computer simulation.

Porosity can be introduced into silica films mainly through two ways: (1) removal solvent / co-solvent and (2) molecularly templated synthesis, in which pores are created by removal of the organic templates such as micelles of surfactants. Molecularly templated synthesis generally offers a uniform pore size in the nanometer range, and an ordered pore structure with a controllable porosity. These advantages make a molecularly templated nanoporous silica film suitable for future semiconductor technology nodes.

There are three methods to introduce templating agents into cross-linked silica networks. The most common way involves polymerization in the presence of non-covalently bonded templates that are removed after gelation. The size of the template can range from several angstroms to several microns. Small molecules such as methyl orange, and dopamine as well large species such as latex beads and bacteria were successfully used to generate molecularly controlled porosity. The second approach involves polymerization of two precursors followed by selective removal of one precursor. This class of templating is rather wide, encompassing a wide range of affinities between different monomers. The third type of processing involves poly-condensation of co-precursors, where at least one precursor has bulky pendant group to induce pore size and formation [60].

Since mesoporous molecular sieves such as hexagonally ordered MCM -41 were discovered by Mobil Corporation scientists in 1992, surfactant templating procedures have been extended to include a wide range of compositions [61, 62]. A variety of conditions have been developed for exploiting the structure-directing functions of electrostatic, hydrogen bonding, and van der Waals interactions. Using poly(ethylene oxide) – poly(propylene oxide) – poly(ethylene oxide) (PEO – PPO – PEO) templating TEOS, TMOS, or tetrapropoxysilane (TPOS), Zhao et al. created hexagonal mesopores with pore sizes between 46 and 100 Å by different ratios of ethylene oxide (EO) and propylene oxide (PO) compositions with and without addition of 1, 3, 5-trimethylbenzene (TMB) as a swelling agent [63]. A film with k values as low as 1.9 was synthesized by Nguyen et al. using six armed star-shaped hydroxyl-terminated poly(ε-caprolactone) (PCL) to template methylsilsesquioxane (MSQ) [64]. Upon heating to 430°C, PCL was thermally decomposed and volatilized from the vitrified poly(methylsilsesquioxane) (PMSQ), leaving behind porous PMSQ films with pores with the size and shape of the original hybrid morphology. Dielectric constants as low as 1.9 were achieved with 30 % detectable porosity in SiO_2 with closed cell nano-pores and hydrophobic surfaces. Using a spin-on glass (SOG) obtained from hydrolysis of methyltriethoxysilane and dimethoxymethyl-3,3,3-triflluoropropylsilane, Yamada et al. believed that curing the SOG film in nitrogen to 450°C would only decompose the triflluoropropyl groups and allow the methyl groups to remain [65]. The dielectric constant was reduced to 2.3 due to the pores introduced into the methylsiloxane network. By addition of triblock co-polymers (Pluronic-P123; EO 20 (PO) 70 (EO) 20) to acidic TEOS sol, Fan et al. co-assembled silica and surfactants in a spin-on film [66]. Depending on the swelling agent (polypropylene glycol (PPO)), films with dielectric constants from 1.3 to 2.6 were obtained. Using similar chemicals, Cho et al. discovered the silica xerogel film pore diameter was about 85 Å by X-ray diffraction (XRD) [67]. After calcining in an oxygen plasma followed by an HMDS / H_2 plasma / HMDS treatment, the dielectric constant of the silica films could be reduced to 1.7. Lubguban et al. deposited films with k from 2.5 to 2.9 by changing pressure and temperatures in a PECVD system [68]. Using tetravinyltetramethylcyclotetrasiloxane (TVTMCTS) as a liquid precursor, they showed that the Si – O ring structures could be reserved to introduce pores, methyl groups provide film hydrophobicity and films were obtained by active vinyl group polymerization. The films were thermally stable up to 400°C.

3.5 References

1. J.C. Pouxviel, J.P. Boilot, J.C. Beloeil, and J.Y. Lallemand, J. Non-Cryst. Solids, 89 (1987) 345.
2. R.A. Assink, and B.D. Kay, J. Non-Cryst. Solids, 99 (1988) 359.
3. R.A. Assink, and B.D. Kay, Colloids and Surfaces A: Physicochemical and Engineering Aspects, 74 (1993) 1.
4. U. Jaglid, and O. Lindqvist, Acta Chemica Scandinavica, 44 (1990) 765.

5. J. Chojnowski, M. Cypryk, K. Kazmierski, and K. Rozga, J. Non-Cryst. Solids, 125 (1990) 40.
6. R. Aelion, A. Loebel, and F. Eirich, J. Am. Chem. Soc., 72 (1950) 5705.
7. H. Yang, Z. Ding, Z. Jiang, and X. Xu, J. Non-Cryst. Solids, 112 (1989) 449.
8. J.C. Pouxviel, and J.P. Boilot, J. Non-Cryst. Solids, 94 (1987) 374.
9. J.C. Ro, and J. Chung, J. Non-Cryst. Solids, 110 (1989) 26.
10. R.A. Assink, and B.D. Kay, J. Non-Cryst. Solids, 104 (1988) 112.
11. R.A. Assink, and B.D. Kay, J. Non-Cryst. Solids, 107 (1988) 35.
12. J. Sanchez, and A. McCormick, J. Phys. Chem., 96 (1992) 8973.
13. Y. Sugahara, S. Okada, K. Kuroda, and C. Kato, J. Non-Cryst. Solids, 139 (1992) 25.
14. P. Lux, F. Brunet, H. Desvaux, and J. Virlet, Magn. Reson. Chem., 31 (1993) 623.
15. P. Lux, F. Brunet, J. Virlet, and B. Cabane, Magn. Reson. Chem., 34 (1996) 173.
16. T.M. Alam, Spectrochimica Acta: part A, 53 (1997) 545.
17. S. Suda, M. Iwaida, K. Yamashita, and T. Umegaki, J. Non-Cryst. Solids, 197 (1996) 65.
18. R.K. Harris, and M.L. Robins, Polymer, 19 (1978) 1123.
19. R.J. Hook, J. Non-Cryst. Solids, 195 (1996) 1.
20. S.E. Rankin, C.W. Macosko, and A.V. McCormick, IChE journal, 44 (1998) 1141.
21. F. Babonneau, Polyhedron, 13 (1994) 1123.
22. D, Avinir, L.C. Klein, D. Levy, U. Schubert, and A.B. Wojcik, in The Chemistry of Organic Silicon Compounds, Vol. 2, Z. Rappoport, Y. Aploig (Eds.), John Wiley & Sons, 1998, p. 2317.

23. D.A. Loy, MRS Bull., 26 (2001) 364.
24. N. Husing, and U. Schubert, Angew, Chem. Int. Ed., 37 (1998) 22.
25. D.A. Loy, and K.J. Shea, Chem. Rev., 95 (1995) 1431.
26. D.A. Loy, B.M. Baugher, C.R. Baugher, D.A. Schneider, and K. Rahimian, Chem. Mater., 12 (2000) 362.
27. H. Dong, PhD dissertation, Dept. of Materials Science and Engineering, Univ. of North Texas, 2003.
28. R.H. Glaser, G.L. Wilkes, and C.E. Bronnimann, J. Non-Cryst. Solids, 113 (1989) 73.
29. M.J. van Bommel, T.N.M. Bernards, and A.H. Boonstra, J. Non-Cryst. Solids, 128 (1991) 231.
30. F. Babonneau, L. Bois, and J. Livage, J. Non-Cryst. Solids, 147&148 (1992) 280.
31. T. Iwamoto, K. Morita, and J.D. Machenzie, J. Non-Cryst. Solids, 159 (1993) 65.
32. F. Babonneau, Mat. Res. Soc. Symp. Proc. Vol 346, 1994, p949.
33. J. Brus, and J. Dybal, Polymer, 40 (1999) 6933.
34. S.K. Mah, and I.J. Chung, J. Non-Cryst. Solids, 183 (1995) 252.
35. B.M. De Witte, D. Commers, and J.B. Uytterhoeven, J. Non-Cryst. Solids, 202 (1996) 35.
36. J. Kim, H. Kim, H. Park, and S. Hyun, Appl. Surf. Sci., 169-170 (2001) 452.
37. B.P. Gorman, R.A. Orozco-Teran, J.A. Roepsch, H. Dong, D.W. Mueller, and R.F. Reidy, App. Phys. Lett., 79 (2001) 4010.
38. Z. Zhang, H. Dong, B.P. Gorman, C. Yao, D.W. Mueller, and R.F. Reidy, Electrochem. Soc., (2003) 170.

39. H.S. Ma, J.H. Prevost, R. Jullien, and G.W. Scherer, J. Non-Cryst. Solids, 285 (2001) 216.
40. W.W. Lee, and P.S. Ho, MRS bulletin, 22 (1997) 19.
41. ITRS Interconnect, 2003.
42. P.J. Bruinsma, N.J. Hess, J.R. Bontha, J. Liu, and S. Baskaran, Mat. Res. Soc. Symp. Proc., 445 (1997) 105.
43. Y. Lu, R. Ganguli, C.A. Drewien, M.T. Anderson, C.J. Brinker, W. Gong, Y. Guo, H. Soyez, B. Dunn, M.H. Huang, and J.I. Zink, Nature, 389 (1997) 364.
44. C. Jin, S. Lin, and J.T. Wetzel, J. Electron. Mater., 30 (2001) 284.
45. A. Jain, S. Rogojevic, S.V. Nitta, V. Pisupatti, W.N. Gill, P.C. Wayner Jr., J.L. Plawsky, T.E.F.M. Standaert, and G.S. Oehrlein, Mat. Res. Soc. Symp. Proc., 565 (1999) 29.
46. S. Sugahara, K. Usami, and M. Matsumura, Jpn. J. App. Phys., 38 (1999) 1428.
47. J. Hong, H. Kim, and H. Park, Thin Solid films, 332 (1998) 449.
48. S. Yu, T. Wong, K. Pita, and X. Hu, J. Vac. Sci. Technol. B, 20 (2002) 2036.
49. S. Yu, T. Wong, K. Pita, X. Hu, and V. Ligatchev, J. App. Phys., 92 (2002) 3338.
50. S. Mizuno, A. Verma, H. Tran, P. Lee, and B. Nguyen, Thin Solid Films, 283 (1996).
51. T. Usami, K. shimokawa, and M. Yoshimaru, Jpn. J. App. Phys., 33 (1994) 408.
52. T. Homma, Mat. Res. Soc. Symp. Proc., V381 (1995) 239.
53. H. Kitoh, M. Muroyama, M. Sasaki, M. Iwasawa, and H. Kimura, Jpn. J. App. Phys., 35 (1996) 1464.
54. S.W. Lim, Y. Shimogaki, Y. Nakano, K. Tada, and H. Komiyama, Jpn. J. App. Phys., 35 (1996) 1468.

55. D.R. Densison, J.C. Barbour, and J.H. Burkhart, J. Vac. Sci. Technol. A, 14(3) (1996) 1124.
56. M.K. Bhan, J. Huang, and D. Cheung, Thin Solid Films, 308-309 (1997) 507.
57. M. Yoshimaru, S. Koizumi, and K. Shimokawa, J. Vac. Sci. Technol. A, 15(6) (1997) 2915.
58. M. Yoshimaru, S. Koizumi, and K. Shimokawa, J. Vac. Sci. Technol. A, 15(6) (1997) 2908.
59. J.A. Roepsch, MS Thesis, Dept. Mater. Sci. Eng., Univ. North Texas, 2001.
60. S. Srebnik, and O. Lev, J. Sol Gel Sci. Technol., 26 (2003) 107.
61. M. Estermann, L.B. McCusker, C. Baerlocher, A. Merroche, and J. Kessler, Nature, 352 (1991) 320.
62. C.T. Kresge, M.E. Leonowicz, W.J. Poth, J.C. Vartuli, and J.S. Beck, ibid, 359 (1992) 710.
63. D. Zhao, J. Feng, Q. Huo, N. Melosh, G.H. Fredrickson, B.F. Chmelka, and G.D. Stucky, Science, 279 (1998) 548.
64. C.V. Nguyen, K.R. Carter, C.J. Hawker, J.L. Hedrick, R.L. Jaffe, R.D. Miller, J.F. Remenar, H. Rhee, P.M. Rice, M.F. Toney, M. Trollsas, and D.Y. Yoon, Chem. Mater., 11 (1999) 3080.
65. N. Yamada, and T. Takahashi, J. Electrochem. Soc., 147(4) (2000) 1477.
66. H. Fan, H.R. Bentley, K.R. Kathan, P. Clem, Y. Lu, and C.J. Brinker, J. Non-Cryst. Solids, 285 (2001) 79.
67. A.T. Cho, T.G. Tsai, C.M. Yang, K.J. Chao, and F.M. Pan, Electrochem. Solid-state Lett., 4(4) (2001) G35.

68. J. Lubguban, Jr. T. Tajagopalan, N. Mehta, B. Lahlouh, S.L. Simon, and S. Gangopadhyay, J. App. Phys., 92 (2002) 1033.

CHAPTER 4

EXPERIMENTAL

4.1 DMDES Polymerization and Cyclization by Liquid ^{29}Si NMR

Hydrolysis and condensation of Dimethyldiethoxysilane (DMDES) (Gelest, Inc. 95%) was analyzed on a Varian 300 high resolution nuclear magnetic resonance (NMR) Spectroscopy. DMDES was first dissolved in ethyl alcohol (EtOH, AAper Alcohol and Chemical Co. 100%). Water was introduced in two forms: 0.01 N HCl (EM Science) catalyst solution and D_2O (Aldrich, 99.9%) as a locking-agent. Two molar ratio (R) and (r) were defined as:

$$R = \frac{\text{moles of EtOH}}{\text{moles of precursor}}$$

$$r = \frac{\text{moles of water}}{\text{moles of precursor}}$$

Throughout the experiment, R and r were held constant: 4. EtOH was introduced as a solvent for DMDES and as a mixture with 0.01 N HCl catalyst. In each case, EtOH was equal (2 by 2 molar quantities versus DMDES molar ratio). Water was used as H_2O and D_2O, in about equal molar amount while keeping r = 4. D_2O was used as locking agent. According to Scherer and Brinker [1], a molar ratio of water to DMDES (r) around 4 would have a moderate reaction rate; therefore, most reaction products could be detectable in liquid ^{29}Si NMR.

Initially DMDES was dissolved in EtOH solution in one vial. In another vial an equal amount of EtOH, 0.01 N HCl, D_2O and chromium (III) acetylacetonate ($Cr(AcAc)_3$, Aldrich) were mixed completely. The two solutions were mixed together and quickly introduced into a 5 mm NMR tube. The initial concentrations of DMDES, EtOH, H_2O, D_2O and HCl were in Table 5:

Table 5: Initial chemical concentrations

chemical	Concentration (M)
DMDES	1.902
EtOH	7.541
H_2O	3.890
D_2O	4.202
HCl	7×10^{-4}

^{29}Si NMR measurements were conducted on a Varian VXR300 high resolution NMR spectrometer with a pulse width of 5μs and a delay of 10s using gated decoupling to suppress nuclear Overhauser effects (NOE). Mah et al. [2] and Hook [3] have used $Cr(AcAc)_3$ as the non-polar paramagnetic relaxation agent showing no effect on sol-gel reactions but reduced data-collecting time. Tetramethylsilane (TMS, Aldrich, 99.9%) was used as an internal reference (chemical shift 0 ppm). Usually tens or hundreds of FIDs (free induction decay) were collected for each spectrum.

4.2 Film Preparation

Triethoxyfluorosilane ($FSi(OC_2H_5)_3$, TEFS, Gelest, 95%) was used as silica matrix precursor without further purification. TEFS has three hydrolyzable Si – OC_2H_5 bonds to undergo hydrolysis and condensation to form dimensional silica networks and one Si – F bond.

In a nitrogen glove box, TEFS was dissolved in EtOH. Under ambient conditions these solutions hydrolyzed with water under 0.01 N HCl catalyst (the solution was called 'sol'), keeping R equal to 15 and r equal to 4. After pregeling for 30 seconds, xerogel films were spun onto both single- and double- polished Si wafers on a Headway spin coater at 1500 rpm for 30 seconds. Si wafer substrates were cleaned with 1% volume HF (EM Science) and dried with nitrogen. The spin coater chamber was saturated with EtOH to hinder solvent evaporation from the wet gel films, promoting gel aging. To make bulk xerogels, some TEFS sols were gelled and dried then covered with parafilm to control solvent evaporation. Both film and bulk samples were used for characterizations.

Hybrid samples were made by introducing DMDES reaction products into TEFS prior to gelation. First DMDES was dissolved in ethanol and reacted with 0.01 N HCl catalysts for a specific time. Different amounts of DMDES were introduced into TEFS and EtOH solutions under nitrogen, and these solutions were transferred into polyethylene or polypropylene vials. Sol viscosity was measured during reaction using a Brookfield Programmable DV-II+ viscometer with spindle spin rate of 100 rpm. To prevent solvent evaporation, samples were covered during viscosity measurements. Hybrid films were prepared by spinning the hybrid sols onto Si wafers. Some hybrid sols were gelled and dried to make bulk samples, like TEFS sample preparations. All hybrid samples were kept under nitrogen for further characterizations.

To determine the best time for DMDES introduction, samples were prepared with different DMDES pregeling times with a fixed DMDES to TEFS molar ratio of 35:65. Several characterization techniques were combined to find the optimal DMDES introducing time.

At the optimal introduction time, another series of experiments was conducted by keeping R and r of 15 and 4, respectively, but changing the DMDES to TEFS molar ratio. To account for the EtOH and water introduced with the DMDES sol while keeping total R and r constant, volumes of EtOH, H_2O, TEFS and DMDES sols were calculated from following equations:

$$V_{EtOH} = (15 - x * 4) \times 58.7 \qquad (1)$$

$$V_{H2O} = (4 - x * 4) \times 18 \qquad (2)$$

$$V_{TEFS} = (1 - x) \times 202 \qquad (3)$$

$$V_{DMDES} = x * (4 * 58.7 + 4 * 18 + 176.7) / 176.7 \qquad (4)$$

In equation (1), 15 and 4 were R and r for TEFS + DMDES, and 58.7 milliliters per mole (ml/mol) is the EtOH molar volume. In equation (2), 4 and 4 were R and r for DMDES, 18 ml/mol is the H_2O molar ratio. The TEFS molar volume is 202 ml/mol in equation (3). The DMDES molar volume is 176.7 ml/mol in equation (4). And x is DMDES molar ratio (moles of DMDES / moles of DMDES + moles of TEFS) added in all the equations.

4.3 Sample Characterizations

4.3.1 Fourier Transform Infrared Spectroscopy (FTIR)

FTIR spectra were obtained on a Nicolet Nexus 470 spectrometer with an MCT-B detector. Depending on the nature of samples, several accessories (attenuated total reflection (ATR), grazing angle total reflection (GATR), or transmission) were used. In ATR mode, the IR source is directed into a Si internally reflecting crystal (45°), and an evanescent wave interacts with samples contacted with the Si crystal. To maintain contact, a constant force (~2 pounds) is used. After interacting with samples, IR signal was attenuated. Transmission mode was used for samples on double polished Si wafers. GATR uses a Ge internal reflection element, and the IR incident angle is 65°. GATR is a much more surface sensitive method. All FTIR spectra were averaged over 32 or 64 scans with a 2 or 4 cm^{-1} wavenumber resolution from 600 to 4000 cm^{-1}. IR intensity loss due to air in the light path and internal reflection elements were counted for by automatic background subtraction.

4.3.2 Gas Sorption

Average pore size of bulk samples was analyzed on a Quantachrome Nova 2200 Gas Absorption Analyzer using the BJH method [4], assuming a N_2 cross section of 16.2 $Å^2$. Before measurements, samples were degassed at 150^0C and 77 torr for a minimum of one and a half hours to ensure removal of all water and organic solvents. Isothermal adsorption and desorption occurred at constant temperature of 77K.

4.3.3 Contact Angles

Contact angle measurements were conducted on Rame-Hart goniometer using DI water as testing liquid. For each sample, at least 5 contact angles were made to get the average contact angle and mean error.

4.3.4 Thermal Gravimetric Analysis (TGA)

TGA measures sample weight loss with temperature increase. To understand thermal stability of samples, TG analyses were conducted on a Perkin Elmer Pyris Diamond system. In a heated microbalance, sample was placed in an aluminum pan and alumina was placed in the other pan as a reference. Experiments were carried out under a N_2 or O_2 flow of 30 sccm (standard cube centimeter per minute) with a heating rate of 5°C / minute to 400°C. Sample weight was measured continuously. Prior to data collection, system was allowed to equilibrate at 50°C for 5 minutes.

4.3.5 Ellipsometry Measurements

Film thickness and porosity were measured using variable angle spectroscopic ellipsometer (VASE, J. A. Woollam Co., Inc.).

Ellipsometry employs polarized light to measure film properties. When polarized light is incident on a sample, the polarization state of reflective or transmitted light changes. The change is a function of the sample properties (such as layer thickness, layer optical properties (refractive index, etc.) and so on), which modify the outgoing light from the sample. An ellipsometer measures this change as two values (psi (Ψ) and delta (Δ)). These values are related to the ratio (ρ) of Fresnel reflection coefficients $\check{R}_p$ and $\check{R}_s$ for p- and s- polarized light as:

$$\rho = \check{R}_p / \check{R}_s = \tan(\psi)e^{i\Delta}$$

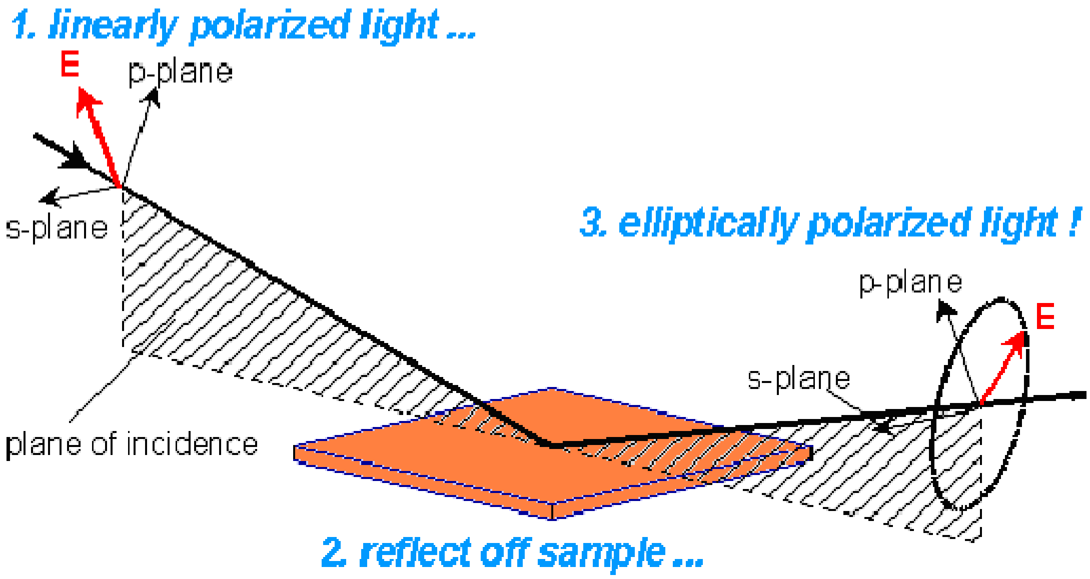

Fig. 3: Linear polarized light incident and outgoing ellipsoid polarized light [5]

After collecting experimental data, film properties under investigation were obtained by a model-fitting process.

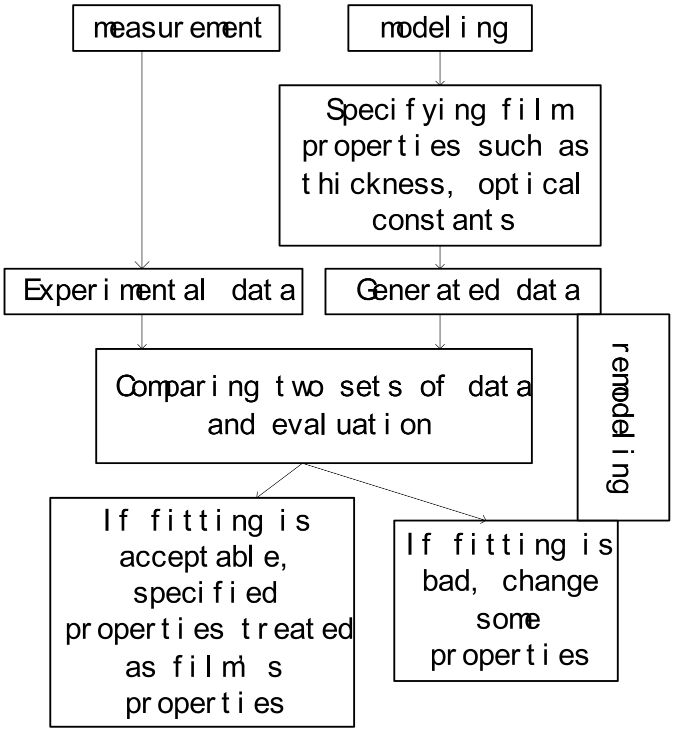

Fig. 4: Ellipsometer data processing method [6]

We used the Cauchy relation and Urbach absorption to model samples:

$$n(\lambda) = A_n + B_n / \lambda^2 + C_n / \lambda^4$$

$$k(\lambda) = A_k\, e^{Bk(1.24\,(1/\lambda - 1/Ck))}$$

$n(\lambda)$, $k(\lambda)$ are refractive index and extinction coefficient at each incident light wave length respectively. λ is incident light wavelength in microns. A_n, B_n, and C_n are Cauchy parameters. A_k is the absorption amplitude. B_k is the broadening and C_k is the absorption band edge, fixed at 400 nm.

A standard SiO_2 sample (TEOS CVD SiO_2 1000Å thick) was used as reference.

Each sample was scanned using wavelength of 400 to 1000 nm at three different incident angles: 65°, 70°, and 75°. Data were analyzed with WVase32 software from J.

A. Woollam Co., Inc. using Cauchy model [6]. The refractive indices of the films were measured at 632.8 nm wavelength. Porosity was calculated using Lorentz-Lorenz equation [7]

$$\frac{(N_f^2 - 1)}{(N_f^2 + 2)} = (1 - v_p)\frac{(N_s^2 - 1)}{(N_p^2 + 2)} + v_p\frac{(n_p^2 - 1)}{(N_s^2 + 2)}$$

where n_f, n_s, and n_p are the refractive indices of film, fully densified solid matrix and the substances inside the pore, usually air ($n_p = 1$, c.a.) at 632.8 nm wavelength, respectively. n_s was used as 1.43. And v_p is pore volume ratio, or porosity.

4.3.6 Impedance Measurements

A metal-insulator-semiconductor (MIS) structure was built for capacitance versus DC bias measurements. A heavily doped p-type single polished Si wafer (resistivity: < 10 Ωcm, from Texas Instrument Inc.) was cleaned with 1% volume HF solution (EM Science) and dried with nitrogen. Films were spun onto the Si wafer. On the back of Si wafer, about 1000 Å thick aluminum (Kurt J. Lesker Com. 99%) was deposited and annealed to enhance the backside contact. Top electrodes were patterned using shadow masks using Au (Kurt J. Lesker Com. 99.99%) physical vapor deposition (PVD) (1000 Å thick, ca.). Au dot diameters were measured under a SEM (JEOL 840 with tungsten filament) at 20.0 KV accelerating voltage. Capacitance was measured on an Agilent 4294A impedance spectrometer at frequency 1M. DC bias was swept from -2 volts to 2 volts. Capacitances in accumulation region were used to calculate dielectric constant values using the parallel plate model:

$C = k_0 * k_r * A / d$

C: capacitance in accumulation region, k_0: dielectric constant of vacuum, k_r: relative dielectric constant of samples, A: dot electrode area, and d: sample thickness.

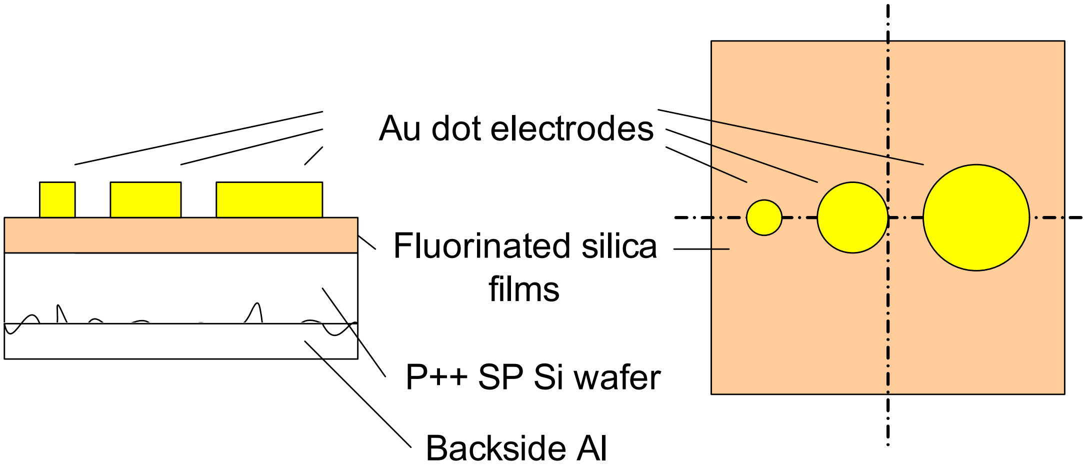

Fig. 5: Structure for impedance measurements

Impedance is a parameter for characterizing electronic circuits, components, and the materials used. Impedance (Z) is defined as the hindrance a unit offers to the current flow, and generally represented as a complex quantity consisted of a real part (resistance, R) and an imaginary part (reactance, X), as shown in Fig. 6. Reactance can include capacitance (C) and / or inductance (L). By measuring the impedance, capacitance of the material can be obtained.

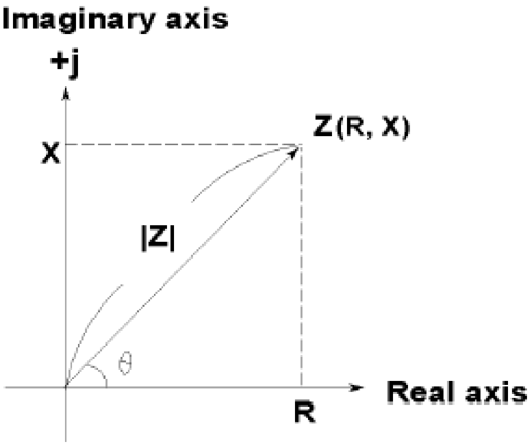

$$Z = R + jX = |Z|\angle\theta$$

$$\begin{cases} R = |Z|\cos\theta \\ X = |Z|\sin\theta \end{cases}$$

$$\begin{cases} |Z| = \sqrt{R^2 + X^2} \\ \theta = \tan^{-1}\left(\frac{X}{R}\right) \end{cases}$$

Fig. 6: Real part (R) and imaginary part (X) of impedance [8]

Impedance can be measured as follows:

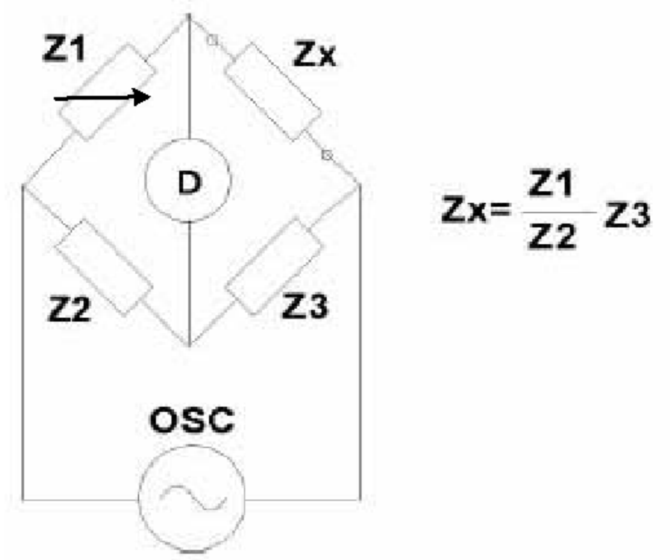

Fig. 7: Maxwell Bridge for impedance measurement [8]

By adjusting the adjustable component Z1, when no current flows through the detector (D), the value of the unknown impedance Zx can be calculated by the relationship of the other bridge elements Zx = Z1 * Z3 / Z2 (all are complex numbers). Various types of bridge circuits, employing combinations of L, C, and R components as the bridge elements, can be used for specific capacitance measurements.

4.3.7 Young's Modulus and Hardness

Young's modulus and hardness were measured on a MTS nanoindentation instrument with a Berkovich diamond tip under constant strain rate mode (0.05 sec^{-1}). For each sample, 9 or 25 individual indentations were made. For each indentation, data pairs of each force and corresponding penetration depth were collected continuously to set depth. Only the first 10 % of film thickness was used to measure Young's modulus and hardness to minimize surface and substrate effects. Fused silica was used as tip cross-area calibration standard.

4.3.8 Other Measurements

Some samples were imaged in cross section on a Hitachi 4700 scanning electron microscopy (XSEM). Fluorine and carbon depth profiles were measured on a Cameca 4f dynamic secondary ion mass spectrometer (DSIMS). Fluorine concentration in some samples was measured in University of Texas at Austin by X-ray photoelectron spectrometry (XPS) and nuclear reaction analysis (NRA) in State University of New York at Albany (SUNY-Albany) with the reaction $^{19}F\ (p, \alpha\gamma)\ ^{16}O$ using known thickness samples of CaF_2 as standard references [9].

4.4 References

1. C.J. Brinker, and G.W. Scherer, Sol-Gel Science: the Physics and Chemistry of Sol-Gel Processing, Academic Press, San Diego, 1990.
2. S.K. Mah, I.J. Chung, J. Non-Crystl. Solids, 183 (1995) 252.
3. R.J. Hook, J. Non-Cryst. Solids, 195 (1996) 1.
4. E.P. Barrett, L.G. Joyner, and P.P. Halenda, J. Amer. Chem. Soc., 73 (1951) 373.
5. Tutorial from J.A. Wollam Co., Inc., at www.Jawoollam.com/tutorial.
6. Guide to Using Wvase32, J.A. Woollam Co., Inc..
7. Principles of Optics, 7th ed. by Max Born and Emil Wolf, p89-103.
8. Agilent Technologies Impedance Measurement Handbook, 2nd ed., Agilent Technologies.
9. Handbook of Modern Ion Bean for Materials Analysis, by J.R. Tesmer, and M. Nastasi, chapter 6, p139 - 166.

Chapter 5

RESULTS AND DISCUSSION

5.1 DMDES Hydrolysis and Poly-condensation

For ^{29}Si NMR experiments, D_n notations similar to that employed by Glaser et al. [1] and Rankin [2] were employed, as shown in Table 6. D_0 signifies $(CH_3)_2$-Si-$(OC_2H_5)_{2-n}(OH)_n$, with n = 0,1,2. D_1 represents $(CH_3)_2$-Si-(OR)$(O_{1/2})$-, where R = H - or C_2H_5 -, two kinds of ends. D_2 represents -$(O_{1/2}$-$[(CH_3)_2]$Si-$O_{1/2})_n$-, n = 1, 2, etc, (middle groups). C_3 represents 3-membered rings $((CH_3)_2Si\text{-}O\text{-})_3$) and C_4 represents 4-membered rings $((CH_3)_2Si\text{-}O\text{-})_4$).

Table 6: Assignment of ^{29}Si NMR signals of hydrolysis and condensation of DMDES under acidic condition and notations used. Underline shows the silicon atoms to which the chemical shift corresponds.

Chemical shift (ppm)	Possible source	Notation
-3.74	$(CH_3)_2Si(OC_2H_5)_2$	D_0^0
-4.39	$(CH_3)_2Si(OC_2H_5)(OH)$	D_0^1
-4.88	$(CH_3)_2Si(OH)_2$	D_0^2
-8.73	$((CH_3)_2SiO)_3$	C_3
-12.60	$(CH_3)_2(OC_2H_5)SiOSi(OC_2H_5)(CH_3)_2$	D_1^0
-12.71	$(CH_3)_2(OC_2H_5)\underline{Si}OSi(OH)(CH_3)_2$	D_1^1
-12.79	$(CH_3)_2(OC_2H_5)\underline{Si}OSi(CH_3)_2OSi(OH)(CH_3)_2$	$D_1^0D_2D_1^1$
-13.08	$(CH_3)_2(OH)\underline{Si}OSi(CH_3)_2O\underline{Si}(OH)(CH_3)_2$	$D_1^1D_2D_1^1$
-13.12	$(CH_3)_2(OH)SiOSi(OH)(CH_3)_2$	D_1^2
-13.35	$(CH_3)_2(OC_2H_5)SiO\underline{Si}(OH)(CH_3)_2$	D_1^1
-13.54	$(CH_3)_2(OC_2H_5)SiOSi(CH_3)_2O\underline{Si}(OH)(CH_3)_2$	$D_1^0D_2D_1^1$
-19.13	$((CH_3)_2SiO)_4$	C_4
-21.51	$(CH_3)_2(OC_2H_5)SiO\underline{Si}(CH_3)_2OSi(OH)(CH_3)_2$	D_2^1
-21.77	$(CH_3)_2(OH)SiO\underline{Si}(CH_3)_2OSi(OH)(CH_3)_2$	D_2^2

According to Sugahara [3, 4], liquid ^{29}Si NMR alkylalkoxide spectra can be mainly divided to three regions, D_0 (- 3 to - 5 ppm), D_1 (- 10 to - 13 ppm), and D_2 (- 20 to - 23 ppm). Fig. 8 shows the ^{29}Si NMR spectra of the DMDES in EtOH sol system (R = 4, r = 4). During the initial 1 - 4 minutes, five signals were detected, three in D_0 region (-3.74, - 4.39, - 4.88 ppm), two in D_1 region (- 12.71, - 13.10 ppm). In the D_0 region, the middle peak was found to have the highest intensity. Ten minutes later, three signals remained in the D_0 region with the middle one (- 4.39 ppm) the most intense. Their chemical shifts were unchanged within an error of ± 0.1 ppm while the time interval and their relative ratios remained almost the same. The D_1 region showed four signals, -12.60, - 12.71, - 13.12, and - 13.35 ppm, and a tiny hump was observed in D_2 region.

At approximately 30 minutes, the three signals in the D_0 region were all present and maintained their relative ratios. But in D_1 region, three more signals appeared, - 12.79, -13.08, and -13.54 ppm. In D_2 region two peaks appeared: -21.51, -21.77 ppm. Between D_0 and D_1, a peak appeared at -8.73 ppm indicating the presence of 3-membered rings. Around 60 - 90 minutes later, the signal at -3.74 ppm in D_0 region disappeared, the other two (-4.39, -4.88 ppm) became very small, and the signal at - 4.39 ppm grew larger. All of the signal intensities in D_1 region decreased. A peak corresponding to 4-membered rings appeared at -19.13 ppm. After 1440 minutes, no signal remained in D_0 region. Intensities of 3-membered rings and signals in D_1 region shrank. 4-membered rings and D_2 signals grew larger.

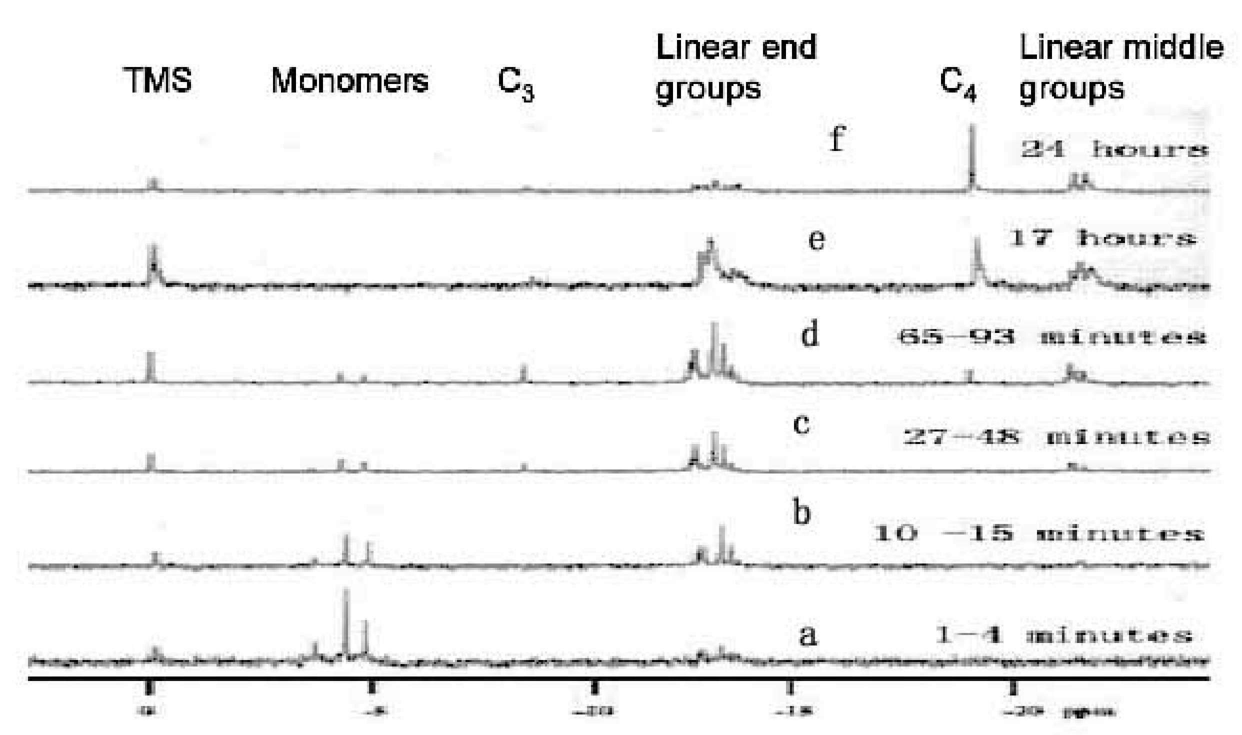

Fig. 8: ^{29}Si NMR spectra of DMDES hydrolysis and condensation progress with time: (a) 1 - 4 minutes: (b) 10 - 15 minutes; (c) 27 - 48 minutes; (d) 56 - 93 minutes; (e) 1020 minutes (17 hours) (another sample with the same R and r ratios); (f) 1440 minutes (24 hours)

Previous works have described the complications in assigning the high-resolution ^{29}Si NMR peaks to the corresponding alkoxysilane hydrolysis and condensation species, especially under acidic conditions. Schmidt illustrated that modified alkoxysilanes could react much faster than unmodified species under proton - catalyzed hydrolysis if the formation of a siliconium ion $RO(CH_3)_2Si^+$ (R= $-C_nH_{2n+1}$) is the rate-limiting step [5]. To further complicate matters, as reactions progress, there are some upfield and / or downfield variations because of hydroxyl groups. So in a specific system, understanding which factors dominate is very important.

In DMDES under HCl catalysis, Hook suggested that factors other than inductive effects caused an upfield shift during the hydrolysis of Si – OR to Si – OH [6]. Alam explained these effects with a partial charge model [7], and Sugahara showed similar results [4]. Using this trend, all the signals of our experiment were assigned in Table 6.

Table 7 tabulates how the concentrations of some components changed as a function of time during hydrolysis and condensation, and the progressive trends are illustrated in Fig. 9, 10, and 11. Concentrations were determined by integrating the NMR peaks at fixed chemical shift regions and normalizing to the initial DMDES concentration. Errors were determined by relative intensity differences from different Si sites in the same compound.

Table 7: Concentrations (M) of hydrolysis and condensation species change with time. Concentrations were determined by integrating the NMR peaks. Errors are based on intensity difference of Si in the same compound but under different chemical environment. Error is within ± 12%.

time (minutes)	3	13	38	75
D_0^0	0.189	0.074	0.040	0.000
D_0^1	0.725	0.346	0.126	0.049
D_0^2	0.495	0.266	0.106	0.037
C_3	0.000	0.000	0.023	0.020
D_1^0	0.000	0.042	0.069	0.054
D_1^1	0.145	0.327	0.223	0.163
D_1^2	0.102	0.191	0.398	0.267
C_4	0.000	0.000	0.000	0.012
$D_1^0D_2D_1^1$	0.000	0.049	0.136	0.211
$D_1^1D_2D_1^1$	0.000	0.000	0.090	0.175

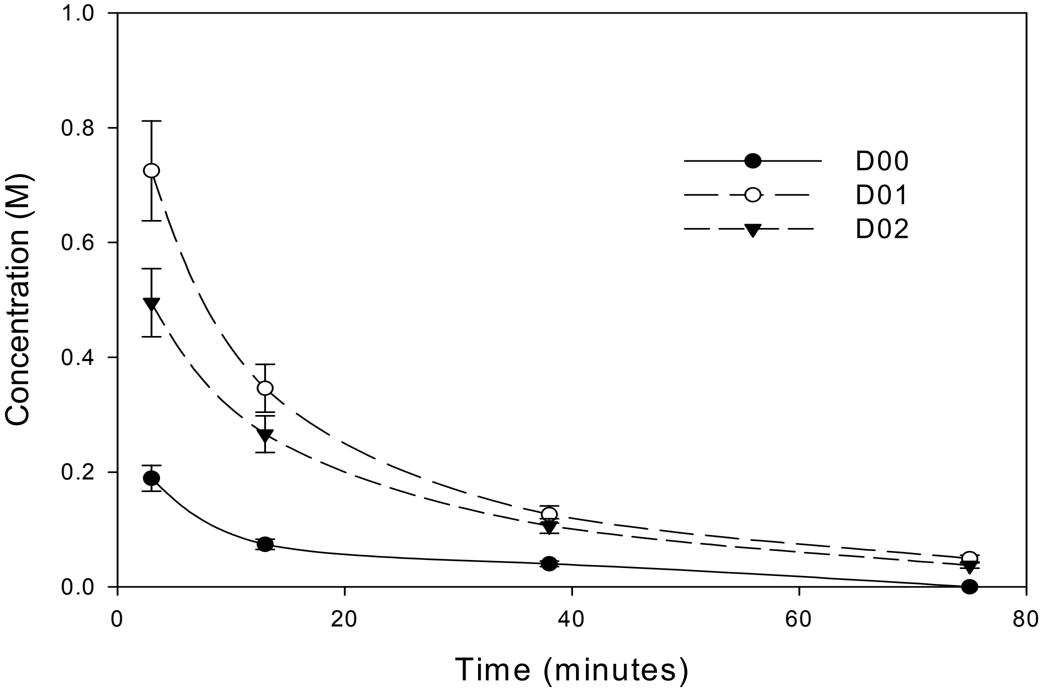

Fig. 9: Monomer concentration changes as a function of time

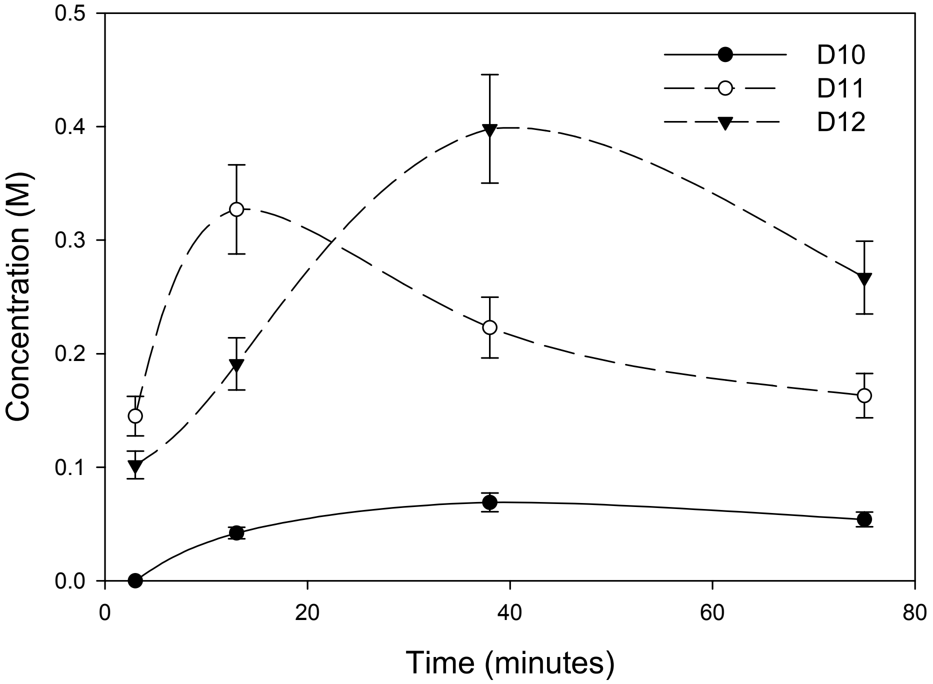

Fig. 10: Dimer concentration changes as a function of time

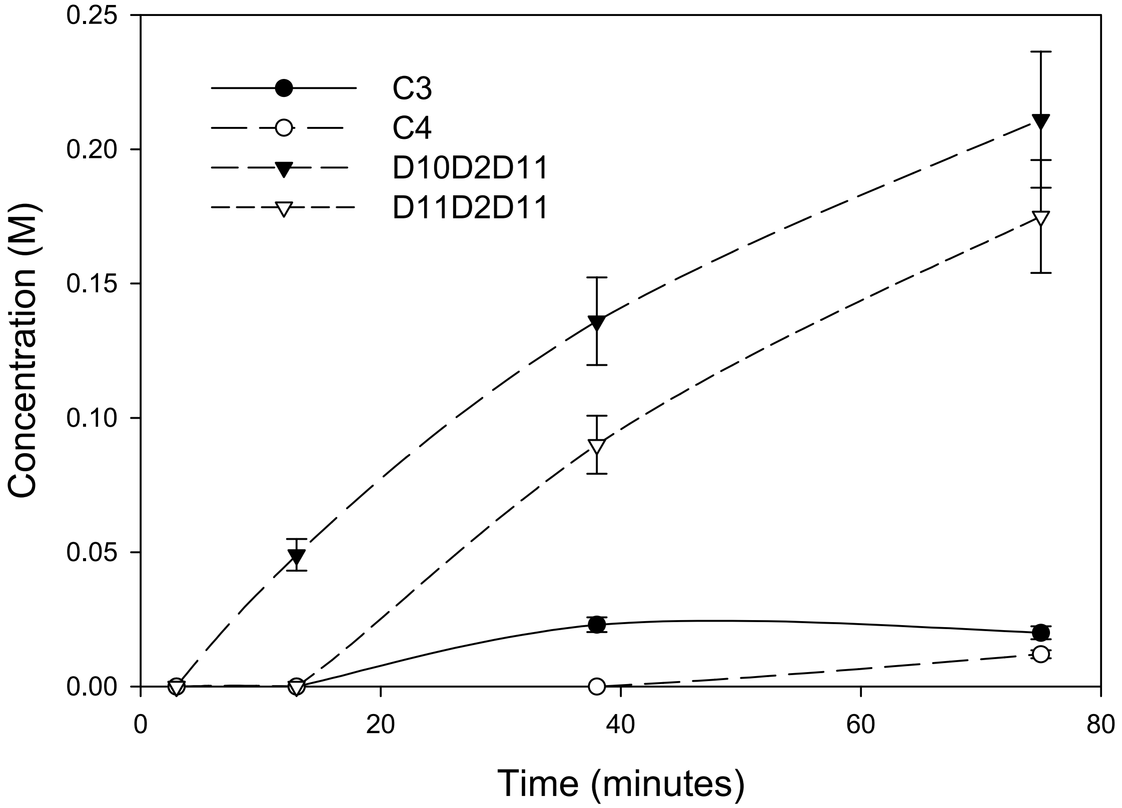

Fig. 11: 3-membered and 4-membered ring and 2 kinds of trimer concentration changes as a function of time

From Table 7 and Fig. 9, 10, and 11, it was obvious that D_1 peaks dominated over most of the experiment time indicating the presence of dimers. Only at 1020 and 1440 minutes, the components in the D_2 region showed comparable magnitude to D_1. 3- and 4-membered rings appeared after half an hour and around an hour, respectively.

McCormick et al. believed that alkyl-substituted silanes could have much higher hydrolysis and polymerization rates than TEOS [2, 8]. From our data, it is clear that DMDES hydrolysis products reach a peak in less than 4 minutes, and the resulting monomers dimerized quickly. Using similar assumptions as made by Fyfe et al., [9] we calculated the hydrolysis constants for the first several minutes for D_0^0 and D_0^1 to be 6.8

and 3.9 liter/(mole*hr). They are larger than the values reported by Sanchez et al [10]. for diethyldiethoxysilane (0.15 liter/(mole*hr)) corresponding to ethyl-substitution, but smaller than the values from Rankin et al. for DMDES (17 ± 3.5 and 11 ± 5.4 liter/(mole*hr)) [2]. We used similar initial DMDES concentrations (1.902 M in this work and 2.24 M for Rankin et al. [2]). Catalyst concentrations (7×10^{-4} M in this work and 2.2×10^{-3} M for Rankin et al. [2]) and water components (D_2O 4.202 M + H_2O 3.890 M in this work and H_2O 4.48 M for Rankin et al. [2]) are quite different. From the data above, we believe that the differences in hydrolysis constants come from the difference in catalyst concentrations.

All the possible reactions and corresponding kinetic constant of DMDES hydrolysis and condensation should be:

$$(Me)_2Si(OEt)_2 + H_2O \xrightarrow{k1} (Me)_2Si(OEt)(OH) + EtOH \tag{1}$$

$$(Me)_2Si(OEt)(OH) + H_2O \xrightarrow{k2} (Me)_2Si(OH)_2 + EtOH \tag{2}$$

$$2(Me)_2Si(OEt)(OH) \xrightarrow{k3} (Me)_2Si(OEt) - O - (OEt)Si(Me)_2 + H_2O \tag{3}$$

$$(Me)_2Si(OEt)(OH) + (Me)_2Si(OH)_2 \xrightarrow{k4} (Me)_2Si(OH) - O - (OEt)Si(Me)_2 + H_2O \tag{4}$$

$$2(Me)_2Si(OH)_2 \xrightarrow{k5} (Me)_2Si(OH) - O - (OH)Si(Me)_2 + H_2O \tag{5}$$

$$(Me)_2Si(OEt) - O - (OEt)Si(Me)_2 + H_2O \xrightarrow{k6} (Me)_2Si(OH) - O - (OEt)Si(Me)_2 + EtOH \tag{6}$$

$$(Me)_2Si(OH) - O - (OEt)Si(Me)_2 + H_2O \xrightarrow{k7} (Me)_2Si(OH) - O - (OH)Si(Me)_2 + EtOH \tag{7}$$

$$(Me)_2Si(OH) - O - (OEt)Si(Me)_2 + (Me)_2Si(OEt)(OH) \xrightarrow{k8} (Me)_2Si(OEt) - O - Si(Me)_2 - O - (OEt)Si(Me)_2 + H_2O \tag{8}$$

$$(Me)_2Si(OH) - O - (OEt)Si(Me)_2 + (Me)_2Si(OH)_2 \xrightarrow{k9} (Me)_2Si(OH) - O - Si(Me)_2 - O - (OEt)Si(Me)_2 + H_2O \tag{9}$$

$(Me)_2Si(OH) – O – (OH)Si(Me)_2 + (Me)_2Si(OEt)(OH) \xrightarrow{k10} (Me)_2Si(OH) – O – Si(Me)_2 – O – (OEt)Si(Me)_2 + H_2O$ (10)

$(Me)_2Si(OH) – O – (OH)Si(Me)_2 + (Me)_2Si(OH)_2 \xrightarrow{k11} (Me)_2Si(OH) – O – Si(Me)_2 – O – (OH)Si(Me)_2 + H_2O$ (11)

$(Me)_2Si(OH) – O – Si(Me)_2 – O – (OH)Si(Me)_2 \overset{k12}{\underset{k13}{\longleftrightarrow}} C_3 + H_2O$ (12)

To determine the kinetics constants for each reaction, the following differential equation groups are used:

For monomers:

$$\underline{d[(Me)_2Si(OEt)_2]/dt} = -k1 * [(Me)_2Si(OEt)_2] * [H_2O]$$

$$\underline{d[(Me)_2Si(OEt)(OH)]/dt} = k1 * [(Me)_2Si(OEt)_2] * [H_2O] – k2 * [(Me)_2Si(OEt)(OH)] * [H_2O] – k3 * [(Me)_2Si(OEt)(OH)]^2 – k4 * [(Me)_2Si(OEt)(OH)] * [(Me)_2Si(OH)_2] – k8 * [(Me)_2Si(OH) – O – (OEt)Si(Me)_2] * [(Me)_2Si(OEt)(OH)] – k10 * [(Me)_2Si(OH) – O – (OH)Si(Me)_2] * [(Me)_2Si(OEt)(OH)]$$

$$\underline{d[(Me)_2Si(OH)_2]/dt} = k2 * [(Me)_2Si(OEt)(OH)] * [H_2O] - k4 * [(Me)_2Si(OEt)(OH)] * [(Me)_2Si(OH)_2] – k5 * [(Me)_2Si(OH)_2]^2 - k10 * [(Me)_2Si(OH) – O – (OH)Si(Me)_2] * [(Me)_2Si(OH)_2]$$

For dimers:

$$\underline{d[(Me)_2Si(OEt) – O – (OEt)Si(Me)_2]/dt} = k3 * [(Me)_2Si(OEt)(OH)]_2 – k6 * [(Me)_2Si(OEt) – O – (OEt)Si(Me)_2] * [H_2O]$$

$$\underline{d[(Me)_2Si(OH) – O – (OEt)Si(Me)_2]/dt} = k4 * [(Me)_2Si(OEt)(OH)] * [(Me)_2Si(OH)_2] + k6 * [(Me)_2Si(OEt) – O – (OEt)Si(Me)_2] * [H_2O] – k7 * [(Me)_2Si(OH) – O – (OEt)Si(Me)_2] * [H_2O] - k8 * [(Me)_2Si(OH) – O – (OEt)Si(Me)_2] * [(Me)_2Si(OEt)(OH)] - k9 * [(Me)_2Si(OH) – O – (OEt)Si(Me)_2] * [(Me)_2Si(OH)_2]$$

$$\underline{d[(Me)_2Si(OH) – O – (OH)Si(Me)_2]/dt} = k5 * [(Me)_2Si(OH)_2]^2 + k7 * [(Me)_2Si(OH) – O – (OEt)Si(Me)_2] * [H_2O] - k9 * [(Me)_2Si(OH) – O –$$

$(OEt)Si(Me)_2]$ * $[(Me)_2Si(OH)_2]$ - k10 * $[(Me)_2Si(OH) – O – (OH)Si(Me)_2]$ * $[(Me)_2Si(OH)_2]$

To simplify, the hydrolysis of DMDES can be expressed by following equations:

$D_0^0 + H_2O \longrightarrow D_0^1 + EtOH$ (1)

$D_0^1 + H_2O \longrightarrow D_0^2 + EtOH$ (2)

And the consequent dimerization can be:

For D_1^0:

$D_0^0 + D_0^1 \longrightarrow D_1^0 + EtOH$ (3)

$D_0^1 + D_0^1 \longrightarrow D_1^0 + H_2O$ (4)

For D_1^1:

$D_0^0 + D_0^2 \longrightarrow D_1^1 + EtOH$ (5)

$D_0^1 + D_0^1 \longrightarrow D_1^1 + EtOH$ (6)

$D_0^1 + D_0^2 \longrightarrow D_1^1 + H_2O$ (7)

For D_1^2:

$D_0^2 + D_0^2 \longrightarrow D_1^2 + H_2O$ (8)

$D_0^2 + D_0^1 \longrightarrow D_1^2 + EtOH$ (9)

According to Pouxviel et al., unhydrolyzed TEOS will not participate in the dimerization [11]. Under acidic conditions, the water-producing dimerization rate would be much larger than alcohol-producing condensation. During the initial time period, we can ignore the unhydrolyzed DMDES (D_0^0) dimerization. Then for D_1^0, D_1^0, and D_1^2, reactions (4), (7), and (8) would dominate. From (4) we can see that to produce 1 mole of D_1^0, 2 moles of D_0^1 were consumed. In the first 13 minutes, the consumption of D_0^1 should be 0.324 M (2 × $[D_1^0]$ + 1 × $[D_1^2]$ + 1 × $[D_1^0D_2D_1^1]$). Using the same methodology, consumption of D_0^2 is 0.894 M (2 × [D_1^1] + 1 × [D_1^2] + 1 × [$D_1^0D_2D_1^1$]). Their consumption ratio is 2.76.

For cyclization (ringed-members formation), Ng and McCormick [8] proposed scheme 1 in Fig. 12 for acid- catalyzed TEOS, which included both bimolecular (three-silicon linear species react with monomers) and unimolecular reactions (four-silicon linear species) for four-membered ring formations. In 1998, Rankin [2] proposed scheme 2, which favored two ways for 4-membered ring formation -through a monomer-trimer and dimer-dimer reactions. Both schemes are shown in Fig. 12.

In Scheme 2 of Fig. 12, 3-membered ring and linear species are shown to be reversible. The relative concentration of C_3 increased initially and then fell off. Consumption of C_3 can only progress through ring opening forming 3-membered linear structures, suggesting C_3 was not as energetically favored as 3-membered linear structures. Through 17 hours and 24 hours, C_4 increased dramatically, but no monomers were detectable in the system. Therefore, C_4 must be formed through dimer-dimer condensation instead of monomer-trimer reaction. Using quantum mechanical calculations, Hench et al. stated that a cyclic siloxane tetramer was favored over a chain-like tetramer [12]. In our systems, C_4 increased with D_2. So during an experimental times, this trend was not appreciable. Without monomer-trimer reactions or appreciable unimolecular linear 4-membered structure bending up from NMR spectra, 4-membered cyclic species must be constructed from dimer-dimer reaction. We have modified Scheme 2 from Rankin et al. [2] to describe our model of cyclization (Fig. 12).

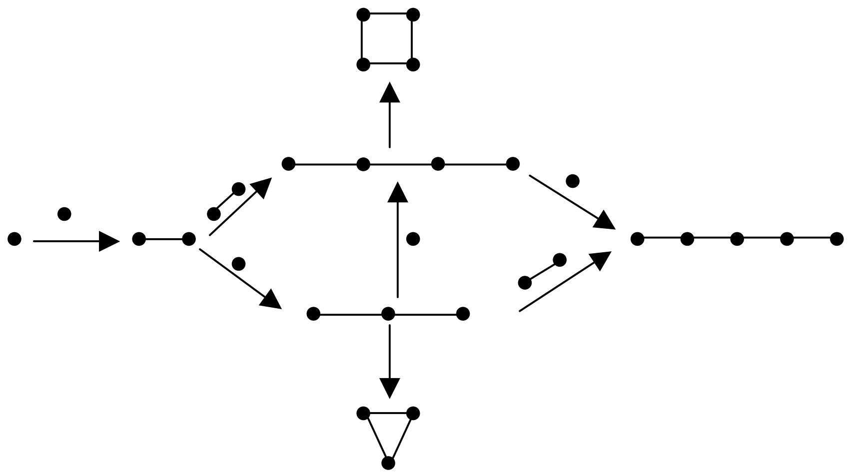

Scheme 1

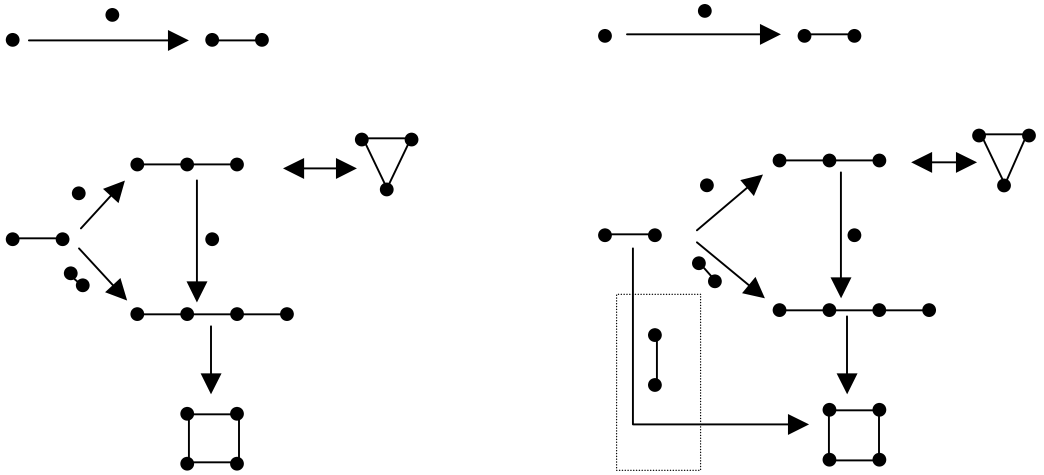

Scheme 2 Our modified scheme

Fig. 12: Scheme 1 by Ng and McCorrick (1996), Scheme 2 by Rankin et al. (1998), and our modified model for possible cyclization mechanism. The dotted box shows the difference of our model with Scheme 2. Black points represent silicon sites (· represents monomers), lines represent bonds between silicon sites (·—· represents dimers and so on), and ▽ and □ represent 3-membered and 4-membered rings. [2].

5.2 TEFS Xerogel films

TEFS is an unusual silica gel precursor. Previous studies showed that TEFS-based films could have low dielectric constant (k) values, high Young's modulus, and hardness [13 – 15]. It is believed that fluorine-incorporation and intrinsic porosity resulted low-k values and the neck thickening between clusters during gelation and aging promoted superior high mechanical properties.

Gelation usually occurs when oligomeric clusters impinge on each another connecting to a three dimensional network. Connectivity is low due to limited linkage between clusters, leading to a weakly bonded network. TEFS gels in different manner. TEFS can gel very fast; rapidly forming interconnected three-dimensional network before all precursor is condensed, leaving a wealth of monomers or low molecular oligomers. Following gelation, these monomers and / or oligomers will react with the networks; thickening the linkages between particles and strengthening the network. Comparing these structures with those of silica gels processed from other precursors (i.e., TEOS or TMOS), microstructures are very different [16]. Gels from other precursors have very individuated features with only a small amount of material forming links while TEFS gels have larger diameter linkages which give the network high strength. These structures have "coral reef" morphology.

5.2.1 FTIR Spectra of TEFS Xerogels

Typical FTIR spectra show F – Si bonding in TEFS xerogel films in Fig. 13. Although their compositions differed, the two spectra shared some common features. The silica network skeleton had two vibrational modes: bending (~ 800 cm^{-1}) and stretching (1000 – 1200 cm^{-1}). OH groups have H_2O bending (~ 1670 cm^{-1}), O – H stretching (~ 3300 cm^{-1}) and SiO – H stretching (~ 3650 cm^{-1}) modes. CH groups have a stretching mode (3000 – 2900 cm^{-1}) and a bending mode (1450 – 1380 cm^{-1}). Si – F bonding was assigned to 940 cm^{-1}. Fig. 14 showed the oxygen and silicon relevant movements and Table 8 summarized peak assignment.

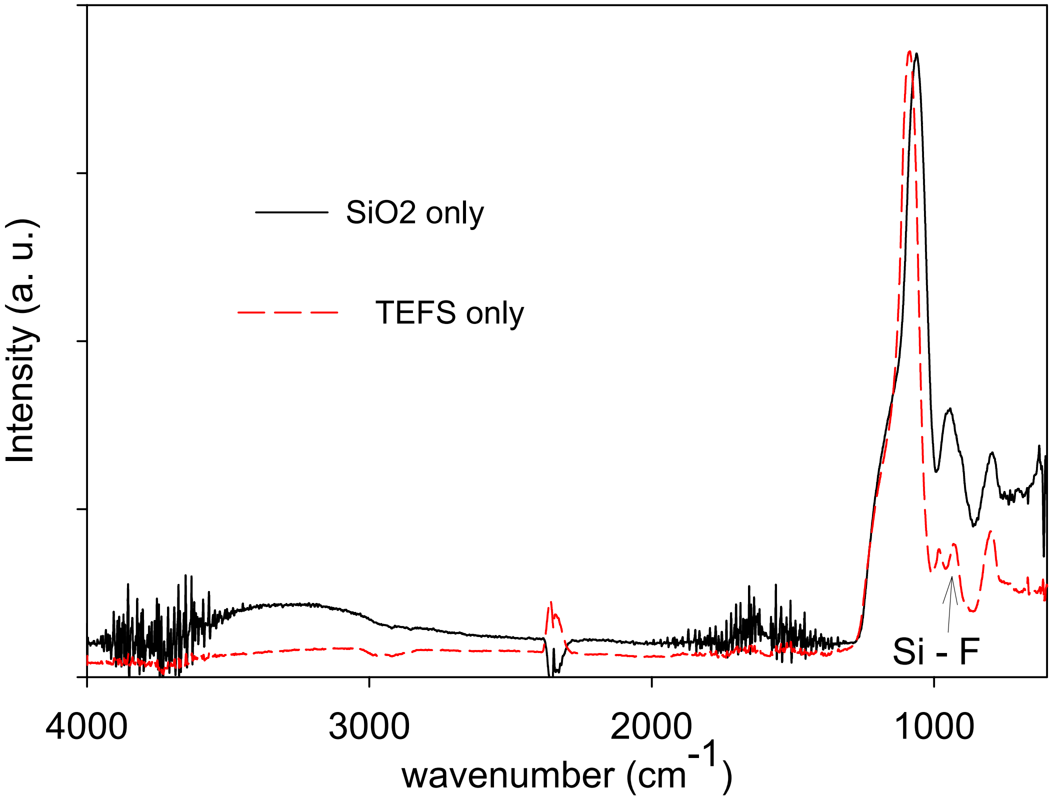

Fig. 13: Typical FTIR spectra of SiO_2, TEFS at 4000 to 600 cm^{-1} wavenumber range

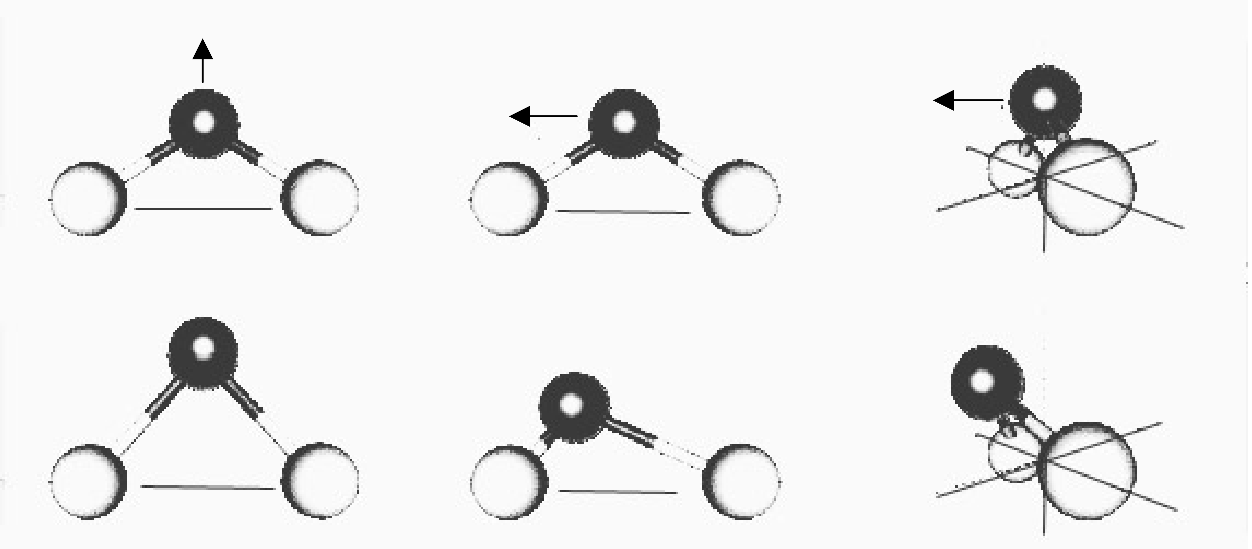

Fig. 14: Schematic representation of the vibrational motions of oxygen atoms (dark) with respect to the bridged silicon atoms (gray): symmetric stretching motion along the bisector of the Si–O–Si bridging angle, antisymmetric stretching motion parallel to the Si–Si line between the two bridged cations, rocking motion perpendicular to the Si–O–Si plane [17].

Table 8: Summary of peak assignments. A range was given for each mode due to several possible peaks or peak shift due to structure changes.

Wavenumber (cm^{-1})	Band assignment
3750 – 3000	O – H stretching
3000 – 2800	C – H stretching
1700 – 1600	H – O – H bending
1460 – 1380	C – H bending
1270 – 1255	Si – CH_3 stretching
1330 – 980	Si – O – Si stretching
980 – 970	Si – OH stretching
950 – 930	Si - F stretching vibration
810 – 790	Si – O - Si bending
770 – 750	Si – CH_3 bending

FTIR spectra are widely used for silica compositional and structural analysis. There have been disagreements among scientists regarding peak assignments, especially for Si – O – Si stretching mode (1300 – 1000 cm^{-1} region) and fluorine in the microstructures of the materials studied to date.

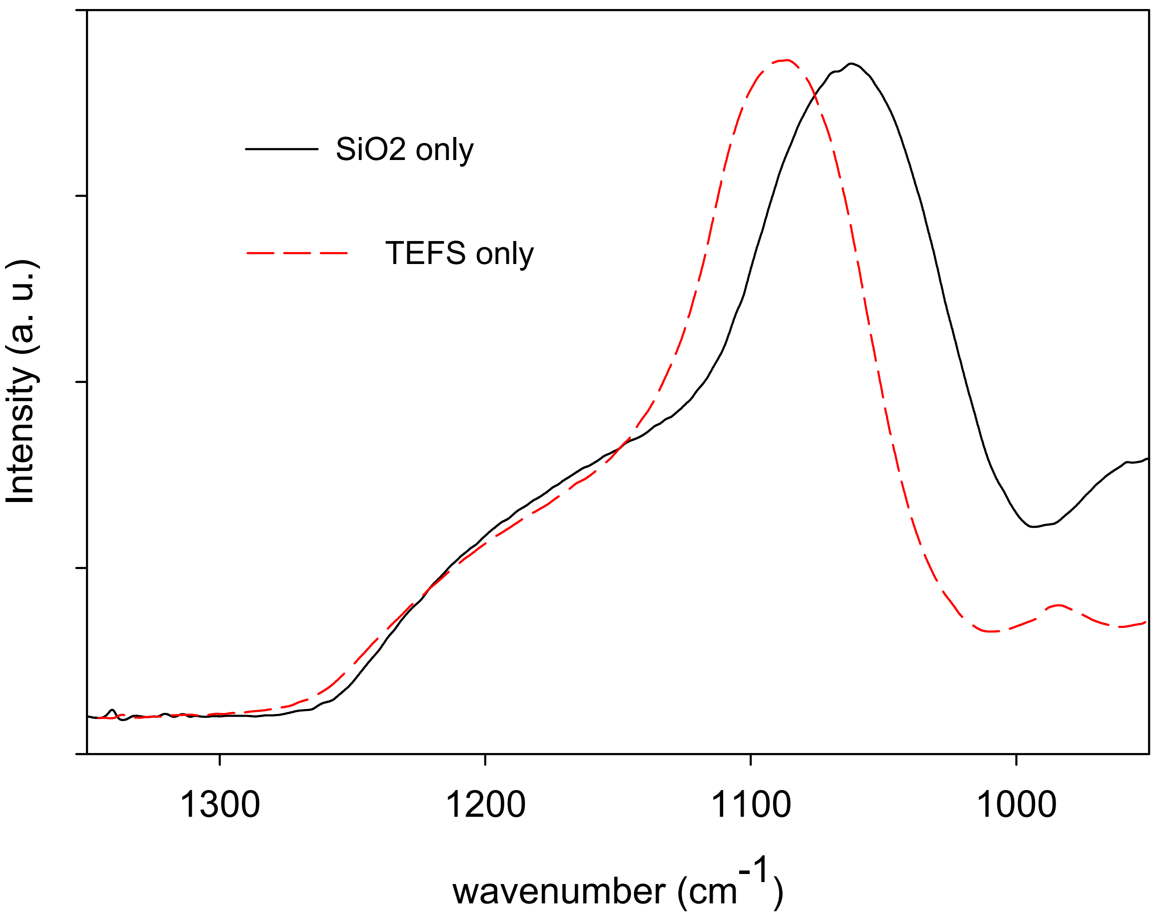

Fig. 15: FTIR spectra of SiO_2-only and TEFS-only films in 1350 to 950 cm^{-1} range

It is generally agreed that the strong and broad absorption band of silica (1300 – 1000 cm^{-1}) is due to asymmetric stretching of the inter-tetrahedral oxygen atoms, [18-21] i.e., displacement parallel to the axis of the two silicon atoms to which the oxygen atom is bonded, shown in Fig. 14 and 16 [22]. However, as oxygen atom stretches relative to silicon atoms, silicon atoms are not static. This band also involves significant silicon atom motion, which depends on the local bonding structures. In an acid-catalyzed sol-gel silica coating FTIR transmission spectra, Parrill [22] divided the 1300 – 1000 cm^{-1} region into four peaks: 1230 cm^{-1} for Si – O – Si oxygen asymmetric stretching, 1140 cm^{-1} for cyclic Si – O, 1093 cm^{-1} for Si – O – C oxygen stretching, and1066 cm^{-1} for another Si – O – Si oxygen asymmetric stretching. Using a semi empirical quantum molecular orbital (MO) method (PM-3 in MOPAC 6.1) to analyze the structural changes responsible for the spectral shifts, Chia et al. concluded that silica 5- or 6-membered rings should dominate but not 4-membered rings [23].

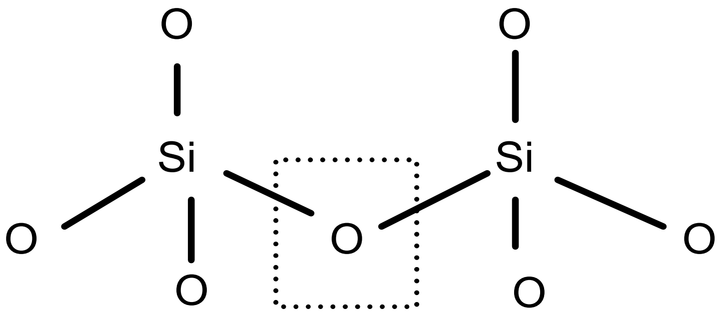

Fig. 16: Oxygen between two tetrahedrons

Without specifying vibrational modes for each peak in the 1300 – 1000 cm^{-1} region, Martinez et al. divided that region into five peaks to show the structural disorder of sol-gel silica films [24] Wang et al. fitted the broad band at 1300 – 1000 cm^{-1} with four Gaussian functions for a cured MSQ film [25]. This work assigned the peak at 1190 cm^{-1} to O – Si – O short chains with CH_3 or OH terminal bonds, the peak at 1134 cm^{-1} to short chains with oxygen terminal bonds, the peak at 1084 cm^{-1} to long chains with CH_3 or OH terminal bonds, and the peak at 1036 cm^{-1} to long chains with oxygen terminal bonds. This assignment was verified and found consistent with curing the MSQ films under different conditions.

A literature review shows that there are some difficulties concerning the assignment of the vibrational modes due to cyclic species in the 1300 – 1000 cm^{-1} region. Difficulties arise because of the possible overlapping of vibrations assigned to different species. A clear understanding between possible vibrational bands has not yet been reached.

There is some disagreement about the presence of fluorine in the microstructures of fluorinated silica films. In plasma enhanced chemical vapor deposited (PECVD) fluorine-doped silicon dioxide films using TEOS and C_2F_6, Usami et al. proposed the presence of $Si – F_n$ species at high C_2F_6 flow, but these species were supposed to evaporate during the deposition and did not remain in the film since the substrate wafer was heated to 360°C during deposition [26]. Later, Kitoh et al. found that in a lower RF power PECVD system using TEFS as precursor, $Si – F_n$ bonds increased although, the substrate was heated to 400°C during the deposition [27]. They proposed that due to incomplete decomposition of the TEFS precursor, H_2O could be converted to HF and further converted to Si – F bonds at the wafer surface. Contrary to Usami, Yoshimaru et al. believed they found the $Si – F_n$ bonds under the same experimental setup [28]. The analysis resulted in the assignments of FTIR peak at 925 cm^{-1} and 985 cm^{-1} to $Si – F_2$, symmetrical and asymmetrical stretching respectively as well as peak at about 940 cm^{-1} to Si – F, combining FTIR spectra and Raman data. Initially, one peak was observed at about 940 cm^{-1}, which is assumed to be Si – F. This peak assignment was based on NMR data on fluorinated silicate glass where most of the fluorine preferentially formed monofluoride sites with a small number of difluoride sites [29]. As the fluorine content increases, the peaks at about 925 cm^{-1} and 985 cm^{-1} begin to form. Upon exposure to humidity, the peaks decomposed into one Si-F peak at 928cm^{-1} [30]. This peak assignment was rationalized by a potential barrier studying of interactions between F_n – Si - $(-O-)_{4-n}$- and water by Nakasaki [31] and Kaneta [32]. As the number of fluorine bonded to silicon atoms increased, the potential barrier height decreased. So they assumed that Si – F_2 bonds would react with H_2O before the Si – F bonds, therefore, Si – F bonds would dominate. Han et al. confirmed the peak assignments with isotopic substitution of ^{16}O with ^{18}O in the fluorinated silica films deposited by PECVD using SiF_4 and O_2 at 250°C substrate temperature [33]. They rationalized the peak assignment due to the invariance of the 940 cm^{-1} position against the isotopic substitution, confirming the band of 940 cm^{-1} belonged to Si – F_n species instead of SiO – F. The Si – F_2 peaks were assigned at 990 cm^{-1} and 920 cm^{-1} while the Si – F peak was assigned at 950 cm^{-1}. Using SiF_4 / TEOS or / and TEFS / TEOS as PECVD precursor, Bhan et al. [34] and Rana et al. [35] reported similar peak assignments.

Contrary to the above data, Lucovsky et al. stated there was no definitive evidence of the presence of Si – F_2 species [36 - 38]. A kinematic study of Si – F_2 vibration would imply a splitting between the peaks at about 980 cm^{-1} and 920 cm^{-1} of about 90 cm^{-1} instead of the reported 68 cm^{-1}. Also, to confirm the presence of Si – F_2, the bending and rocking modes would need to be observed. Lucovsky et al. collected FTIR spectra down to 150 cm^{-1}, but no such peaks were observed. So they concluded that only Si – F bonds were present.

Although Campostrini et al. observed Si – F_2 bonding in the TEFS precursor (purchased from ABCR) by gas chromatography [39], we believed that in TEFS xerogel films, only Si – F bonds exist since water in our system would change Si – F_n bonds to Si – F bonds [30] (if there were any Si – F_n bonds). Consequently, the IR peak at 950 – 930 cm^{-1} was assigned to Si – F bonds. The peak at 1300 – 1000 cm^{-1} contains linear and cyclic Si – O – Si structures with ringed-species at the higher wavenumber shoulders. Other peaks are: 3700 -3300cm^{-1} belongs to OH or H_2O, 3000 – 2800 cm^{-1} to CH groups, 1275 – 1255 cm^{-1} to Si – CH_3.

5.2.2 Fluorine Effects in Lowering k values

Although fluorine has been successfully used to lower silica dielectric constant, the mechanism is still under debate. Due to its highest electronegativity, substitution of oxygen with fluorine was thought to increase Si – O bond strength within the silica network, which was manifested by the blueshift of the Si – O stretching mode at about 1080 cm^{-1}. Usami et al. corroborated this statement by observing a Si 2p binding energy shift with fluorine concentration under XPS [24]. They found that the Si 2p binding energy monotonically increased as fluorine content increased and they attributed the increase to fluorine substitution. With fluorine addition, Si – OH bonds decreased. Using TEFS as PECVD precursor, Kitoh et al. found that fluorine could hinder moisture absorption in the film [27]. Mizuno et al. observed that even a small amount of fluorine could reduce the Si – OH content sharply [40]. They believed that fluorine and OH obviously competed for the available Si sites, and the Si – F bonding was preferred due to the highest electronegativity of fluorine. The elimination of Si – OH was beneficial to reduce the dielectric constant since the OH bond has high dipolar contributions to k (k_{H2O} = 79 -81). Additionally, the highly electronegative fluorine could draw electrons closer to itself, resulting in a change in the Si – O network bonding characteristics from that of the tetrahedral sp^3 orbital to the more planar, and less polarizable sp^2 orbital [40].

By examining the k values over a range of frequencies, Lim et al. found that fluorine impacted ionic polarization considerably more then the electronic polarization [41]. They suggested that a decrease in Si – O vibrational modes due to appearance of Si – F bonds would be the main factor related to the decrease in the dielectric constant. Using ab-initio calculations, Lucovsky et al. concluded that due to fluorine substitution, effective partial charge on Si sites was reduced for both stretching and bending vibrational modes, and Si – F vibrations had lower effective partial charges than Si – O vibration at the main stretching modes [36 - 38]. These two factors led the dominant decrease in k values. Lubguban et al. shared the same idea [42].

To explain the blueshift of Si – O stretching mode at about 1080 cm^{-1} and the corresponding full width at half maximum (FWHM) decrease, Han et al. [33] proposed that fluorine addition led to the Si – O – Si bond angle relaxation in the silica network accompanied by a lower density than dense SiO_2. Yoshimaru et al. believed that fluorine would incorporate within a silica network where Si – O – Si bonding groups with smaller bond angles were defect centers and more reactive, comparing the reactions among H_2O and CVD silica networks [28]. Kim et al. explained the Si – O – Si bond angle relaxation using a “Bonding Structure Model” [43]. They thought that due to the highest electronegativity, fluorine would draw the electronic clouds of Si – O bonds to itself and increase the Si – O – Si bond angle. It is schematically shown as following:

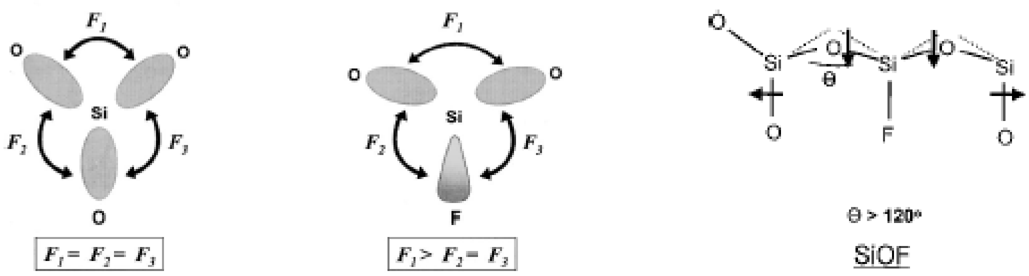

Fig. 17: “Bonding Structure Model” from reference [43]

In an effort to quantify electronic and ionic additions to the dielectric constant of plasma deposited SiO_2 films, Han et al. employed ATR – FTIR spectroscopy and spectroscopic ellipsometry to separate electronic and ionic contributions for lowering the dielectric constant values due to fluorine incorporation [44]. At lower fluorine concentrations, Si – O – Si bond angle relaxation and subsequent density reduction appeared to be largely responsible for the electronic component decreasing. The ionic component, mainly due to Si – O – Si stretching vibrations, also decreased with increasing F concentration. This decrease was attributed to the replacement of more ionic SiOH bonds with Si – F.

In our fluorinated silica xerogel films, fluorine concentration was measured low (about 1 atomic percent, will be discussed in detail later). And in typical sol-gel processes (unlike PVD or CVD), the silica network has plenty of time to relax its structure no matter with or without fluorine combination. So in our sol-gel fluorinated silica films, the mechanism for fluorine decreasing dielectric constant is mainly due to replacement of Si – O bonds by less ionic Si – F bonds and the resulting void formation leading electronic component decrease.

5.2.3 Fluorine Concentration Measurements

Fluorine concentrations of TEFS xerogels were measured by XPS (Fig. 18), DSIMS (Fig. 19), and NRA (Fig. 20) using reaction $^{19}F(p, \alpha\gamma)^{16}O$ with known thickness samples of CaF_2 as standard reference. Results confirmed that fluorine atomic concentration in TEFS xerogels although constant as a function of depth was only 0.8 to 1.7 atom%. During TEFS hydrolysis and condensation, most fluorine element was lost (fluorine atomic concentration should be 1 / (1 + 1 + 1.5) [$FSiO_{3/2}$ -], e.g. 28.57 %). The reason may be due to Si – F bonds react with water to form SiOH and HF.

F1s XPS spectrum showed a fair symmetric peak (Fig. 18), which means fluorine in samples has only one chemical state. This corroborated our guess that in a TEFS xerogel only Si – F species exist.

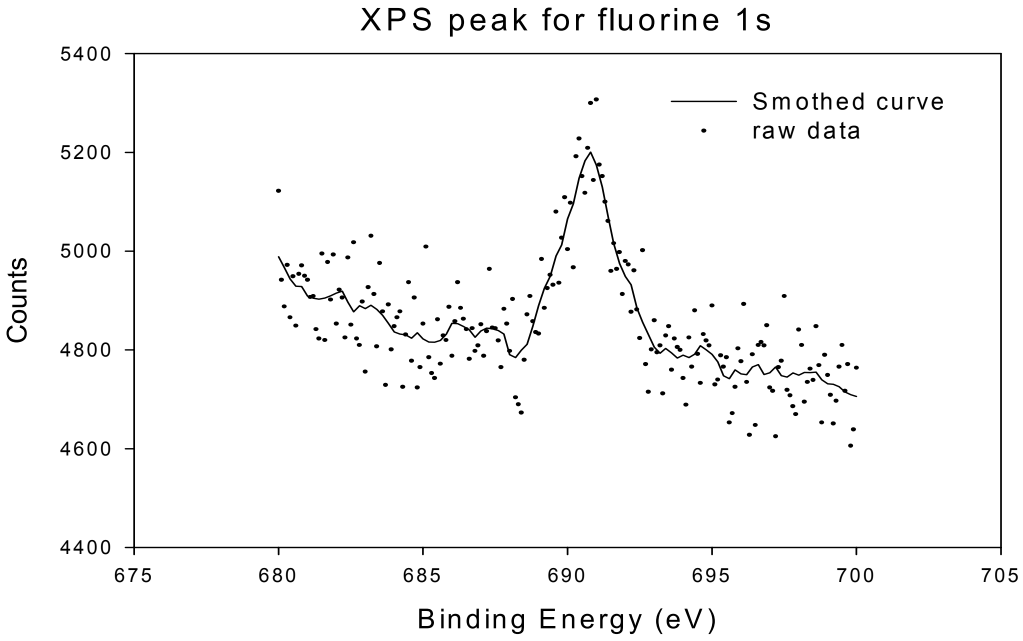

Fig. 18: Fluorine 1s XPS peak

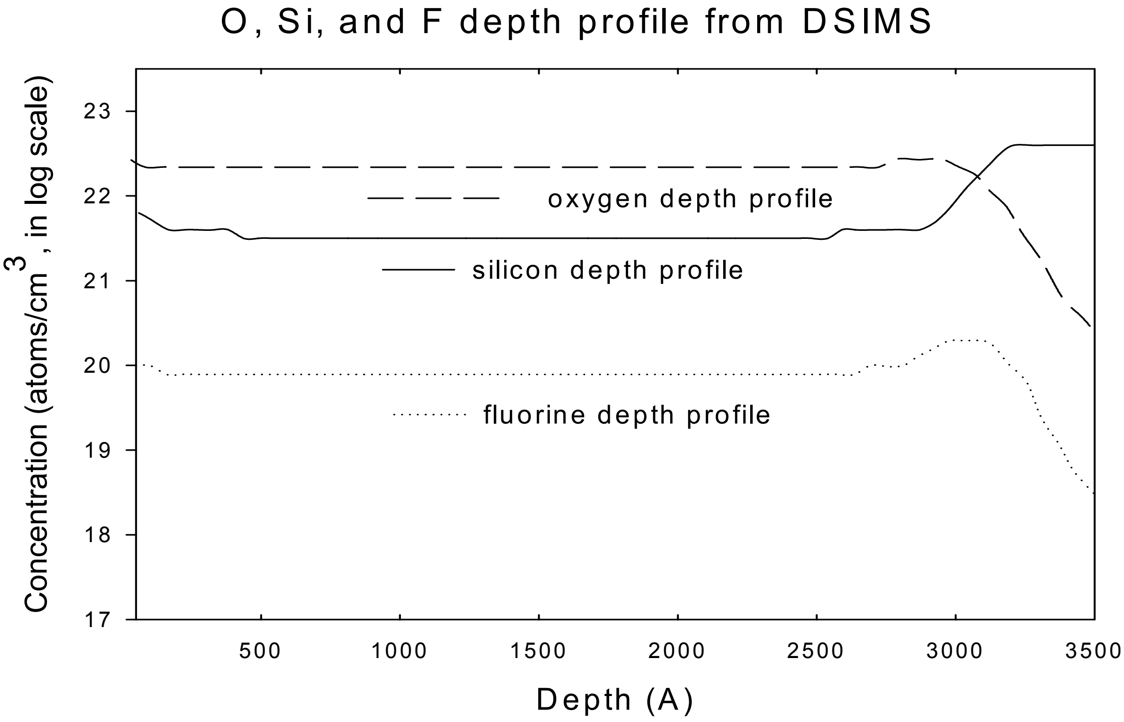

Fig. 19: Oxygen, silicon, and fluorine elemental compositions from DSIMS

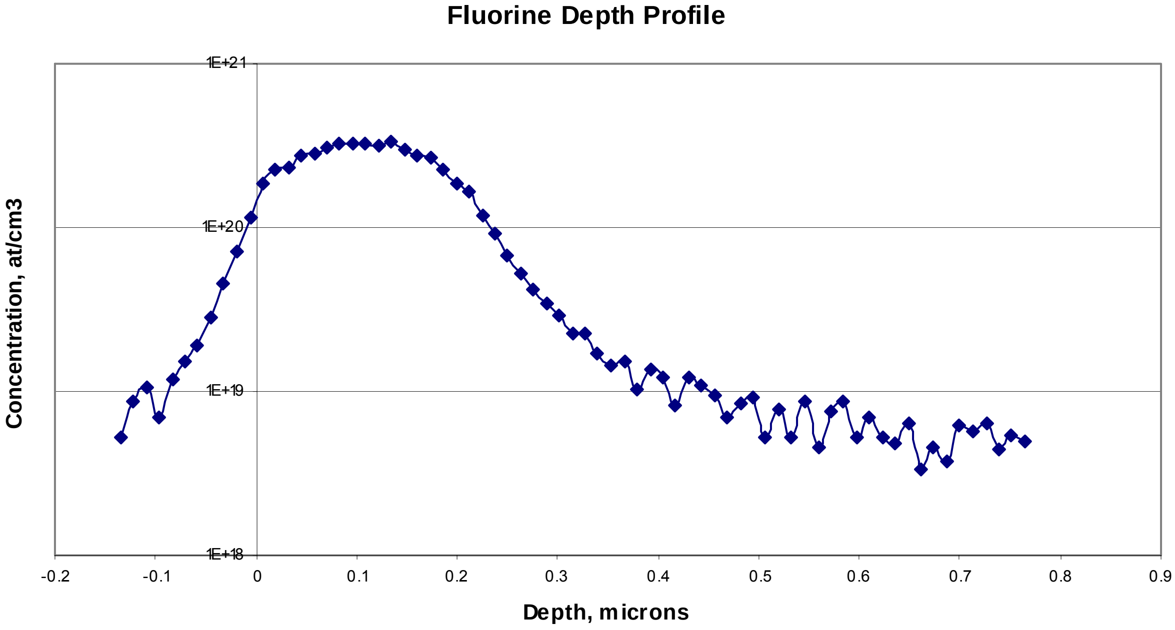

Fig. 20: Fluorine depth profile in TEFS-only film by NRA spectrum

5.2.4 E & H of TEFS Xerogel films

Compared with other low-k candidates, TEFS xerogel low-k films stand out due to their intrinsic high mechanical properties and relatively low dielectric constants. We believe that previously described microstructure rendered TEFS its superior properties.

Table 9: Electrical and mechanical property comparison between several low-k materials

Properties	TEFS xerogel (UNT)	MSQ (JSR)[45]	Silica xerogel (Honeywell)[46]	Polymer low-k (Dow Chem.)	Porous polymer low-k (Dow Chem.)
Dielectric constant	2.3	2.3	2.2	2.7	2.3
Elastic modulus (GPa)	12	4	6.4	3.8	2.65
Hardness (GPa)	1.0	0.3	0.8	0.25	0.15

5.2.5 TEFS Gelation Modeling

We believe that the presence of fluorine created this “coral reef” morphology and, consequently, the enhanced mechanical properties of TEFS. As discussed in Section 5.2, unlike most silicon sol-gel systems, TEFS forms gel networks very rapidly and thickens linkages between particles. To explain the difference, the following model was proposed:

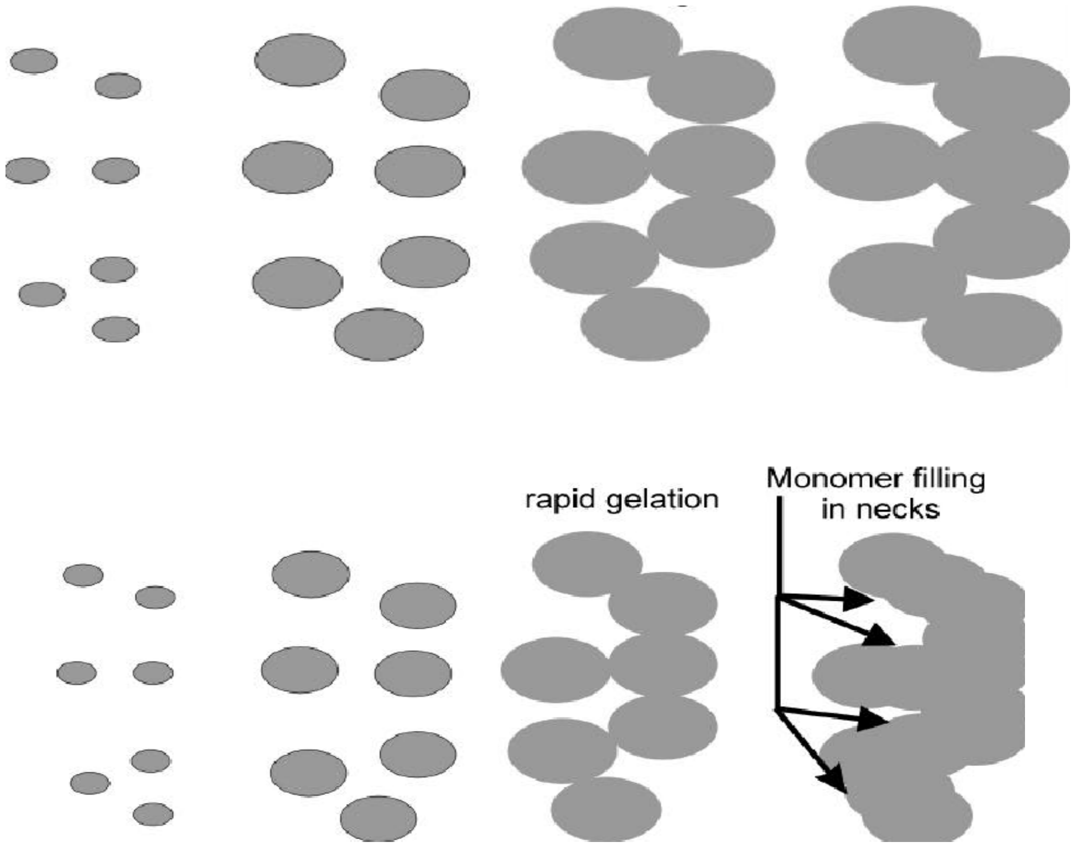

Fig. 21: Proposed gelation model for ordinary precursors and TEFS [47]

During hydrolysis and poly-condensation, ordinary sol-gel precursors generally follow heritage growth: monomers to dimers, to trimers, to tetramers, etc. After some time, resulting clusters impinge on each other. To gel, a system has a relatively high extent of condensation (80 - 90%) so that enough cluster cores can form and sufficient impingement is possible to produce linkages for a spanning network. Linkages or necks between particles are the weakest part of the structure due to low bond density.

TEFS gels at low extents of condensation (~ 60 %), which means it can gel with a wealth of monomer. These monomers or low degree connected oligomers can reinforce the weak linkages, so strengthen the network and structure. The reason why TEFS gels in this fashion is due to fluorine inhibition of ring formation during gelation.

5.2.6 Fluorine Effect Limitations

Although fluorine can effectively lower dielectric constant in silica xerogel films, it has two main drawbacks:

- during sol-gel reactions, fluorine is lost due to Si – F reactions with water, which does not happen in CVD systems. TEFS has some SiOH bonds. Water absorption will increase dielectric constant, counterbalancing the benefit of fluorine introduction [26, 30, 38, 40, 48].

  $Si - F + H_2O \longrightarrow Si - OH + HF$ (corrosive HF outgassing)

  $Si - F + H_2O \longrightarrow Si - F \ldots H_2O$ (strong hydrogen bonding).

- research shows that fluorine incorporation into silica has a concentration limitation although different researchers give different values. Therefore, by fluorine alone, it is impossible to further decrease the dielectric constant [26, 34, 35, 49].

Basing on our understanding of TEFS xerogels and DMDES hydrolysis and condensation, a new hybrid xerogel was created by introducing pregeled DMDES into TEFS sols, trying to combine benefits from both TEFS and DMDES.

5.3 Hybrid Xerogels

5.3.1 FTIR Spectra

Typical FTIR spectra of the hybrid xerogels were shown in Fig 22 and 23. For comparison, FTIR spectra for SiO_2-only and TEFS-only xerogels were also shown.

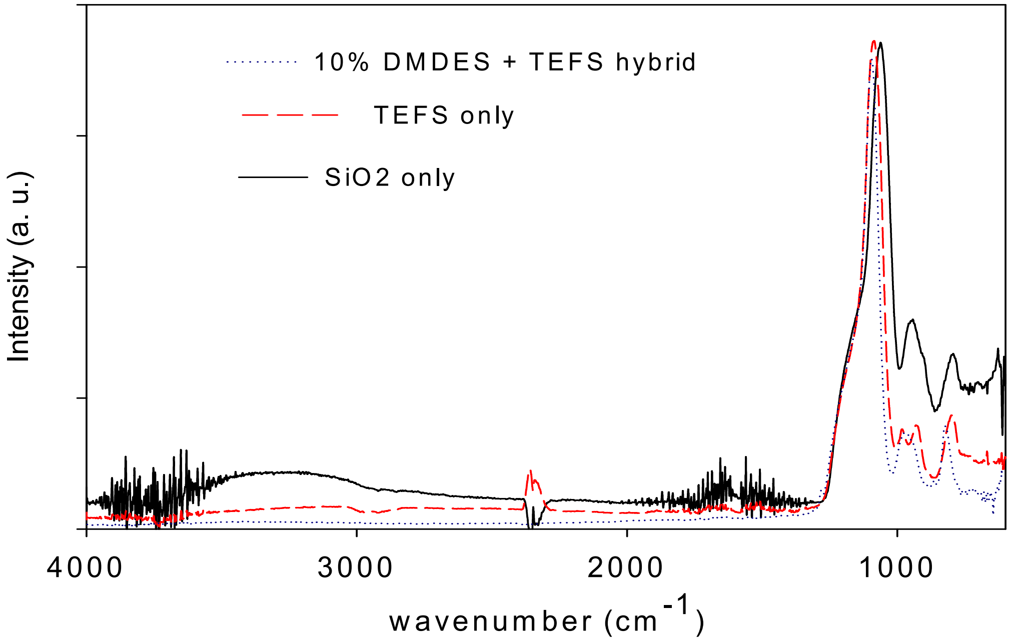

Fig. 22: FTIR spectra of 10 atom. % DMDES + TEFS, TEFS-only, and SiO_2-only

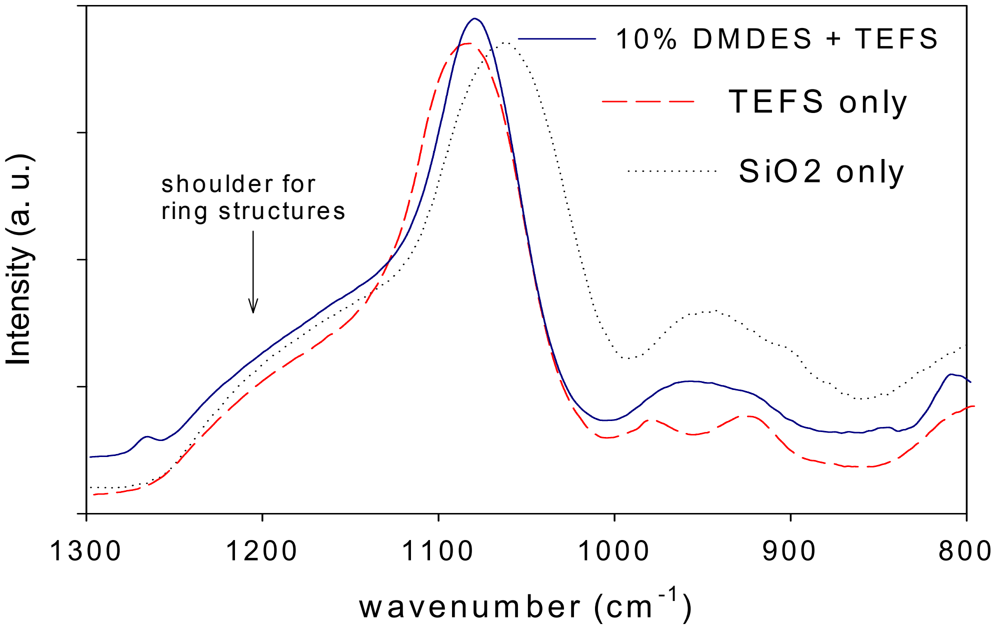

Fig. 23: FTIR spectra of SiO_2, TEFS, 10 % DMDES + TEFS hybrid films: at region in 1300 – 800 cm^{-1}

Fig. 22 and 23 show FTIR spectra of SiO_2, TEFS, and TEFS + DMDES films. All spectra show the typical Si – O – Si antisymmetric stretching mode in the range of 1000 - 1200 cm^{-1}. The peak positions of TEFS and TEFS + DMDES films show a blueshift and narrower FWHM due to strengthened Si – O bonds [50]. Usually Si – O bonds show several vibrational peaks in the 1300 – 800 cm^{-1} region. Peak fitting shows that taller peaks at higher wavenumbers come from Si – O cyclic structures and peaks at lower wavenumbers correspond to linear species [51]. TEFS+DMDES films have a bigger shoulder at higher frequency because more Si – O – Si ringed structures have been introduced by DMDES polymerization and exhibit a composite peak of Si-O (around 980 cm^{-1}) and Si-F (around 930 cm^{-1}) peaks. Methyl group addition in the xerogel was manifested by a Si – C peak at 1270 cm^{-1} and lowered water peak intensity.

Although DMDES can be introduced into the TEFS matrix to form a hybrid xerogel, shown in Fig. 22, DMDES and TEFS have different kinetics of hydrolysis and condensation. The time and concentration of DMDES introduction must be optimized to permit DMDES to function as silica network modifier.

5.3.2 DMDES Concentration Determination

Fig. 24 showed the FTIR spectra of the hybrid xerogel in the 1500 – 700 cm^{-1} region. Spectra of TEFS with different molar ratios of DMDES mixed at the same time were collected after drying of the gels resulted. It was observed that as the DMDES concentration decreased, the Si – C peak (1265 cm^{-1}) intensity decreased. As 35% DMDES introduced, the Si-C peak was fairly detectable. On the other hand, the Si – F peaks (935 cm^{-1}) intensity increased as the DMDES concentration decreased. At concentrations greater than 35% DMDES, the Si – F peak (935 cm^{-1}) overlapped with the Si – OH peak (986 cm^{-1}) forming a composite peak which tilted toward S – OH side. Below 30% DMDES, peaks were clearly separate, and a single Si – F peak could be observed at about 935 cm^{-1}. As DMDES concentration went down, Si – F peak intensity increased accordingly. This is reasonable because TEFS molar concentration goes up as DMDES concentration goes down.

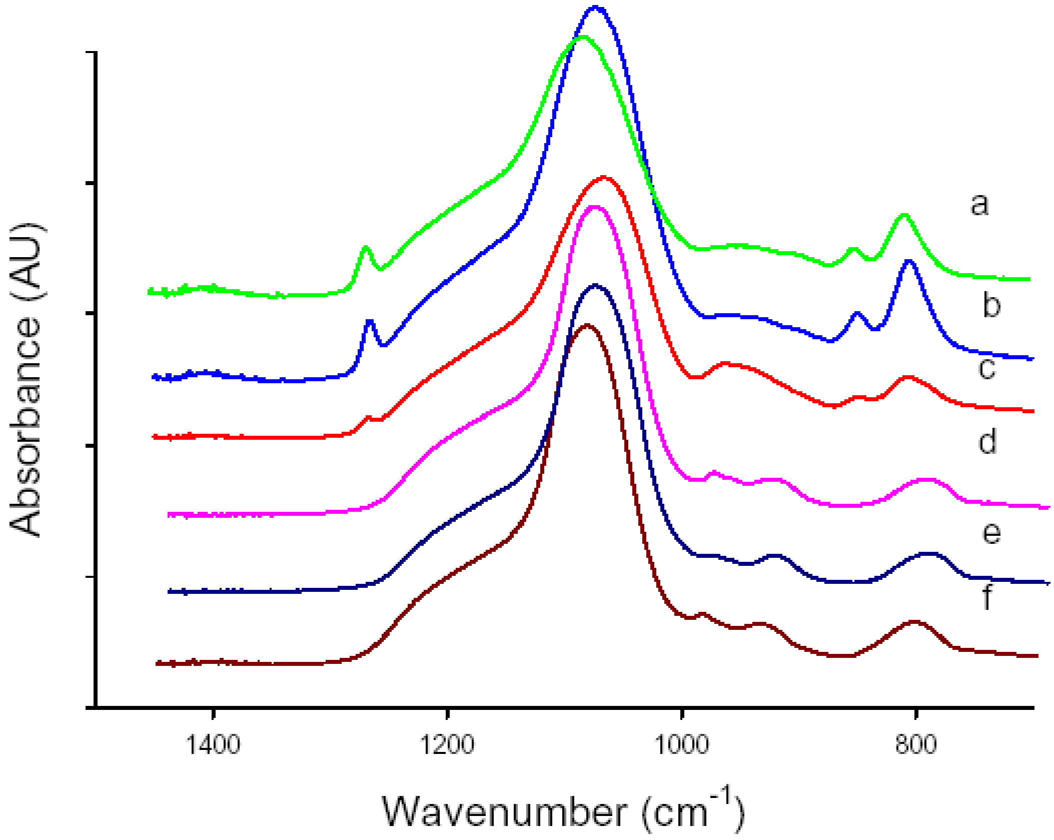

Fig. 24: FTIR spectra as a function of atomic percent of DMDES: (a) 45%, (b) 40%, (c) 35%, (d) 30%, (e) 25%, (f) 0%

5.3.3 DMDES Addition Time

Fig. 25 showed the FTIR spectra of the hybrid film as the function of DMDES (35%) pregeling time. The Si – C (1270 cm^{-1}) peak intensity changed with DMDES pregeling time although the molar ratio of DMDES was maintained at 35%. Fig. 26

shows the Si – C peak intensity changes with DMDES pregeling time by normalizing Si – C peak at 1270 cm^{-1} to silica network Si – O peak at about 1080 cm^{-1}. The curve had a very sharp increase between 0 to 2 hours, then a weaker increase between 2 to 6 hours, and a decrease after 6 hours.

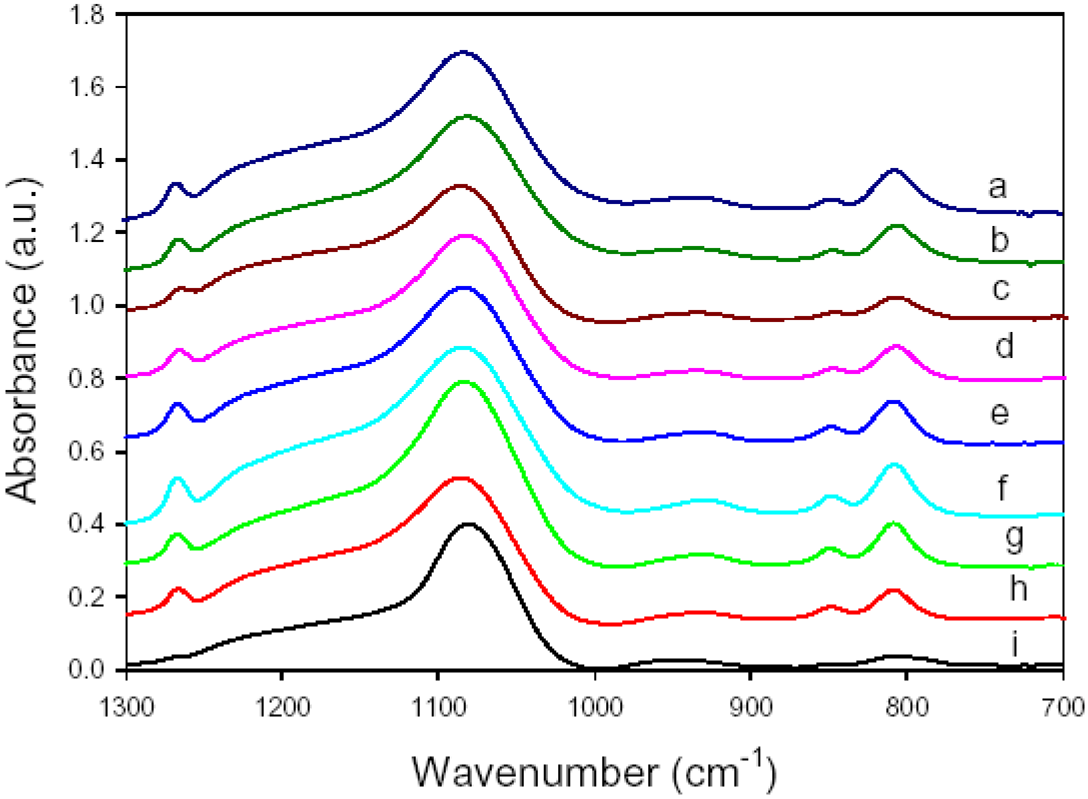

Fig. 25: FTIR spectra as function of DMDES pregeling time: (a) 13 hours, (b) 11 hours, (c) 10 hours, (d) 8 hours, (e) 6 hours, (f) 4 hours, (g) 1.5 hours, (h) 1 hour, (i) 0 hour

As we know, under acid catalyst DMDES hydrolyzes and develops linear and cyclic species [52, 53]. DMDES cyclic species cannot connect to the Si – O network. And at different time there are different fractions of cyclic and linear species. Monomer, dimer, trimer, etc would have different connectivity intrinsically and at different pregeling time due to dilution of cyclic species and steric hindrance. The only source for the Si –

C peak is from DMDES bonded to a TEFS network and / or its hydrolyzed monomers within the Si-O network. This curve suggested that at around 4-6 hours of DMDES pregelation the linear species had the highest total connectivity.

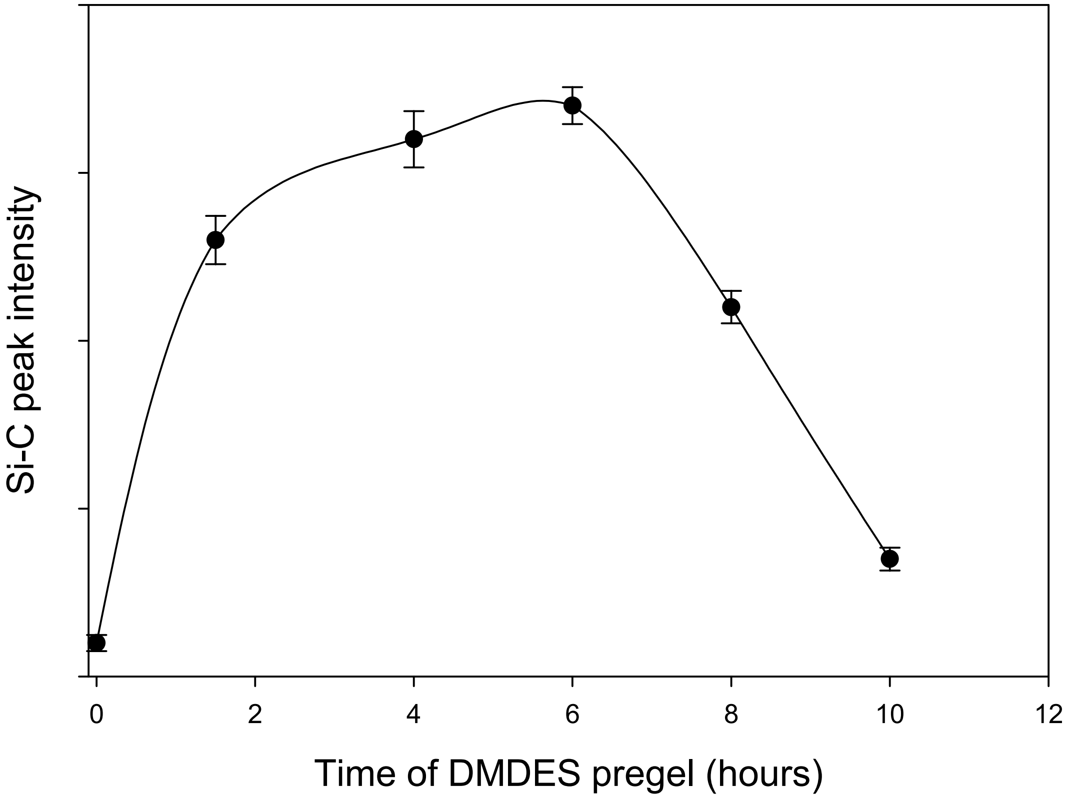

Fig. 26: Si - C peak intensity in FTIR spectra change with DMDES pregeling time

5.3.4 Nano-templating

Gas adsorption experiments were conducted to determine the effects of cyclic DMDES components on hybrid xerogel pore structures. Ringed-structures have no ability to connect to silica network because of lack of functionalizability. They can only act as spacers within gels. Results of average diameter change by BJH analysis [54] from N_2 isothermal desorption at relative pressure P / P_0 of 0.05 to 0.3 for hybrid xerogel (35% DMDES) are shown in Fig. 27.

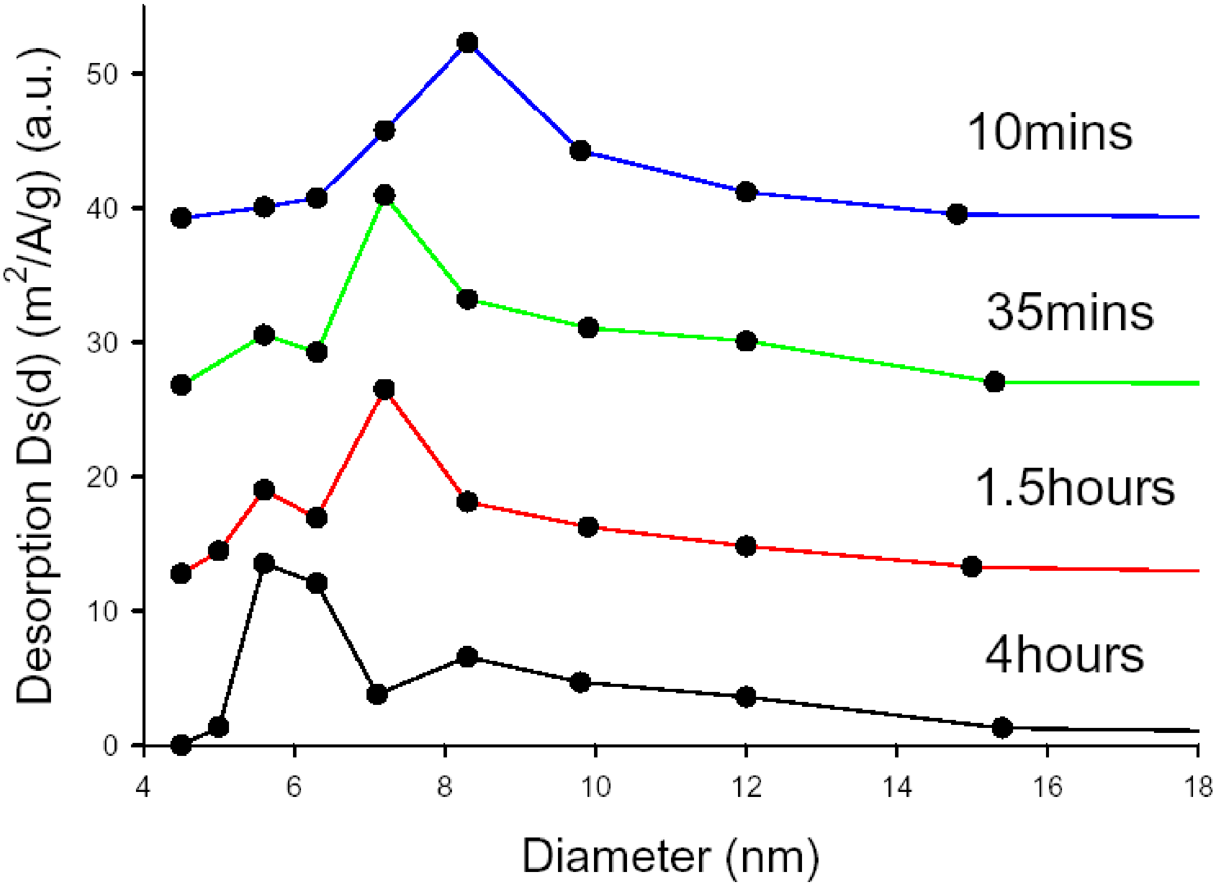

Fig. 27: Average pore diameter versus DMDES pregeling time

At short DMDES pregeling time (10 minutes), the hybrid xerogel showed a single diameter peak at about 8.5 nm. Later on, the system evolved into two peaks, the initial peak at 8.5 nm, and another peak at about 5.5 nm. As pregeling time increased, the peak at 5.5 nm gradually dominated.

From ^{29}Si liquid NMR data, we know that DMDES develops ring structures during hydrolysis and poly-condensation. The concentration of ring structures increases with time, as shown in Fig. 11. TEFS gelled intrinsically when DMDES pregeling time was short, and no ring structures were available. Some hydrolyzed DMDES monomers (D_0^1, D_0^2) or dimers ($D_1^0D_1^1$, $D_1^1D_1^1$) would be connected into the silica network, as manifested in FTIR spectra in Fig. 25 (i) and Fig. 26. As more ring species were available, they could act as nanotemplating agents for the silica network. Each individual C_4 has a diameter of about 1 nm [55]. Individual C_4 species or clusters of C_4 can prevent gelation in their intermediate vicinity and create voids. It is hoped that these voids would be on the scale of the C_4 diameter.

In bulk sample studies, we found that in hybrid xerogels normalized Si – C peak intensity increased with DMDES while Si – F peak decreased. Methyl groups in the xerogel dramatically decreased water adsorption peak, shown in Fig. 22. Due to different kinetics, the best time for DMDES introduction was 4 to 6 hours after DMDES pregeled under acidic catalyst. Introduced at that time, ring components from DMDES could function to produce nanometer pores.

To make hybrid film samples, different DMDES concentrations were used. Ring structures in DMDES are nonpolar. They repelled water from TEFS / EtOH / H_2O system, in which water was necessary for TEFS hydrolysis and condensation. This effect prevented introduction of large amounts of DMDES although different solvents (hexane, acetone, IPA, 1, 4-dioxane, etc.) were tried to alleviate the problem. The DMDES concentration was limited to 10% because higher DMDES concentration introduced phase separation. DMDES introduction time was set 4 to 6 hours after DMDES pregelation.

5.3.5 Viscosity

Hydrolysis and condensation of TEFS sols was affected when pregeled DMDES was introduced. The viscosity of hybrid system was measured and shown below:

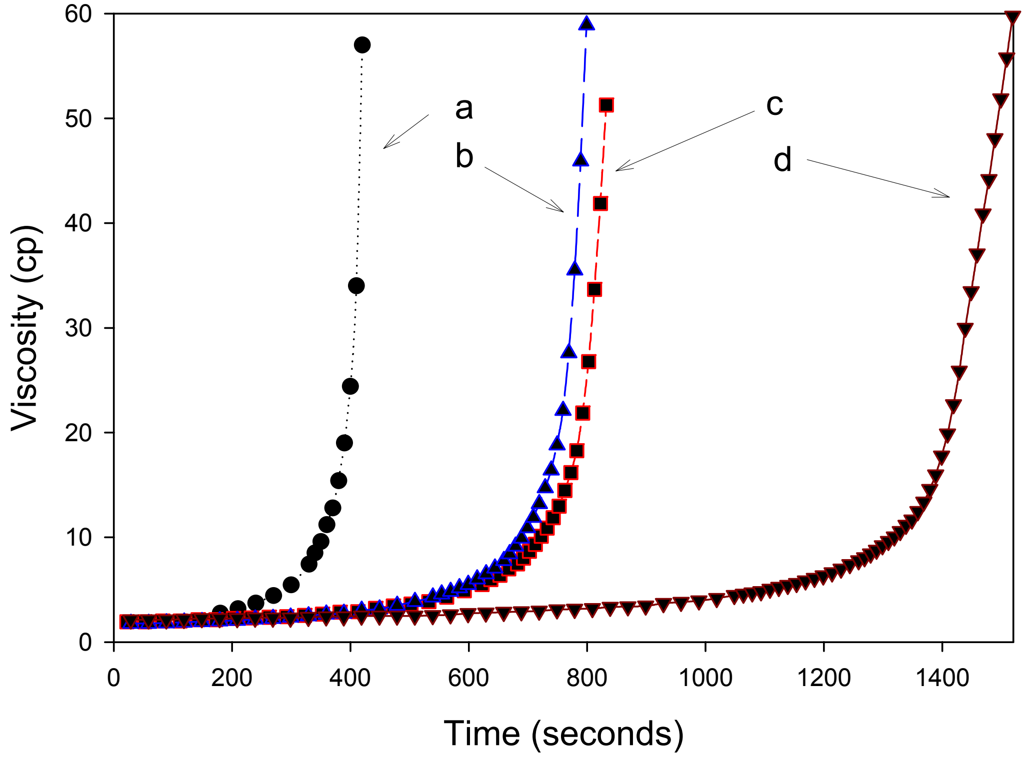

Fig. 28: Viscosity changes versus time, (a) 100 % TEFS + 15 EtOH + 4 H_2O, (b) 85% TEFS + (15% DMDES + 14.25 EtOH) + 4 H_2O, (c) (85% TEFS + 5% DMDES) + (10 % DMDES + 14.3 EtOH) + 4 H_2O, (d) (85 % TEFS + 15% DMDES) + 15 EtOH + 4 H_2O (1 cp = 10^{-3} Pa*sec, viscosity is within +/- 0.06 cp, time is within +/- 1 second)

To compare how DMDES introduction affected hybrid system gelation, functional groups (- OC_2H_5) from TEFS and DMDES were separately calculated and tabulated below:

Table 10: Calculated functional group concentrations of TEFS (a), three DMDES + TEFS hybrid systems (b, c, and d), and their gelation times (same systems a, b, c, and d as in Fig. 28)

system	a		b	
Functional group [OEt] concentration (N)	from TEFS	from DMDES	from TEFS	from DMDES
	2.599	0	2.599	0.095
Total concentration (N)	2.599		2.694	
gelation time (s)	406		773	
H_2O concentration (N)	3.465		3.413	
system	c		d	
Functional group [OEt] concentration (N)	from TEFS	from DMDES	from TEFS	from DMDES
	2.499	0.1	2.208	0.097
Total concentration (N)	2.599		2.305	
gelation time (s)	815		1441	
H_2O concentration (N)	3.401		3.475	

From Table 10 it was found that introducing DMDES into TEFS resulted in prolonged gel times although total functional group concentration (from both TEFS and DMDES) increased (comparing system (b) to (a)). Increasing total functional group concentration should decrease gelation time. This did not hold in these systems.

Fig. 29 showed viscosity change with relative time progress. Although different hybrid systems took different gelation times, their viscosity change as a function of relative time did not vary much. Mah et al. believed that all the hybrid systems had a similar gelation mechanism [56]. In DMDES and TEOS hybrid systems, Glaser et al. discovered that DMDES had 100% degree of reaction using ^{29}Si solid state NMR [1]. Babonneau et al. got the same result (e.g. DMDES was fully condensed within TEOS by

^{29}Si MAS NMR analysis) [57]. Brus et al. found that DMDES molecular segments in silica network were delocalized by ^{1}H MAS NMR [58].

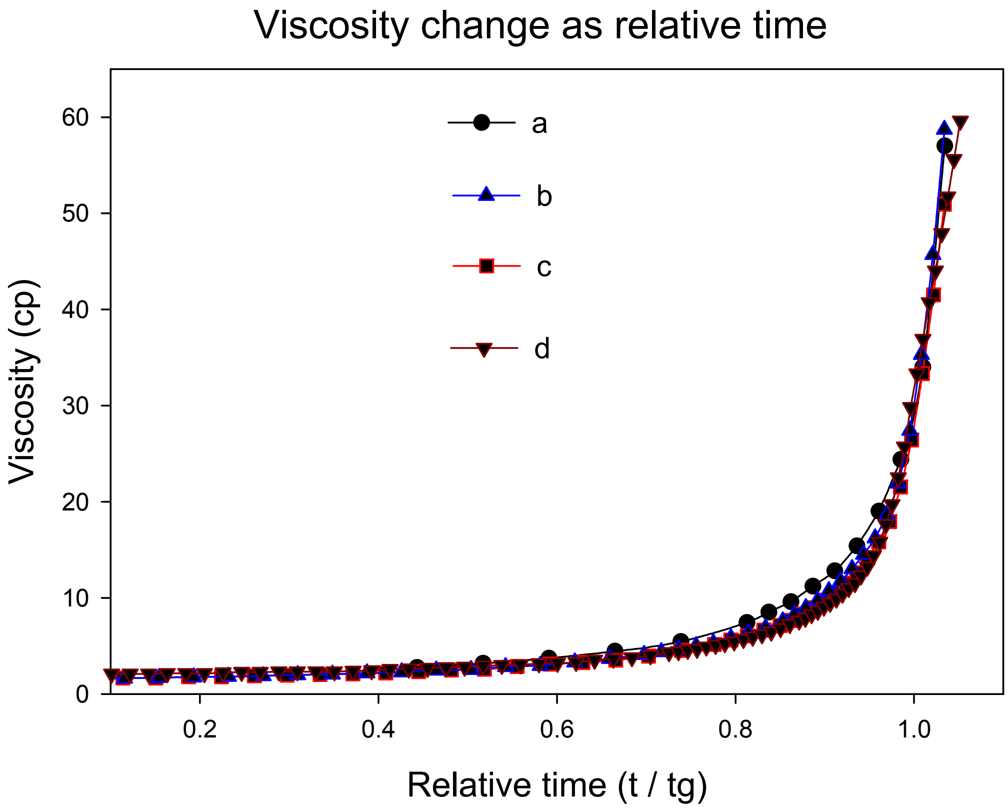

Fig. 29: Viscosity change as a function of relative time t / tg (tg taken from viscosity reached 30 cp) of the same systems a, b, c, and d, as in Fig. 28 (1 cp = 10^{-3} Pa*sec, viscosity is within +/- 0.06 cp, time is within +/- 1 second)

In these four systems (a, b, c, d), all experimental conditions (water concentration, temperature, catalyst type and concentration, and DMDES pregeled time) were almost the same except for functional group concentrations. Gelation time should be the result of functional group concentration differences in different systems. Comparing systems a and b, DMDES addition did not lead to decreased gel time although total functional group concentrations increased. We propose that the introduction of DMDES would delay or “poison” TEFS gelation.

Fig. 30 shows the gelation time increased as the ratio of DMDES to TEFS increased. It is possible that when fluorine from TEFS and methyl groups from DMDES combined, they neutralize each other and "stabilize" the TEFS plus DMDES units. Campostrini et al. [39] shared the same idea.

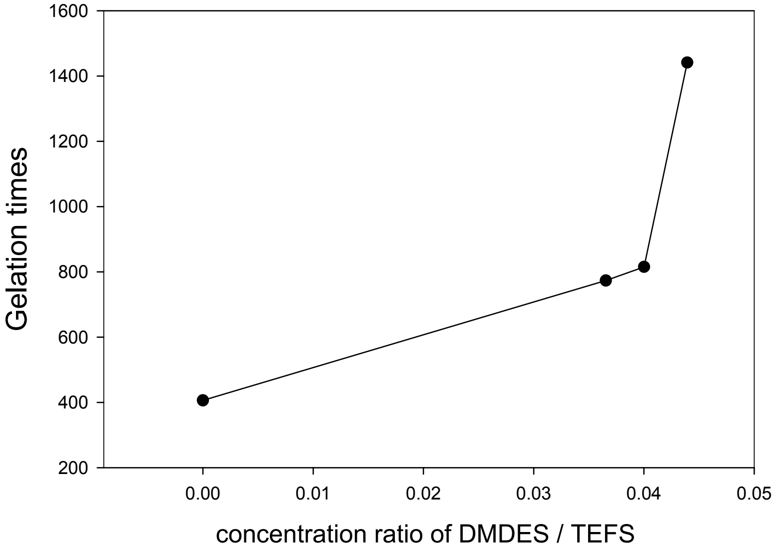

Fig 30: Gelation time of DMDES + TEFS hybrid system increase as DMDES relative concentration increase (time is within +/- 1 second)

5.3.6 Model for Hybrid System

Based on above analysis, a model was proposed for the DMDES + TEFS hybrid system:

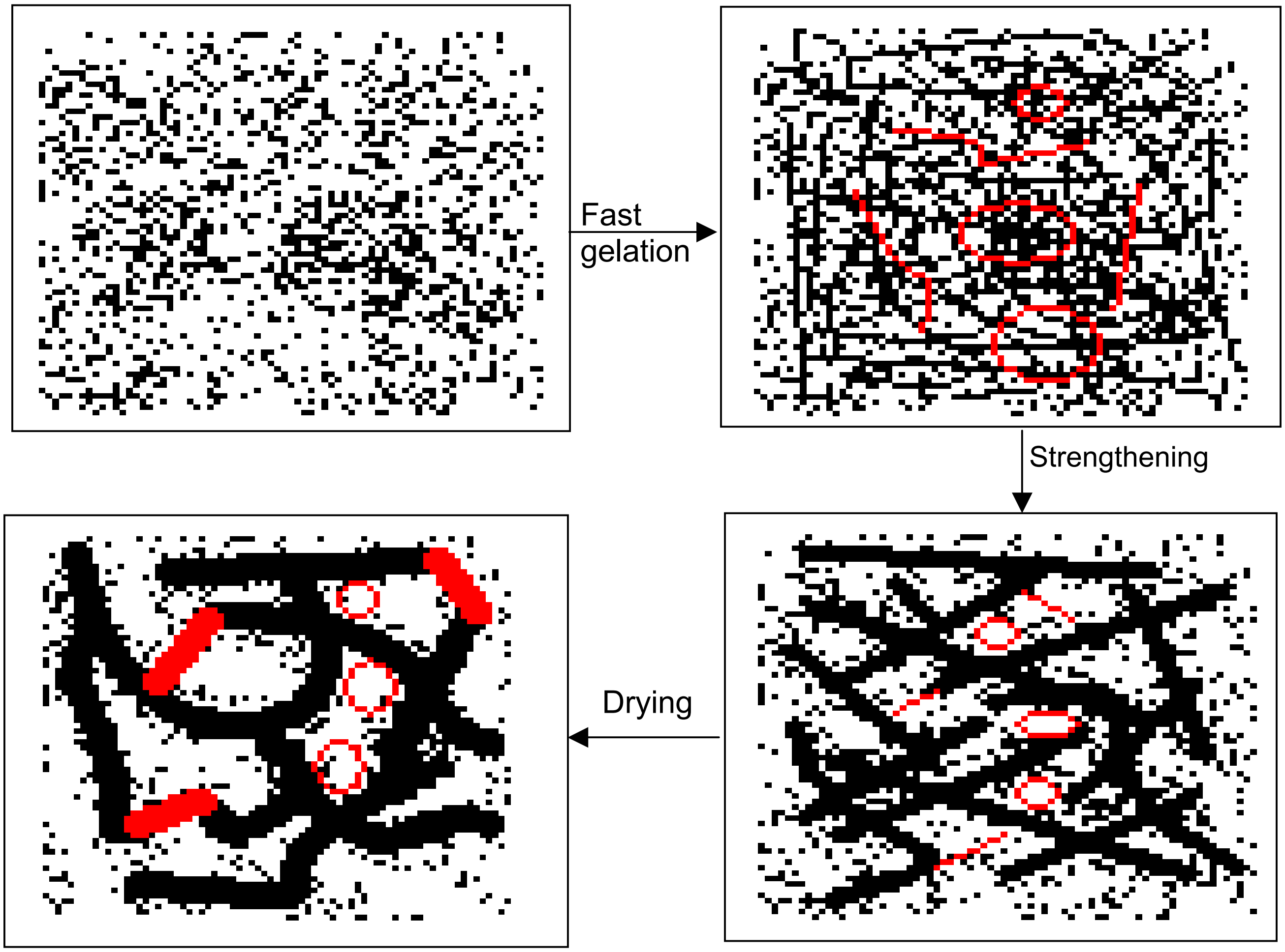

Fig. 31: Proposed model for hybrid system gelation (dots as monomers, lines as linear clusters, and circles as ringed-species)

Due to neck-thickened linkages, TEFS xerogels have high strength. Intrinsic F-bearing and porous microstructure created films with low dielectric constants. After DMDES introduction, the hybrid system would inherit some / or all those benefits from the TEFS-derived silica matrix. Ring structures from DMDES acted a “nanotemplating agent" creating voids during hybrid gelation. Linear components connect to partially hydrolyzed TEFS species when TEFS was introduced into pregeled DMDES solutions. Because of the conflicting effects of methyl groups and fluorine, the intermediate products somehow were stabilized. TEFS concentration was dominant, so that hybrid system has a delayed gel time. Connected linear species from DMDES would give the final product hydrophobicity.

5.4 Characterizations

5.4.1 Hydrophobicity

Hybrid film hydrophobicity increased as a function of DMDES concentration in the hybrid film increased, as shown in Fig. 32. This is because more linear species (i.e. methyl groups) were connected to the silica network.

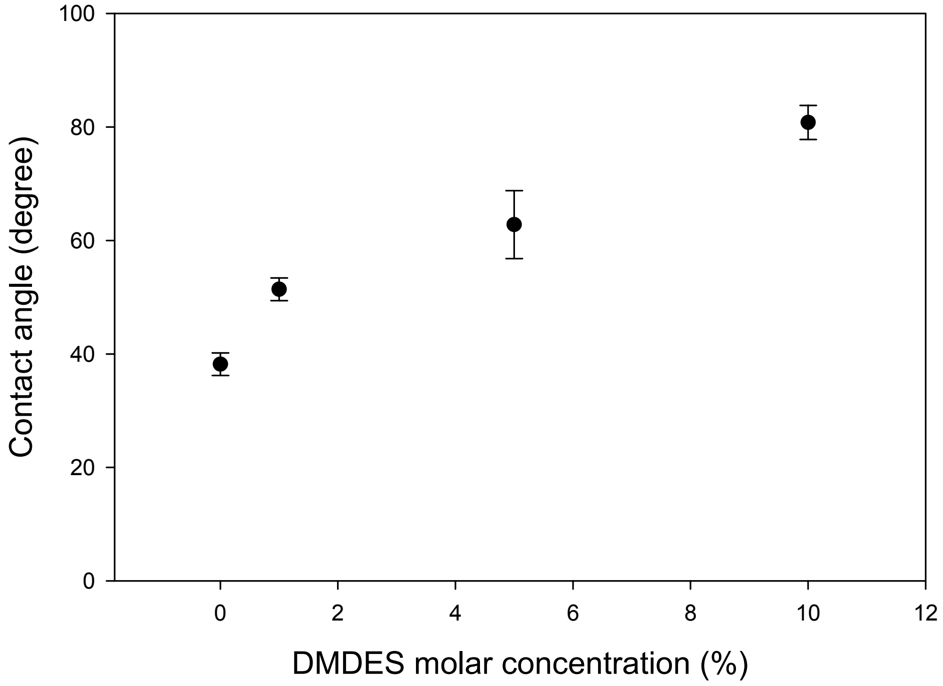

Fig. 32: Film hydrophobicity increase as DMDES concentration increase

As more DMDES is introduced, more linear species are connected into the silica matrix, and methyl groups would result into the network. Methyl groups can decrease a film's concentration of OH groups and water, so hydrophobicity should increase as a function of DMDES concentration.

We lack methods to characterize film pore size distribution; therefore, we assume DMDES affects films as it does in bulk samples.

5.4.2 Thermal Stability

Thermal stability property is very important for materials integration in IC processing. We did thermogravimetric analysis (TGA) and compared results with FTIR (before and after TGA analysis), contact angle measurements, and DSIMS results.

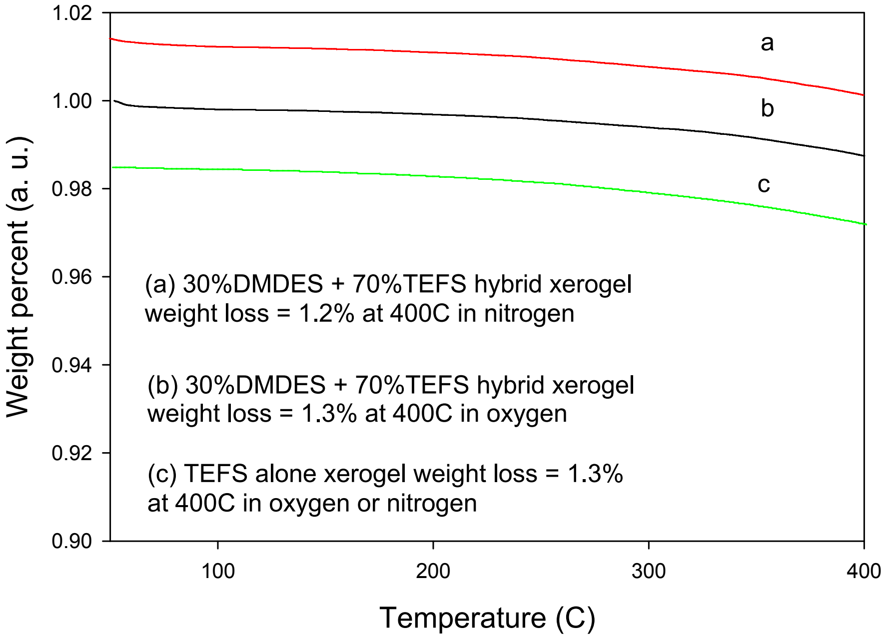

Fig 33: Weight loss of TEFS and 30% DMDES + TEFS hybrid xerogels with heated temperature and ambient environment. Error is within ± 3.0 % from calibration.

Different systems (TEFS only and 30% DMDES + TEFS) and different ambient environments (under pure oxygen and nitrogen) shared similar TGA curves. Campostrini et al. [39] analyzed TEFS xerogels made under inert or atmospheric conditions with thermogravimetric-mass spectroscopy (TG – MS) combination and found that before 400°C, the total weight loss was 1.2%, very similar to our results. TG – MS showed that water outgassed between room temperature and 250°C, (i.e., adsorbed or entrapped), and between 250°C to 400°C EtOH outgassed as a solvent and from condensation reactions:

$$\equiv \mathrm{Si} - \mathrm{OEt} + \mathrm{HO} - \mathrm{Si} \equiv \longrightarrow \equiv \mathrm{Si} - \mathrm{O} - \mathrm{Si} \equiv + \mathrm{EtOH}.$$

Near 400°C, they detected SiF_4. In a DMDES + TEOS system, Mah et al. [56] believed that before 150°C weight loss corresponded to desorption of physically adsorbed water or residual solvents, between 150 to 550°C related to removal of organics accompanied by polymerization and structural relaxation. Due to methyl-induced hydrophobicity, water-related weight loss before 150°C was negligible. Babonneau et al. found the total weight loss before 400°C was around 2% corresponding to completion of condensation reactions [57]. In PECVD deposited carbon-doped SiO_2:F films, Lubguban et al. discovered the continuous loss of Si – F bonds between 300°C to 400°C by integrating FTIR spectra using Beer's law, and continuous loss of $Si - CH_3$ bonds by inspecting the $Si - CH_3$ peak intensities, but did not explain the details of these reactions [42].

To ascertain the lost components, a comparison of FTIR spectra of 30% DMDES + TEFS samples of as-made after TGA analysis in oxygen and in nitrogen is shown in Fig. 34.

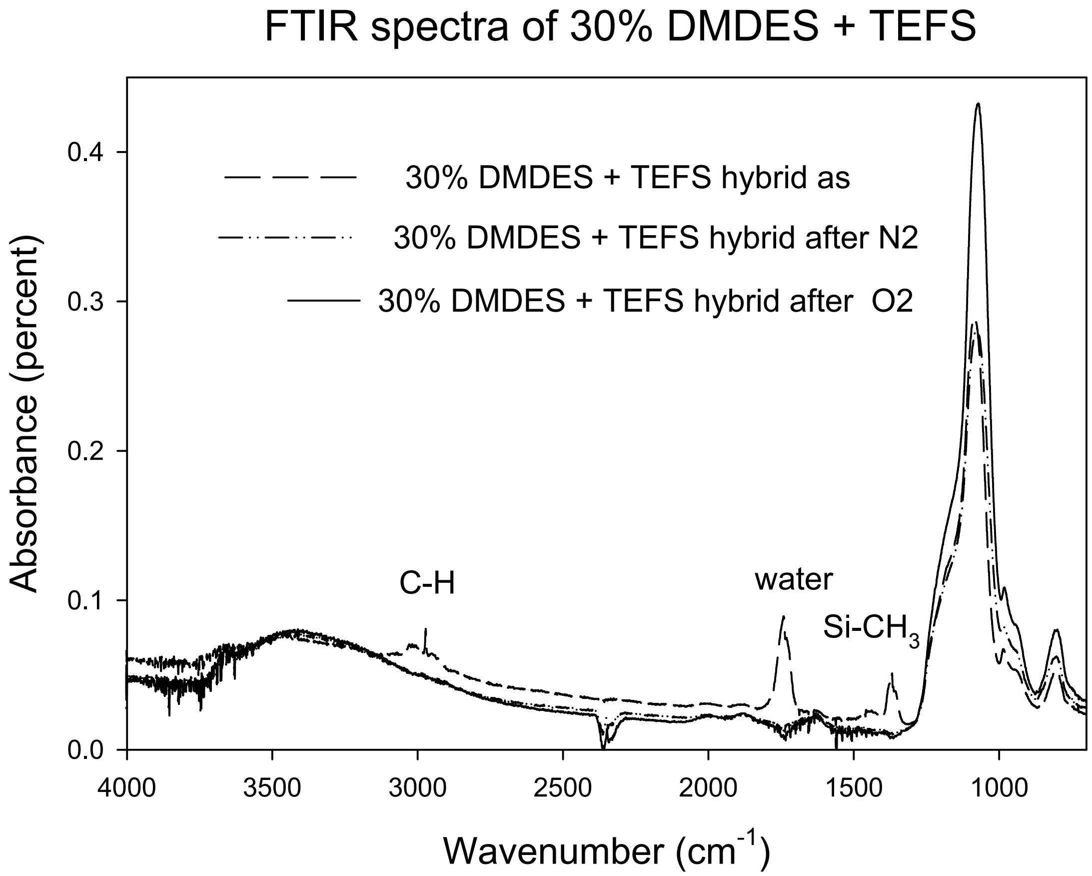

Fig. 34: FTIR spectra of 30% DMDES + TEFS hybrid xerogel (1) as, (2) heated in N_2 at 400°C for 2 hours, (3) heated in O_2 at 400°C for 2 hours

From the FTIR spectra, it was found that after annealing in both environments, free water (peaked at about 1636 cm^{-1}) was lost and Si – CH_3 bonds decreased dramatically (Si – CH_3 peaked at 1265 cm^{-1} and C – H peaked at 3048 to 2906 cm^{-1}). Fluorine showed no significant changes (Si – F peaked at about 940 cm^{-1}). Except those common changes, a Si – O – Si peak intensity increase was obvious only after oxygen annealing. All three FTIR spectra were under common scale, the Si – O – Si peak intensity increase might describe higher matrix structure enhancement.

Methyl group loss was further confirmed by contact angle measurements, shown in Fig. 35. All samples were heated under atmosphere for one hour at temperatures from 100°C to 400°C.

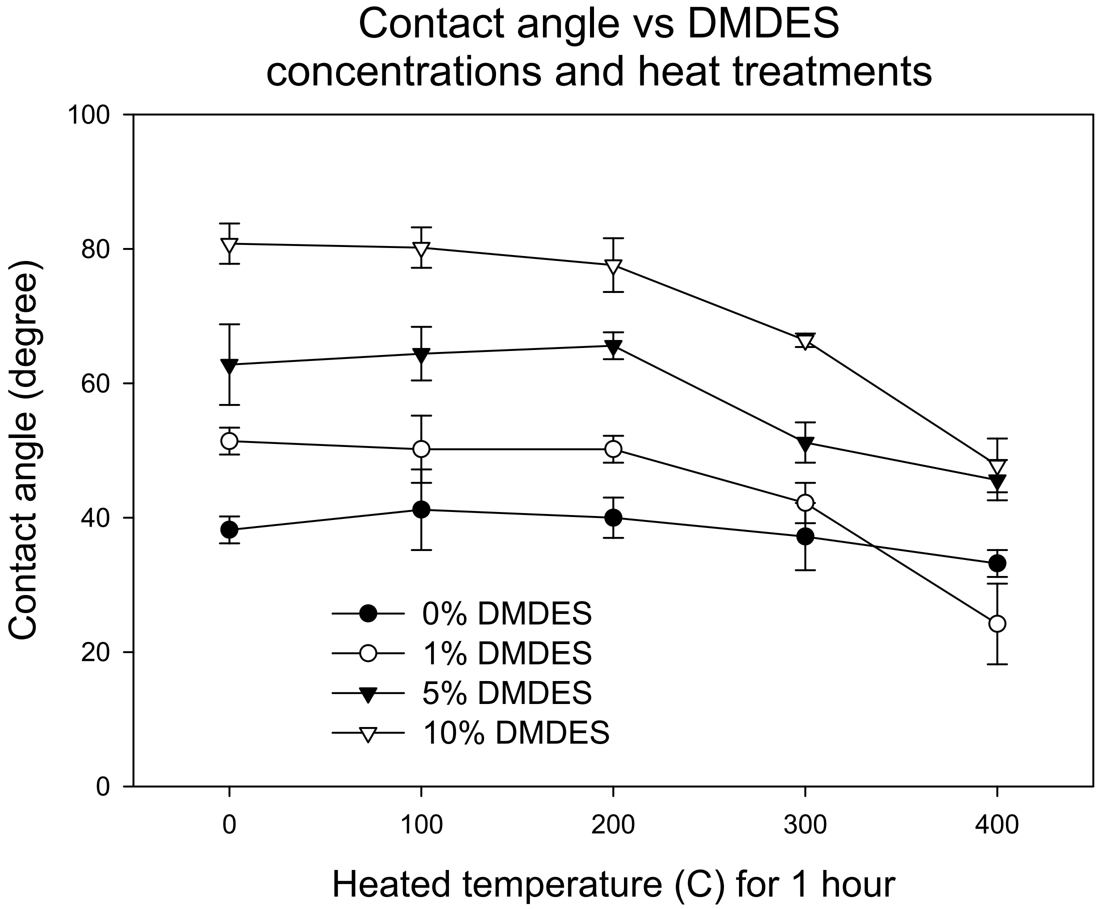

Fig. 35 Contact angle change with thermal treatments and introduced DMDES concentrations.

As DMDES concentration increased, the contact angle increased because more methyl groups were connected to the Si – O – Si network. When samples were heated up to 200°C contact angles did not change. At temperatures above 200°C, hybrid films showed a decrease of contact angle, but TEFS did not. We attributed the contact angle decrease between 200°C to 400°C to the loss of methyl groups in hybrid films.

Two films (TEFS-only and 10% DMDES + TEFS) were analyzed further by DSIMS to trace elemental concentration changes upon thermal treatments. Their results were summed in Fig. 36, 37, 38 and Table 11. In Fig. 36, all elements showed almost uniform distribution throughout the films. The concentration decrease near the surface was attributed to experimental artifacts [59], and the concentration increase of some elements at the film-substrate interface was due to sample cleaning residuals. Elemental concentration calculations were averaged between 1000 Å to 2000 Å regions.

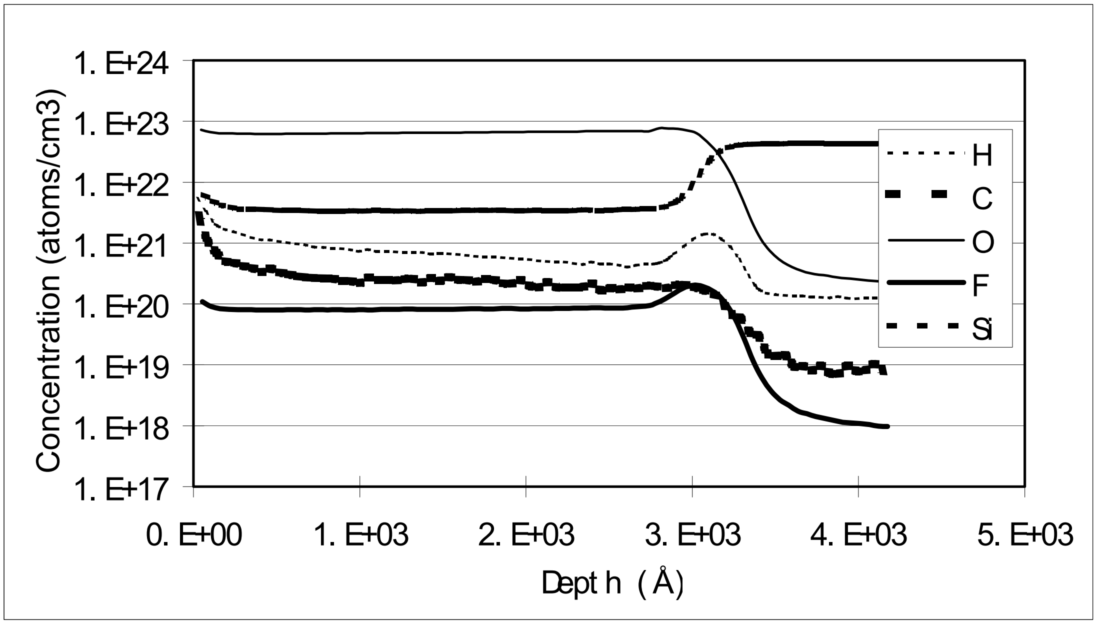

Fig. 36: DSIMS result for 10% DMDES + TEFS films.

Table 11: Summary of DSIMS elemental analysis of TEFS-only and 10% DMDES + TEFS films

		O	Si	F	C	H
TEFS only	0°C	6.52E+22	3.40E+21	8.22E+19	2.48E+20	6.58E+20
	(σ_{stdev})	9.08E+20	3.65E+19	1.05E+18	1.73E+19	6.66E+19
	200°C	6.39E+22	4.01E+21	9.85E+19	1.07E+21	1.32E+21
	(σ_{stdev})	1.39E+21	7.87E+19	6.29E+17	1.18E+20	1.78E+20
	400°C	6.31E+22	3.36E+21	1.83E+19	2.90E+20	7.29E+20
	(σ_{stdev})	8.75E+20	4.08E+19	2.94E+17	1.68E+19	5.63E+19
10% DMDES + TEFS	0°C	6.52E+22	3.55E+21	1.38E+20	1.82E+20	7.52E+20
	(σ_{stdev})	1.27E+21	5.07E+19	2.32E+18	1.95E+19	8.84E+19
	200°C	6.86E+22	3.84E+21	1.38E+20	3.35E+20	8.39E+20
	(σ_{stdev})	6.73E+20	5.74E+19	1.94E+18	4.04E+19	1.07E+20
	400°C	6.35E+22	3.48E+21	1.05E+20	2.12E+20	7.90E+20
	(σ_{stdev})	5.38E+20	9.95E+19	2.16E+18	1.22E+19	4.18E+19

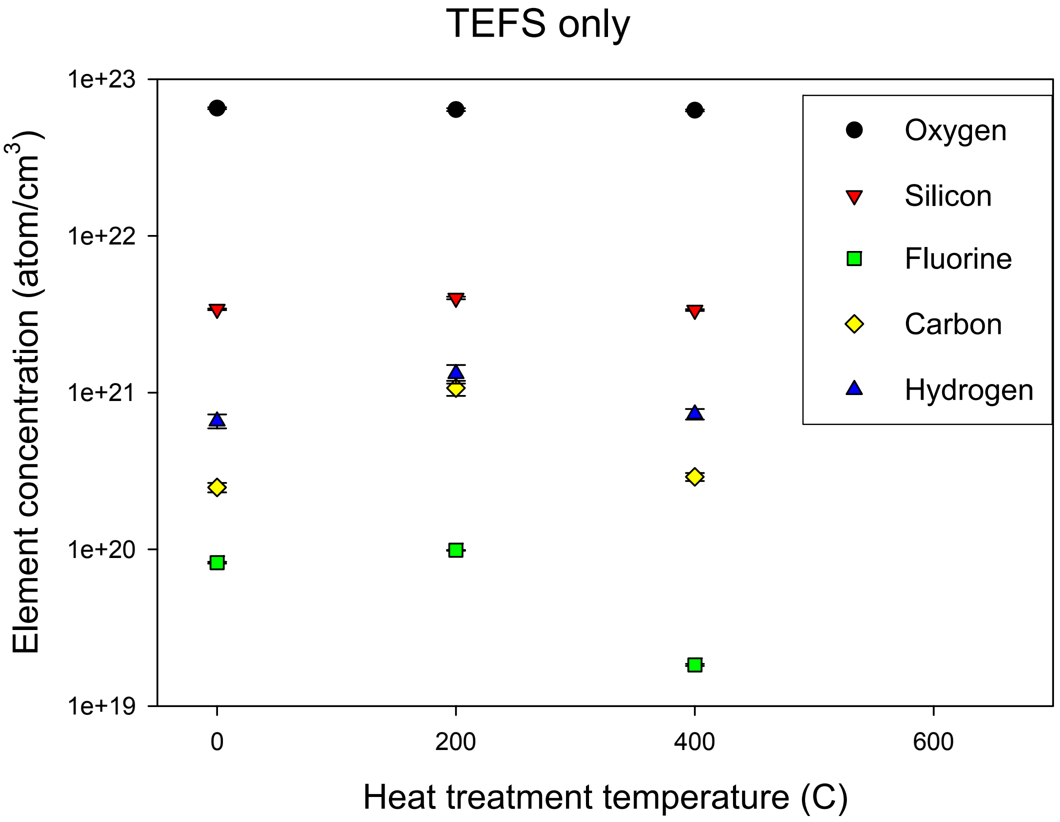

Fig. 37: DSIMS elemental analysis for TEFS-only film

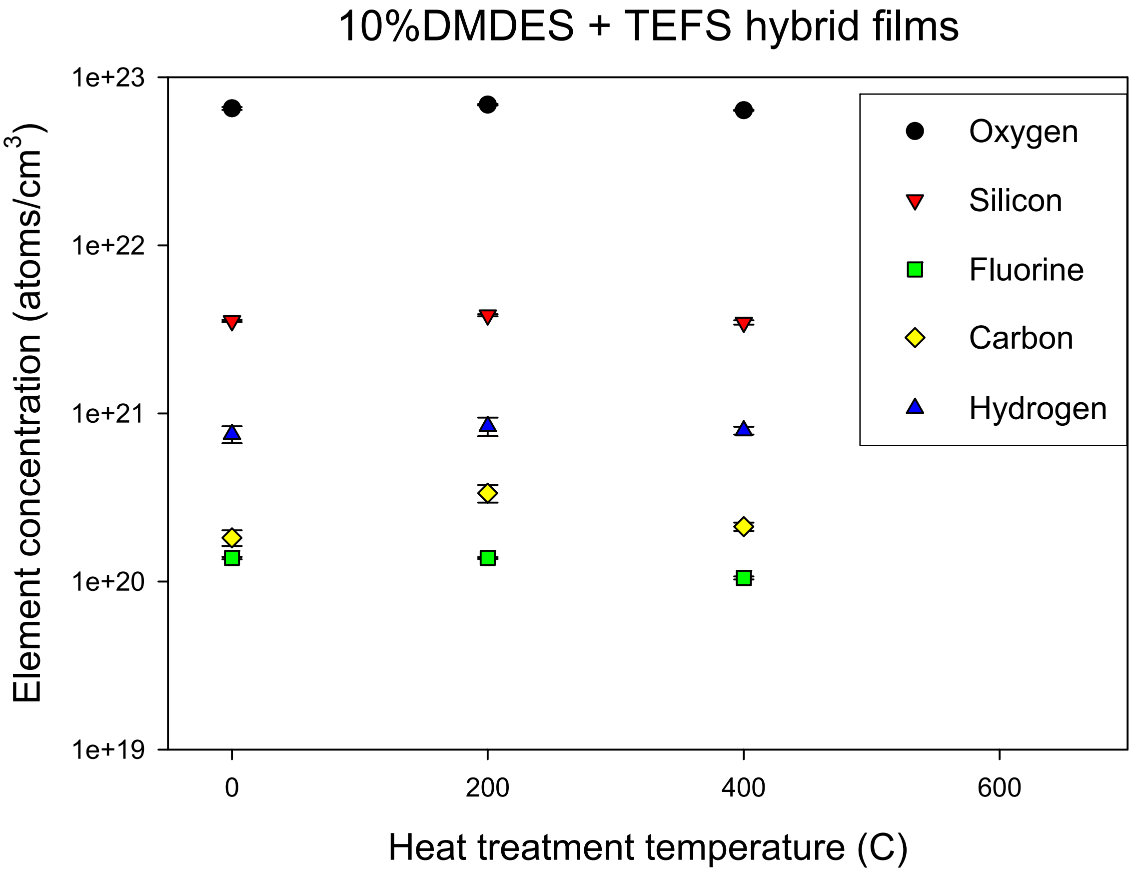

Fig. 38: DSIMS elemental analysis for 10% DMDES + TEFS film

Table 11, Fig. 37 and Fig. 38 showed elemental concentration changes in TEFS and 10% DMDES + TEFS films after different heat treatments. In both samples and after different temperature treatments, oxygen and silicon concentrations were constant, suggesting the main structure did not change significantly. Fluorine concentration in TEFS decreased above 200°C, but in 10 % DMDES + TEFS film did not show such a trend, perhaps due to methyl group stabilization of the fluorine. At different thermal treatments (room temperature, 200°C, and 400°C for one hour respectively), carbon elemental concentrations in TEFS-only and 10% DMDES + TEFS hybrid films did not change significantly. Since no methyl-bearing DMDES was introduced in TEFS-only sample, carbon concentrations in DSIMS analysis may be due to residual ethoxy groups (– OC_2H_5).

Combining TGA, FTIR, contact angle measurements, and DSIMS results, we can conclude:

Weight loss for both TEFS-only and DMDES + TEFS hybrid samples between room temperature to 400°C could be separated into two parts:

- room temperature to 200°C, mainly water loss
- 200°C to 400°C, mainly EtOH loss resulting from further condensation of residual ethoxy groups and nearby OH groups

In both oxygen and nitrogen annealing, samples lost most of their methyl groups, which made samples less hydrophobic. In oxygen annealing, structural change (i.e., further condensation) may be responsible for the Si – O – Si peak intensity increase. Fluorine concentration showed a decrease in the TEFS film but did not in 10% DMDES + TEFS hybrid samples, which may be due to methyl group's stabilization of the fluorine

5.4.3 Dielectric Constant Calculations

Dielectric constant calculations were based on impedance measurements using plate capacitance model.

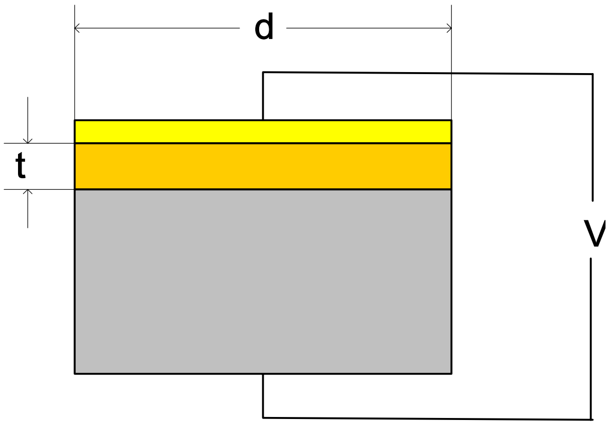

$$C = \frac{Q}{V} = \frac{\varepsilon_0 * k_r * 1/4 * \pi * d^2}{t}$$

Fig. 39: Parallel capacitance model and its equation

These measurements were critical to dielectric constant: t, film thickness, measured by ellipsometry, C, capacitance, measured by impedance measurement, and d, electrode diameter, measured by SEM.

(a) film thickness measured by ellipsometry

After collecting experimental data, film properties under investigation were obtained by model-fitting process. Based on physical structure, a layered model with some optical constants as fitting parameters was built. Film properties (i.e., thickness, refractive index) can be obtained by model fitting. A standard SiO_2 sample (TEOS CVD SiO_2 1000Å thick) was used as reference:

Built model:

1 SiO_2	1000 Å
0 Si	0.775 mm

Fitted model

1 SiO_2	1000.7 Å
0 Si	0.775 mm

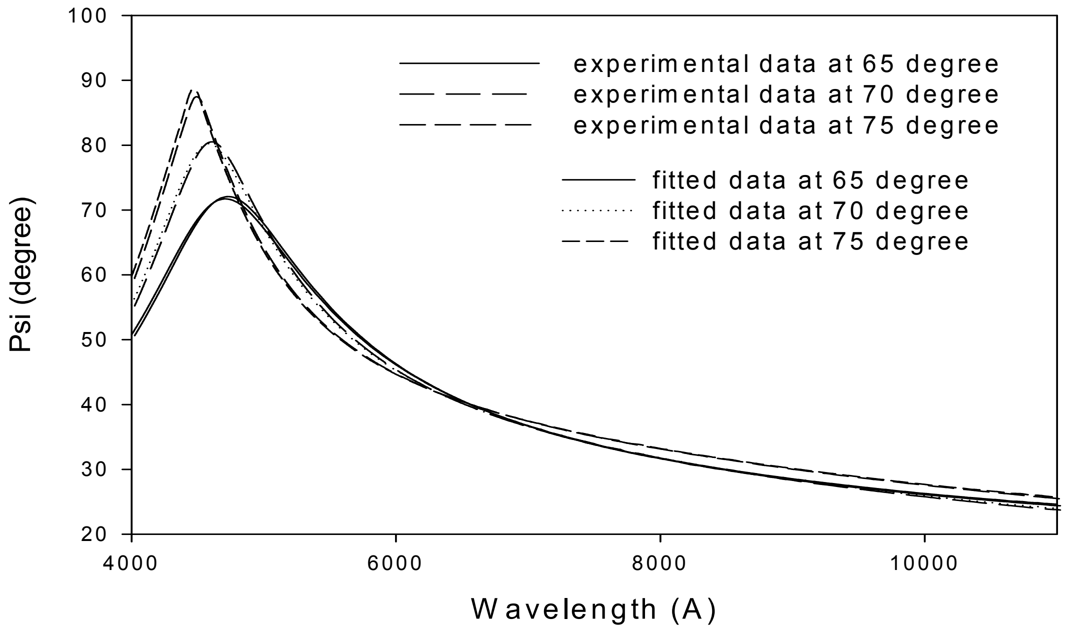

Fig. 40: Experimental data from ellipsometer and generated data from built model at 65, 70, and 75°

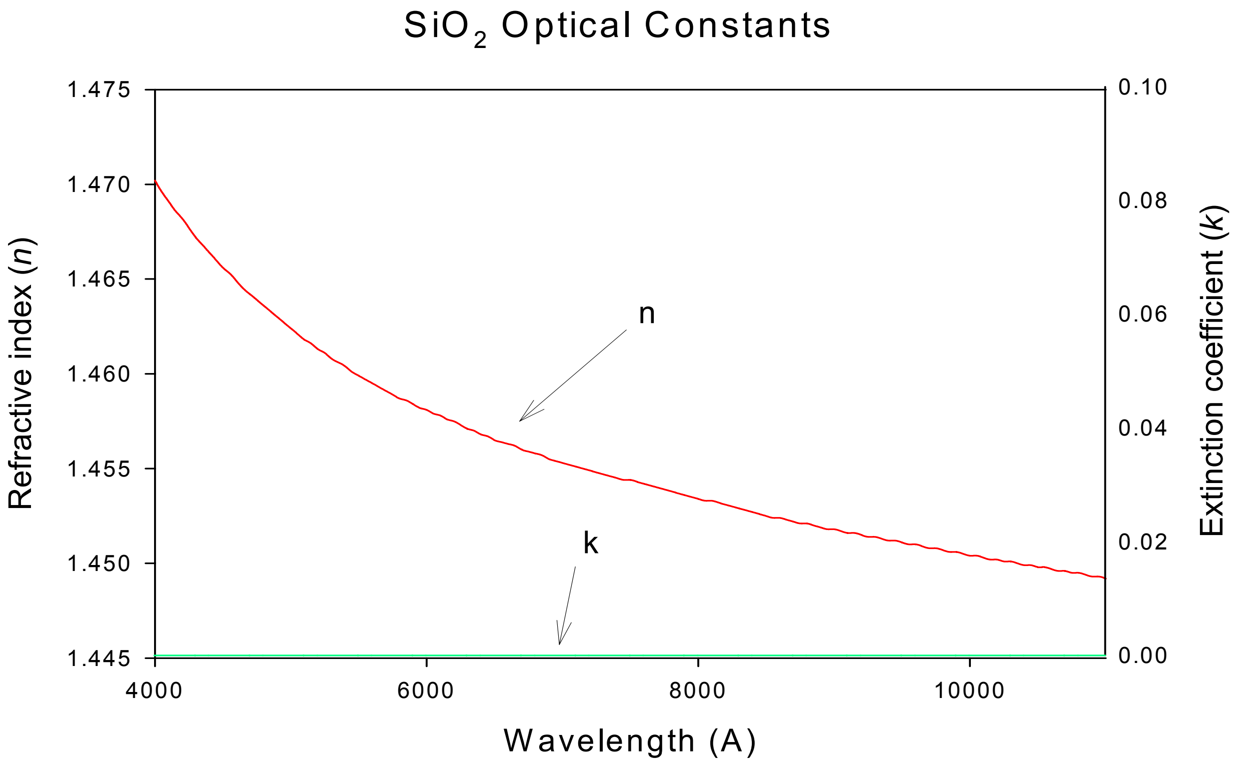

Fig. 41: SiO_2 film optical constants obtained by ellipsometry

SiO_2 thickness is 1000 Å based on ellipsometry measurements following deposition (i.e.,1000.7Å). Generated data and experimental data fitted quite well (MSE = 5.685, more details later). Refractive index changes with incident light wave length showed a decay, which was general for Cauchy non-absorpting materials (k = 0).

Xerogel films are not as simple as SiO_2 due to their intrinsic porous nature. To improve fitting, several methods were played, including adding a surface roughness layer (effective medium approximation, EMA), film-substrate intermixing, and film structure grading. One example was shown:

Built model:

EMA	100 A
Cauchy	2000 A
Si	0.775 mm

Fitted model:

srough	26 A
Cauchy	2113.5 A
Si	0.775 mm

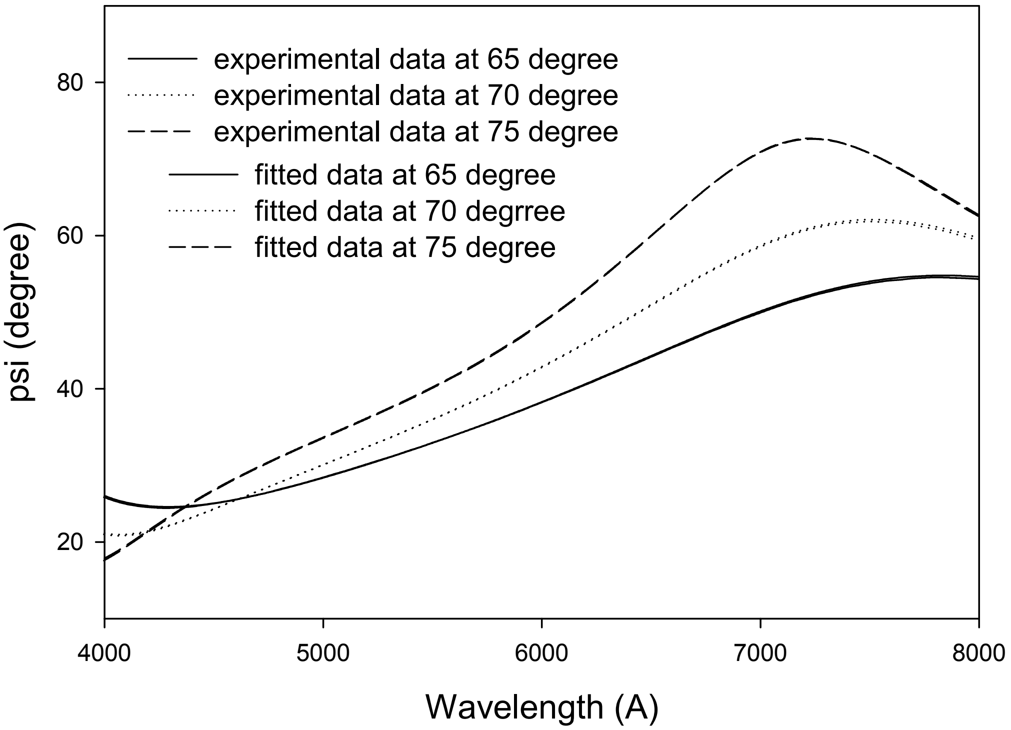

Fig. 42: Experimental data from ellipsometry and generated data from modeling for a hybrid film

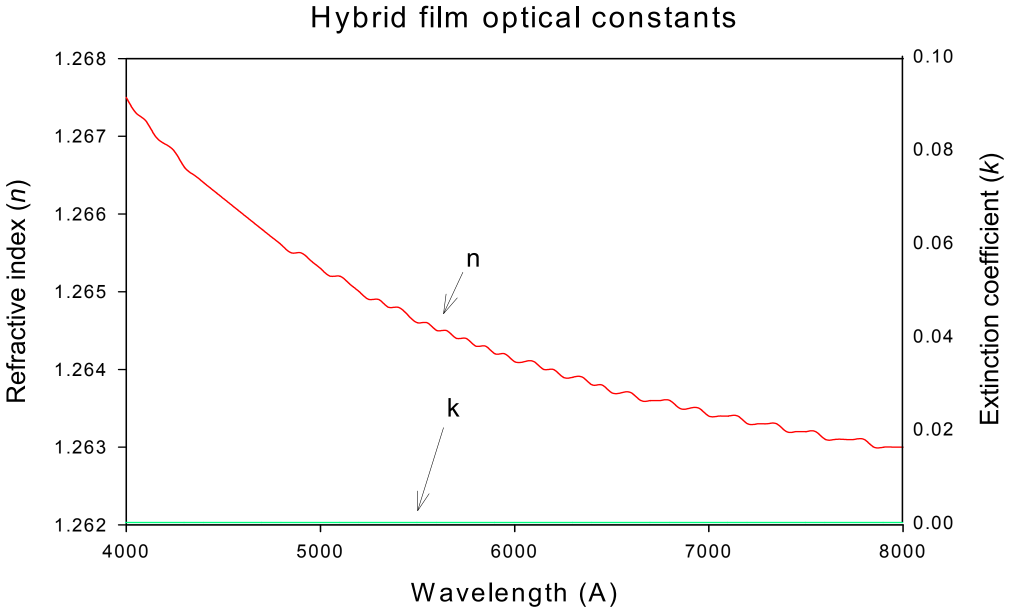

Fig. 43: Optical constants for a hybrid film from ellipsometry

To evaluate the model fitting, a Levenberg-Marquardt algorithm was used to fit the model parameters by minimizing the following equation:

$$MSE = \frac{1}{2N-M}\sum_{i=1}^{N}\left[\left(\frac{\Psi_i^{\mathrm{mod}}-\Psi_i^{\mathrm{exp}}}{\sigma_{\Psi,i}^{\mathrm{exp}}}\right)^2+\left(\frac{\Delta_i^{\mathrm{mod}}-\Delta_i^{\mathrm{exp}}}{\sigma_{\Delta,i}^{\mathrm{exp}}}\right)^2\right]=\frac{1}{2N-M}\chi^2$$

MSE is mean square error; N is the number of measured Ψ and Δ pairs; M is the number of fitting parameters; Ψ^{mod}, Δ^{mod} are model generated values; Ψ^{exp}, Δ^{exp} are experimental data; and σ is the standard deviation. A "good" fit should produce MSE approaching one [60].

For some sol-gel films, MSE can go as low as 1. A comparison of thickness from XSEM and ellipsometry would further evaluate the model fitting.

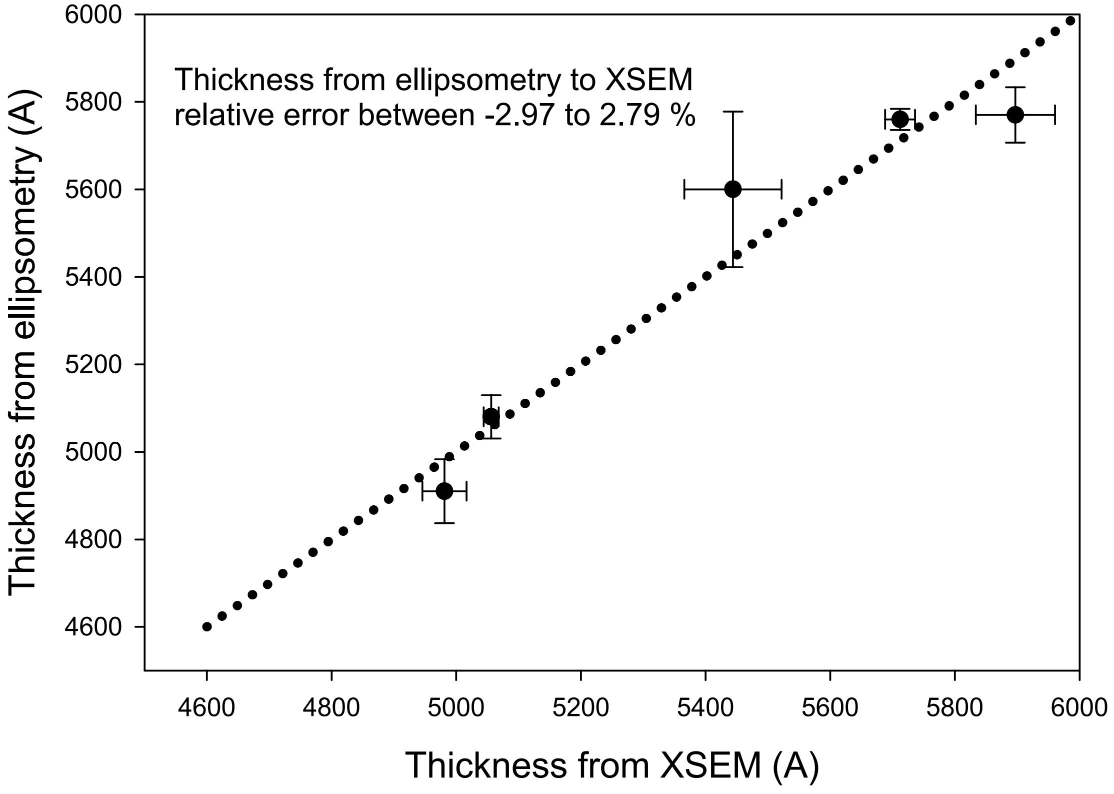

Fig. 44: Comparison of thickness from XSEM and ellipsometry

Based on the analysis and comparison, our thickness measurements correlate to 1 ± 3 %.

(b) Capacitance from impedance measurements

All TEFS-only and DMDES + TEFS samples were measured with an Agilent Impedance Analyzer 4294A by sweeping DC bias of different regions at 1 MHz oscillation frequency. A 1000Å TEOS CVD SiO_2 film was used as reference.

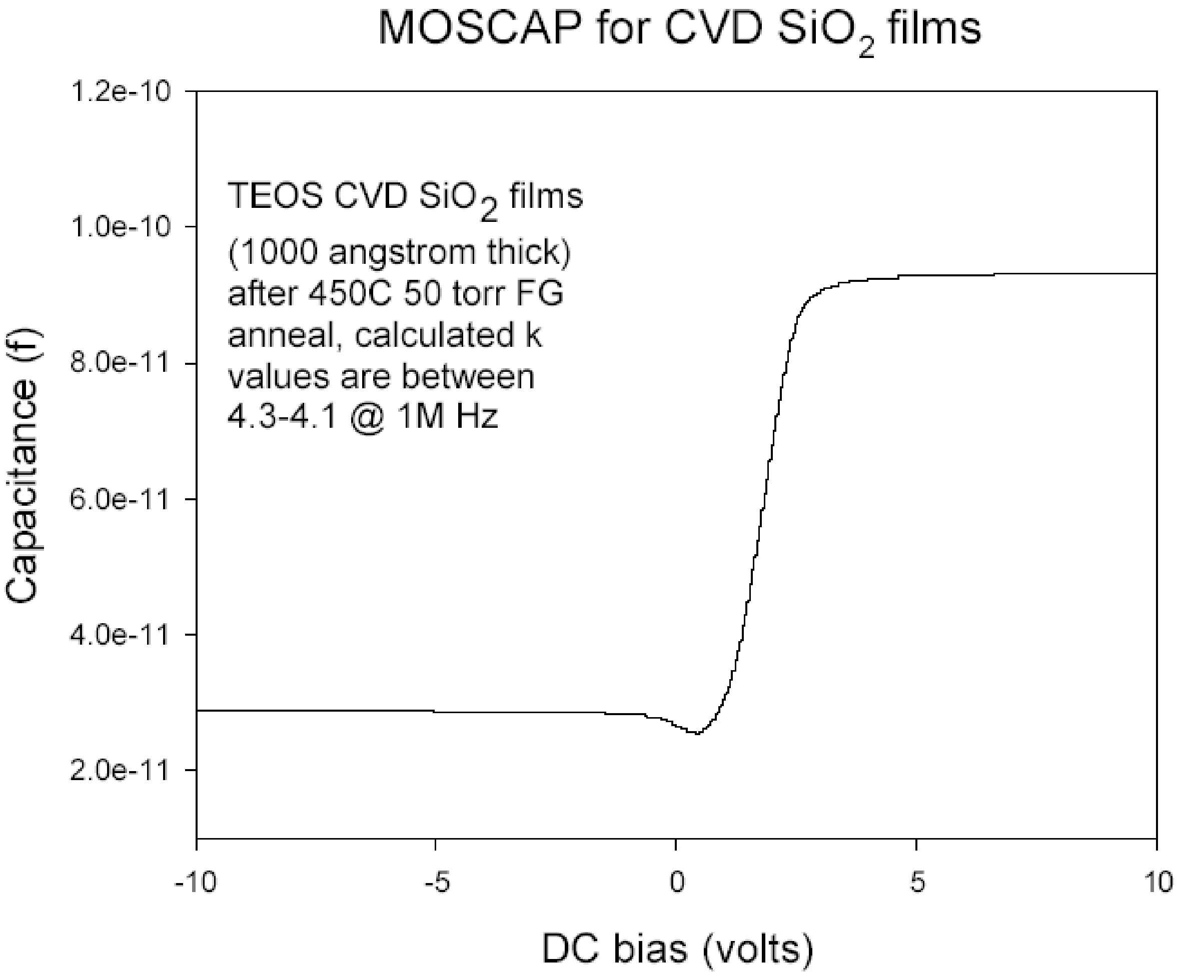

Fig. 45: CV curve for TEOS CVD SiO_2 sample

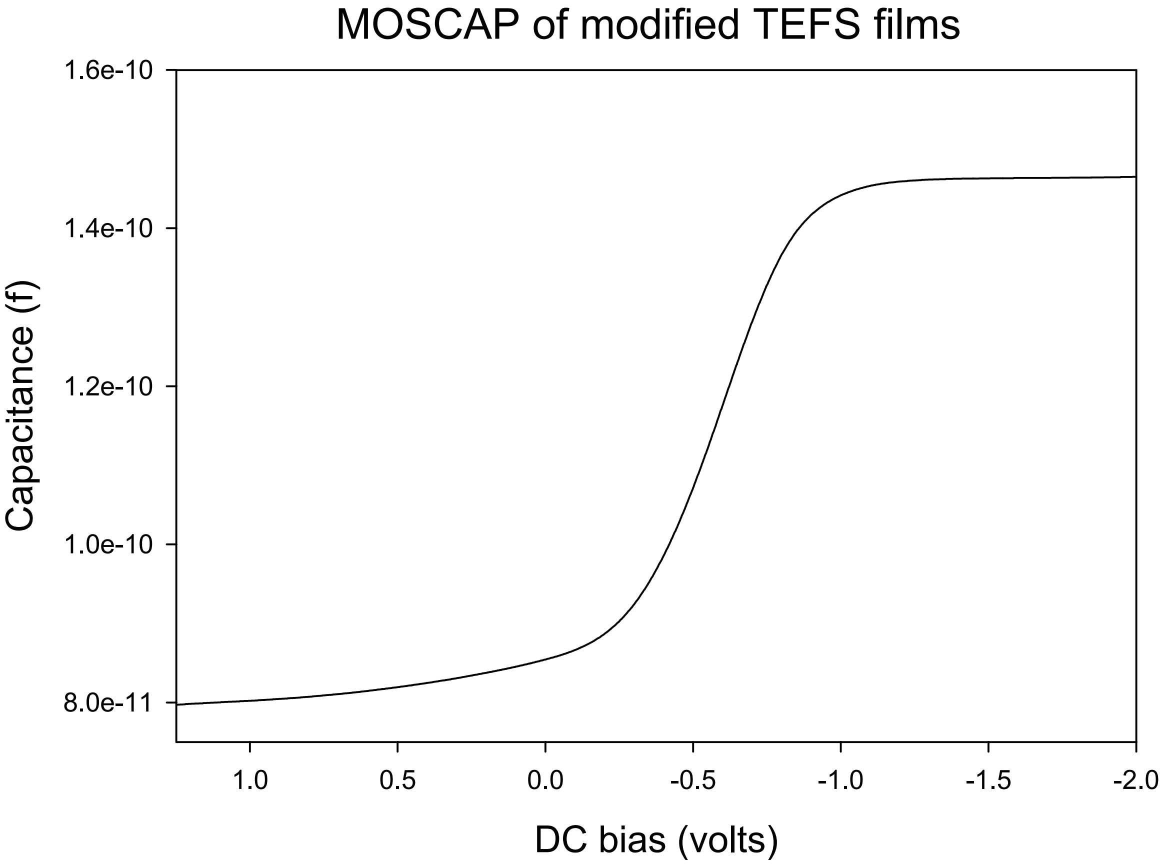

Fig. 46: CV curve for typical TEFS-only or DMDES + TEFS hybrid films.

All CV curves from a MOSCAP structure can be divided into three parts: inversion region, depletion region, and accumulation region. Only the capacitances in the accumulation region were used for k value calculation.

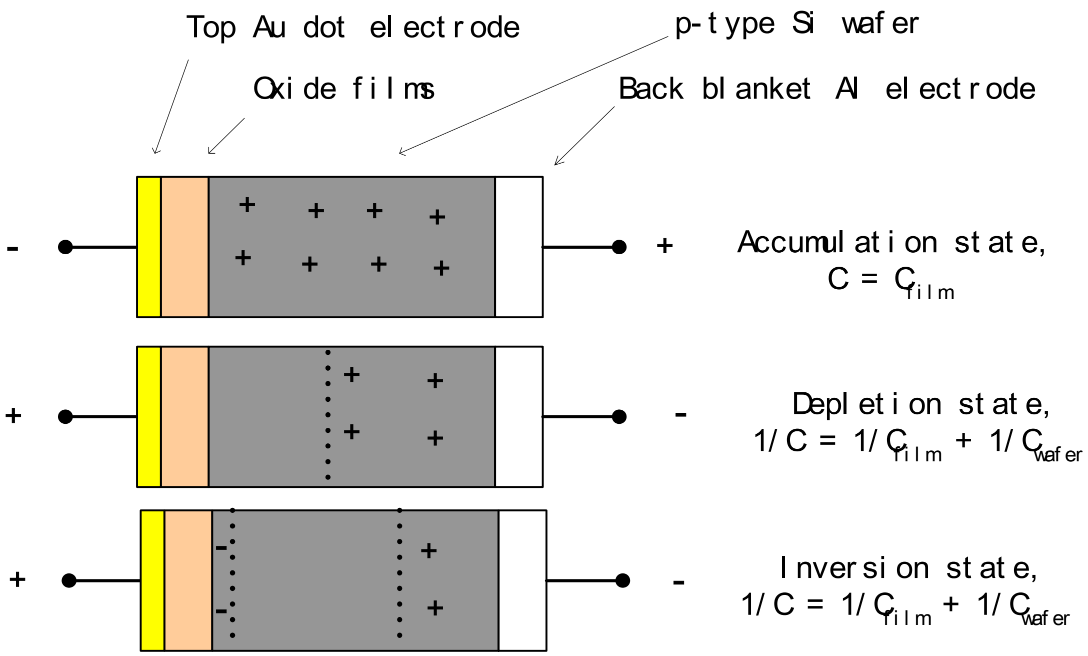

Fig. 47: Reason for capacitance at accumulation region used for insulator dielectric constant calculation

Fig. 47 shows that, only in accumulation state, measured capacitance equals to film capacitance. Therefore, capacitances in the accumulation region were used for k value calculation.

(c) Top dot electrode diameter measurements (SEM).

Top electrode diameters were measured using SEM. The scale bar was calibrated under different magnifications and used as a reference. By inspecting SEM images, it could be found that top electrode had an irregular shape, pinholes, probe scratches during measurement and inclusions. For each diameter, 8 to 12 measurements were averaged and used to calculate error. The biggest error for each dot was used for all samples (± 4.18 %).

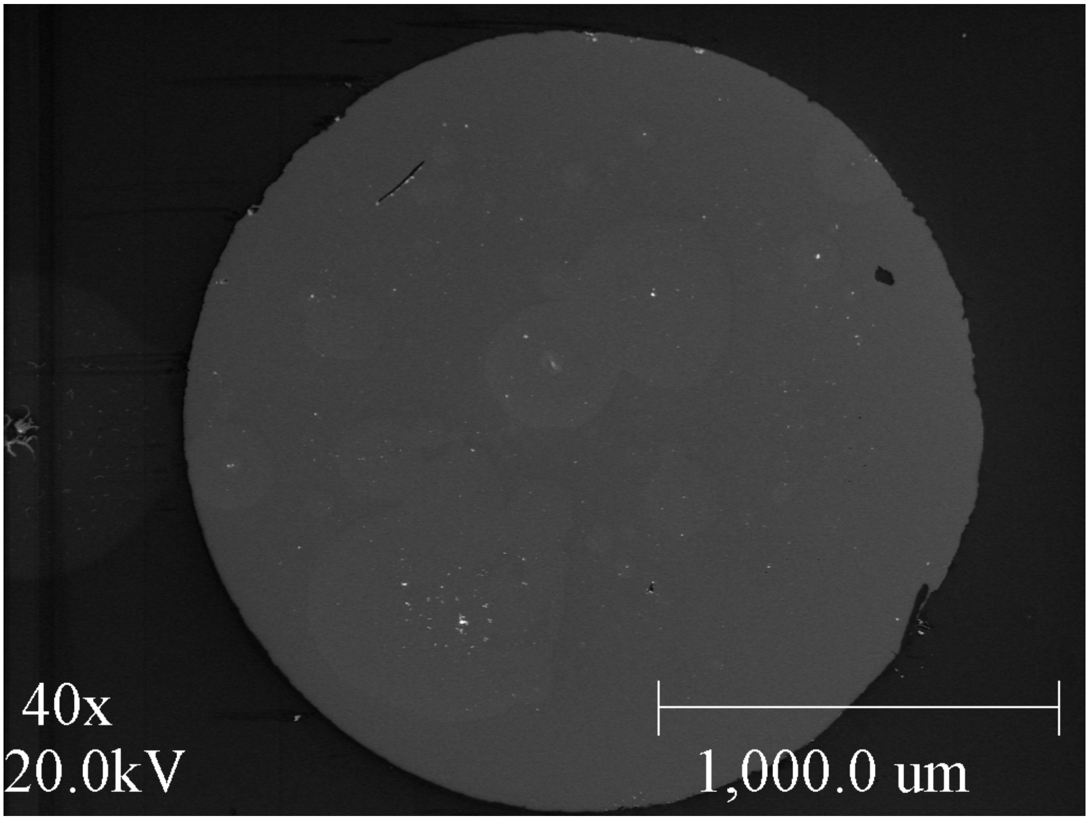

Fig. 48: SEM image of top electrode dot

With all the values measured, calculated k values from equation:

$k = 4 * (C * t_{thickness}) / \varepsilon_0 * \pi * d^2_{dot\ diameter})$

ε_0 is $8.854 * 10^{-12}$ F / m, and π is 3.142.

Results are shown in Fig. 49.

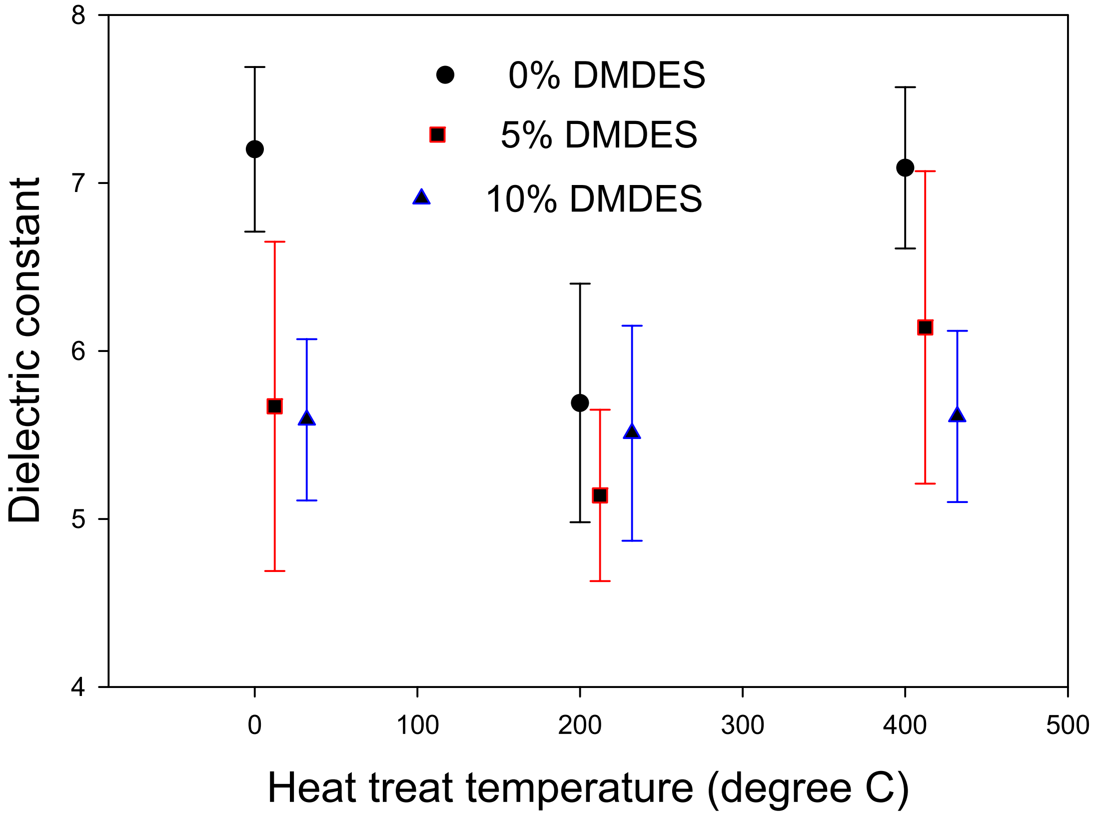

Fig. 49: Calculated dielectric constants for TEFS-only and DMDES + TEFS hybrid films under different heat treatments

All values are higher than expected (ca. 2.3, [13]). We calibrated each measurement step, so we are confident about the measured values. The cause may be from processing. Film thickness was measured before the top electrode metal deposition, but in k value calculation, film thickness was the effective thickness underneath the metal dots. Considering the porous nature of sol-gel films, we suspect that the effective film thickness may shrink due to metal penetration caused by an increase in dielectric constant. (Dot diameter was overwhelmingly larger than thickness, (dot diameter was in mm region and thickness was in several tenths of micron), using an isotropic diffusion model, the effective film thickness reduction effect would be dominant over dot electrode diameter expansion).

We treated TEFS-only samples with 1 volume % hexamethyldisilazane (HMDS) ($(CH_3)_3Si - (NH) - Si(CH_3)_3$) with supercritical CO_2. This process is called silylation

$$2 \equiv Si - OH + (CH_3)_3Si - (NH) - Si(CH_3)_3 = 2\ Si - O - Si(CH_3)_3 + NH_3$$

FTIR spectra of TEFS-only samples before and after silylation were shown in Fig. 50, with them were measured contact angle changes.

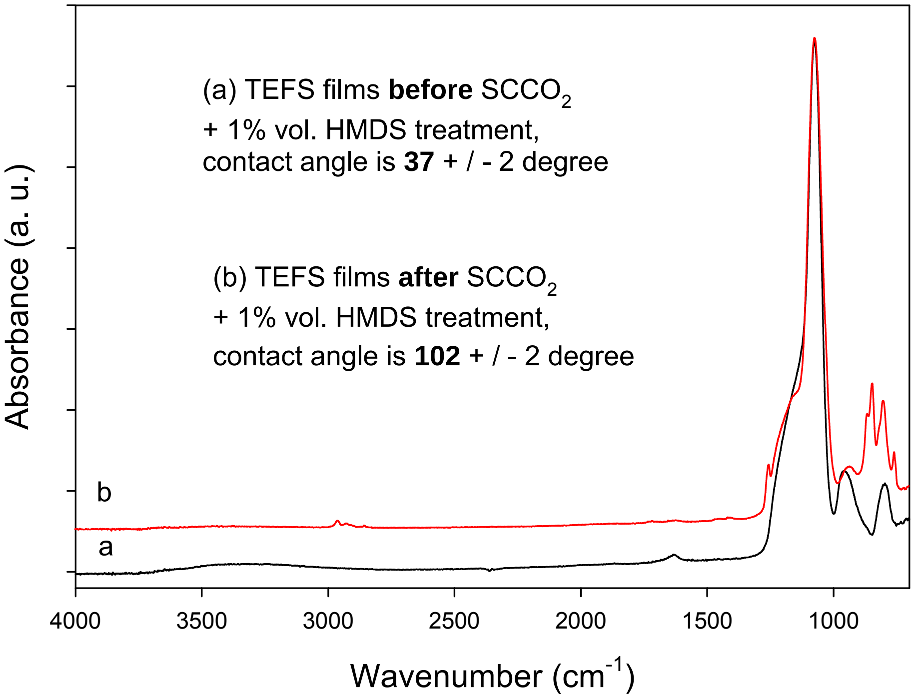

Fig. 50: FTIR spectra of TEFS-only samples before and after silylation and contact angle changes

Table 12: Calculated k values of TEFS-only samples before and after silylation treatment with two different top metal electrodes

calculated k value	before $SCCO_2$	Random error	after $SCCO_2$	Random error
Au dot	7.26	0.67	3.77	0.33
Cu dot	6.13	0.59	3.54	0.31

Silylation added methyl groups onto the silica network, manifested in FTIR spectra with Si – CH_3 peak at 1260 cm^{-1} and C – H peaks at 2990 to 2880 cm^{-1} shown in Fig. 50. The presence of methyl groups reduced water (peaked at 1641 cm^{-1}) and Si – OH bonding (~ 3300 cm^{-1} broad peak).

The decrease in water and Si – OH bonding could result in the decrease in sample dielectric constants. It is unclear what caused the experimental k value decrease after silylation: one possibility is decreased water and Si – OH bonding or methyl group sealing of pores and limiting metal penetration. More experiments are needed.

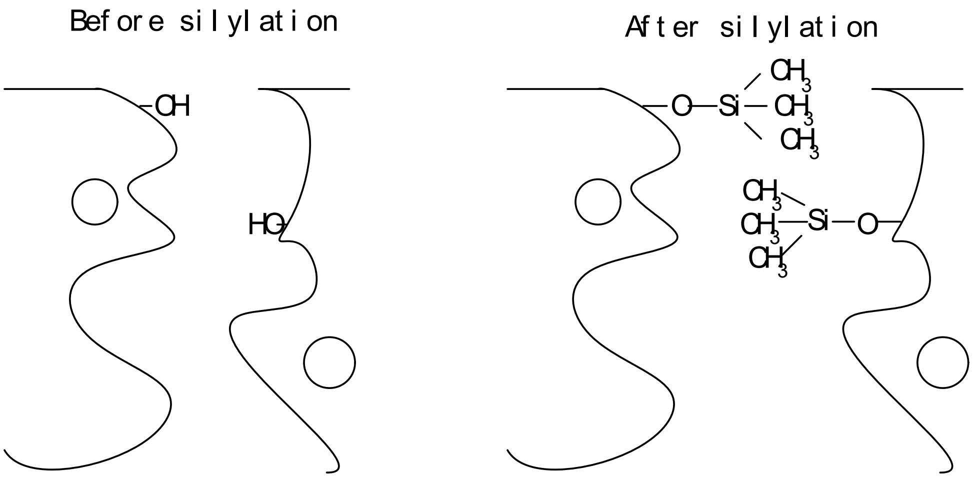

Fig. 51: Pore-sealing effect by silylation modification.

5.4.4 Mechanical Property Measurements

Mechanical properties of low-k dielectrics are critical to survive fabrication processes such as chemical mechanical planarization (CMP) and packaging as well as to device reliability. Porous low-k materials have mechanical properties such as Young's modules (E) and hardnesses (H) values between that of its dense phase and air [61]. E and H were measured by nano indentation on a MTS system using a Berkovich diamond tip.

A schematic of the indentation process is shown in Fig. 52. As the indenter is driven into the material, both elastic and plastic deformation processes occur, producing an impression that conforms to the shape of the indenter to some contact depth, h_c. The radius of the circle of contact is *a*. As the indenter is withdrawn, only the elastic portion of the displacement is recovered, which effectively separates the elastic properties of the material from the plastic.

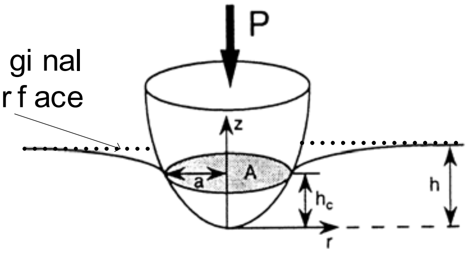

Fig. 52: Schematic representation of nano indentation indenter and sample contact showing various quantities used in analysis [62]

A schematic representation of indentation load (*P*) versus tip penetration depth (*h*) data obtained from one full cycle of loading and unloading is presented in Fig. 54. Important quantities for material E and H subtraction include: peak load (P_{max}), maximum depth (h_{max}), residual depth after unloading (h_f), and the slope of the upper portion of the unloading curve ($S = dP/dh$). The parameter S was defined as the load (P) change rate over penetration depth and is known as contact stiffness. The hardness and elastic modulus are derived from these quantities.

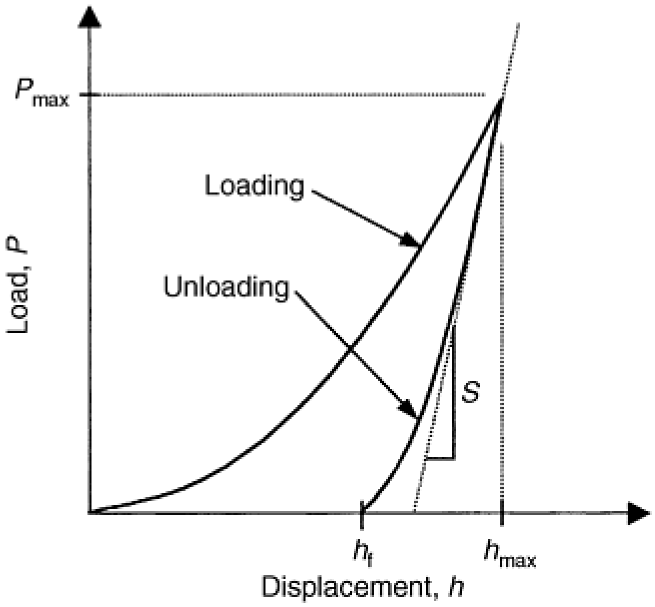

Fig. 53: Loading and unloading load (P) versus surface displacement (h) in a full cycle

The fundamental relations from which H and E are determined are:

$$H = P / A \quad (1)$$

where P is the load and A is the projected contact area at that load, and:

$$E_r = \pi^{1/2} * S / (2 * \beta * A^{1/2}) \quad (2)$$

where E_r is the reduced elastic modulus and β is a constant that depends on the geometry of the indenter [63, 64]. Equation (1) is a working definition for the hardness as measured by indentation testing. By this definition, the hardness is a measure of the load-bearing capacity of the material-tip contact computed by dividing the applied load by the projected area of contact under load. Reduced modulus, E_r, is used in equation (2) to account for the fact that elastic displacements occur in both the indenter and the sample. The elastic modulus of the test material, E, is calculated from E_r using:

$$\frac{1}{E_r} = \frac{1-\nu^2}{E} + \frac{1-\nu_i^2}{E_i} \qquad (3)$$

where v is the Poisson's ratio for the test material, and E_i and v_i are the elastic modulus and Poisson's ratio of the indenter, respectively. For the Berkovich diamond tip, the elastic constant E_i = 1141 GPa and v_i = 0.07. [64] Although Poisson's ratio of the material is needed to compute its modulus, Young's modulus calculation is influenced insignificantly by v_i [65, 66]. Even a rough estimate, say, v = 0.25 ± 0.1, produces only about a 5% uncertainty in the calculated value of E for most materials. β in equation (2) is a constant for the Berkovich diamond tip, β = 1.034 [64, 67].

It is clear that in order to calculate the hardness and elastic modulus from indentation load-displacement data using equation (1) and (2), an accurate measurement of projected contact area under load (A) and elastic contact stiffness (S) is essential. The most widely used method for establishing the contact area and stiffness was developed by Oliver and Pharr [64], which is based on ideas suggested by several others [68 – 70]. The Oliver-Pharr method begins by fitting the unloading portion of the load-displacement data to the power-law relation:

$$P = B^*(h - h_f)^m \qquad (4)$$

where B and m are empirically determined fitting parameters, and h_f is the final displacement after complete unloading, also determined from the curve fit, shown in Fig. 53. The contact stiffness (S) is established by analytically differentiating equation (4) and evaluating the result at the maximum depth of penetration, $h = h_{max}$, that is:

$$S = \left(\frac{dP}{dh}\right)_{h=h_{\max}} = Bm(h_{\max} - h_{\mathrm{f}})^{m-1} \qquad (5)$$

The contact stiffness is graphically determined for E and H subtraction. The next step is to determine the contact depth (h_c), which for elastic contact is less than the total depth of penetration (h_{max}) as illustrated in Fig. 53. The contact depth is estimated using:

$$h_{\mathrm{c}} = h - \varepsilon \frac{P}{S} \qquad (6)$$

where ε is a constant that depends on the indenter geometry. For Berkovich indenters ε = 0.75 [64, 71]. The projected contact area is calculated by evaluating an empirically determined indenter area function $A = f(d)$ at the contact depth h_c; that is:

$$A = f(h_c) \qquad (7)$$

The area function, $A = f(d)$, also known as the shape function or tip function, relates the cross-sectional area of the indenter (A) to the distance (d) from its tip. Usually it is stimulated by indenting a fused silica reference standard.

Once the projected contact area and contact stiffness are known, E and H can be calculated from equations (1) and (2).

For our samples, E and H were averaged over about 9 to 25 individual penetrations using Nanoindenter® XP from MTS Systems Corp. with Berkovich diamond tip and TestWorks® 4 software interface. The Indenter was driven to penetrate samples at constant strain rate (0.05 sec^{-1}). One penetration is shown in Fig. 54.

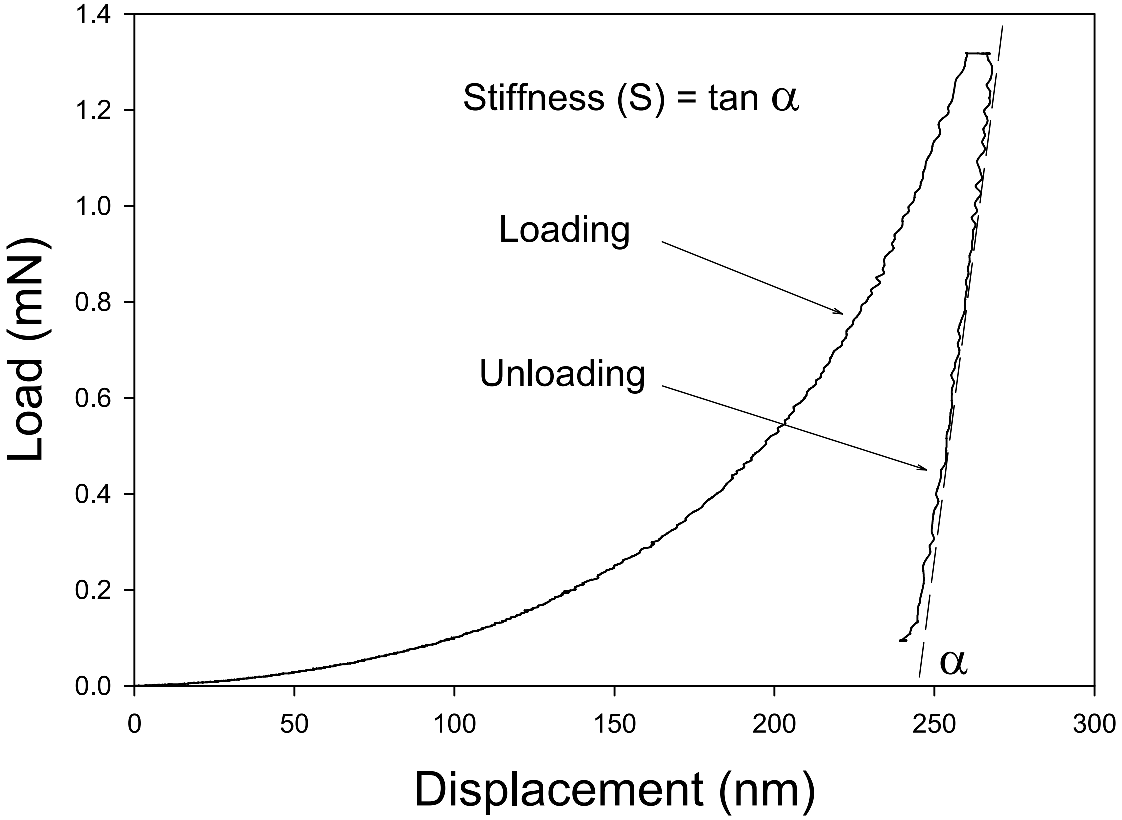

Fig. 54: One cycle of loading unloading versus surface displacement

Calculated E and H values for each individual penetration are in Fig. 55 and Fig. 56.

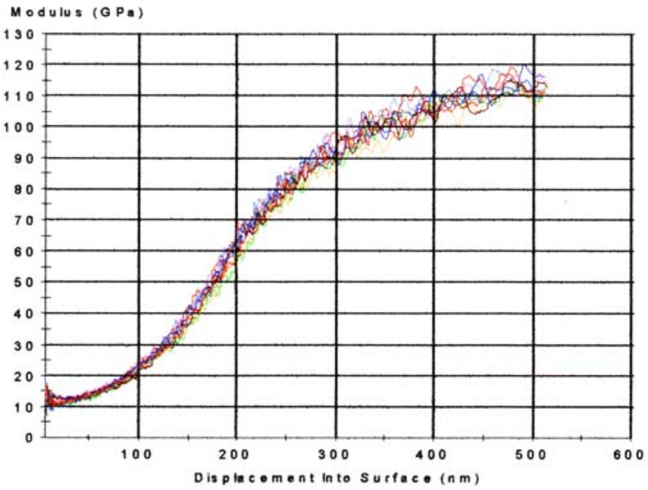

Fig. 55: Calculated E versus surface displacement in each individual penetration

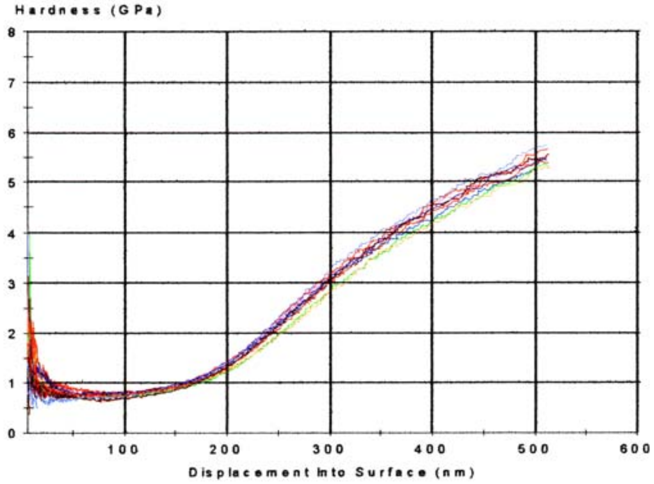

Fig. 56: Calculated H versus surface displacement in each individual penetration

In E and H calculations, both curves had an increased modulus or hardness at very shallow depths. This phenomenon is not yet well understood. Several explanations have been proposed: indentation size effects [72]; material surface overshoot; or a real change in surface composition [73]. But convention holds that this minimum plateau can be used as the best estimate for low-k film mechanical properties

[74]. Minimum values occurred in E calculations from 70 Å to 100 Å and in H calculations from 250 Å to 400 Å. So E and H values for our samples were taken from 70 Å to 100 Å and from 250 Å to 400 Å, respectively. (Total film thickness is about 2500 to 4000 Å, thickness we used for E and H values was less than 10% of film thickness to avoid surface and substrate effects). E and H measurement results are summarized in Fig. 57 and Fig. 58.

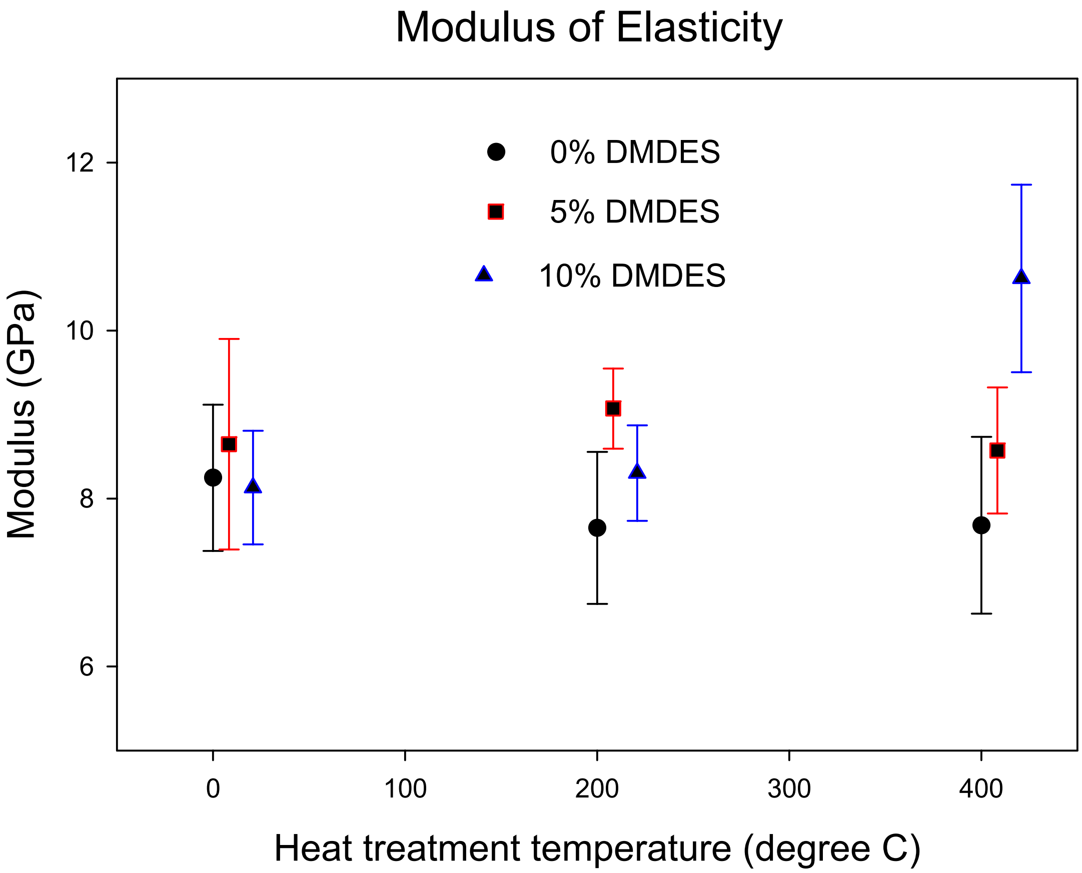

Fig. 57: Elastic modulus change with compositions and heat treatments

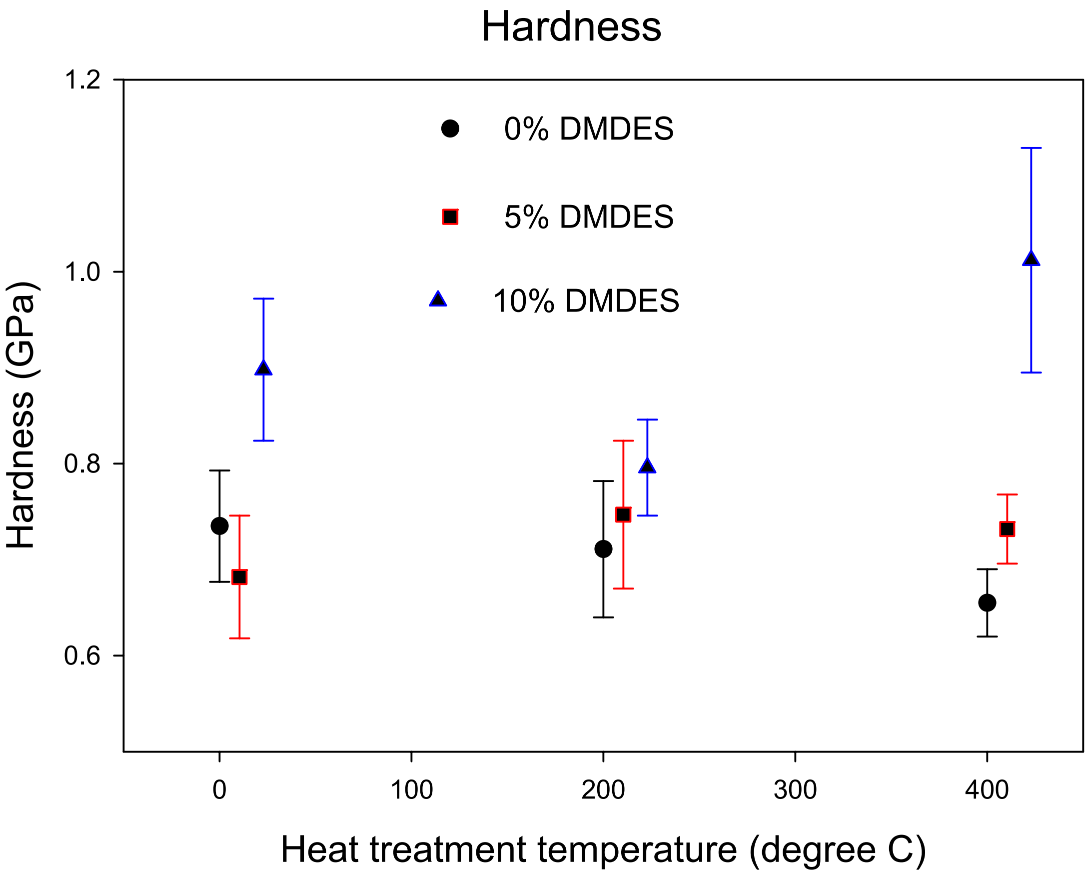

Fig. 58: Hardness change with compositions and heat treatments

The values in Fig. 57 and 58 are lower than previously reported for TEFS [13]. Differences may be due to slightly different instrumental configurations or, more likely, due to different processing of the films. In previous work, the aging times were 30 minutes while in this study the aging times were around five minutes.

Porosity calculated from the Lorentz-Lorenz relation:

$$\frac{(N_f^2-1)}{(N_f^2+2)} = (1-v_p)\frac{(N_s^2-1)}{(N_s^2+2)} + v_p\frac{(N_p^2-1)}{(N_p^2+2)}$$

has been used to compare modulus results in Fig. 59.

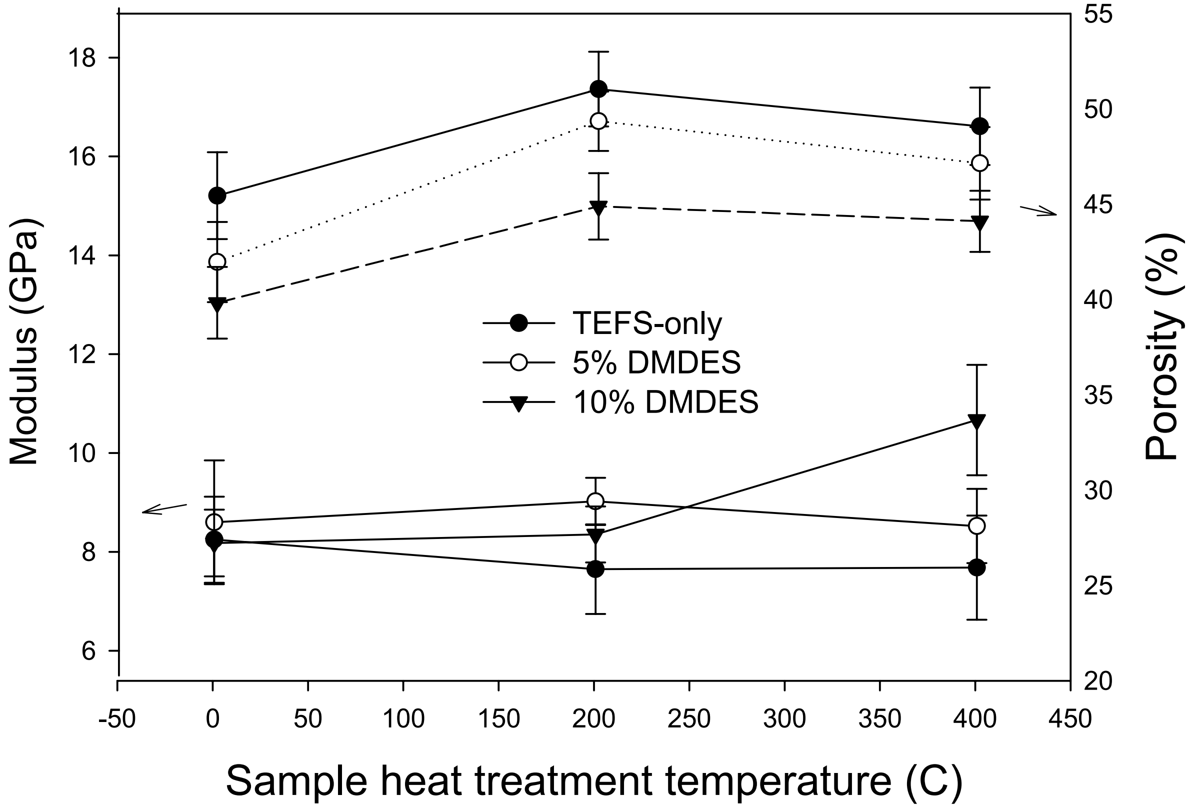

Fig. 59: Modulus and porosity change with sample compositions and thermal treatments

In ^{29}Si solid state NMR, it was found that Si – CH_3 segments introduced by DMDES were delocalized. [58, 74, 75] This fast network segmental motion could relax silica network, lead to lower porosity. After 400°C for one hour, some lost Si – CH_3 bonds may be changed to Si – O – Si bonding, further strengthening the matrix. So little increase in E and H in 10% DMDES + TEFS films at 400°C was observed.

5.5 References

1. R.H. Glaser, G.L. Wilkes, and C.E. Bronnimann, J. Non-Cryst. Solids, 113 (1989) 73.
2. S.E. Rankin, C.W. Macosko, and A.V. McCormick, IChE journal, 44 (1998) 1141.
3. Y. Sugahara, S. Okada, K. Kuroda, and C. Kato, J. Non-Cryst. Solids, 139 (1992) 25.
4. Y. Sugahara, S. Okada, S. Sato, K. Kuroda, and C. Kato, J. Non-Cryst. Solids, 167 (1994) 21.
5. H. Schmidt, H. Scholze, and A. Kaiser, J. Non-Cryst. Solids, 63 (1984) 1.
6. R.J. Hook, J. Non-Cryst. Solids, 195 (1996) 1.
7. T.M. Alam and M. Henry, Physical Chemistry Chemical Physics, 2 (2000) 23.
8. L.V. Ng, and A.V. McCormick, J. Phys. Chem., 100 (1996) 12517.
9. C.A. Fyfe, and P.P. Aroca, Chem. Mater., 7 (1995) 1800.
10. J. Sanchez, S.E. Rankin, and A.V. McCormick, Materials and Interfaces, 35 (1996) 117.
11. J.C. Pouxviel, J.P. Boilot, J.C. Beloeil, and J.Y. Lallemand, J. Non-Cryst. Solids, 89 (1987) 345.
12. J.K. West, L.L. Hench, B. Zhu, and Y.C. Cheng, J. Non-Cryst. Solids, 121 (1986) 51.
13. B.P. Gorman, R.A. Orozco-Teran, J.A. Roepsch, H. Dong, D.W. Mueller, R.F. Reidy, App. Phys. Lett., 79 (2001) 4010.
14. J.A. Roepsch, MS Thesis, Dept. Mater. Sci., Univ. North Texas, 2001.

15. Z. Zhang, H. Dong, B.P. Gorman, C. Yao, D.W. Mueller, and R.F. Reidy, Electrochem. Soc., (2003) 170.
16. J.K. Hong, H.S. Yang, M.H. Jo, H.H. Park, and S.Y. Choi, Thin Solid Films, 308–309 (1997) 495.
17. P. Innecenzi, J. Non-Cryst. Solids, 316 (2003) 309.
18. P.N. Sen, and M.F. Thorpe, Phys. Rev. B, 15 (1977) 4030.
19. F.L. Galeener, Phys. Rev. B, 19 (1979) 4292.
20. F.L. Galeener, A.J. Leadbetter, and M.W. Stringfellow, Phys. Rev. B, 27 (1983) 1052.
21. C.T. Kirk, Phys. Rev. B, 38 (1988) 1255.
22. T.M. Parrill, J. Mater. Res., 7 (1992) 2230.
23. T. Chia, J.K. West, and L.L. Hench, Mat. Res. Symp. Proc., Vol. 346 (1994) 727.
24. C.Y. Wang, Z.X. Shen, and J.Z. Zheng, App. Spec., 54 (2000) 209.
25. J.R. Martinez, F. Ruiz, Y.V. Vorobiev, F. Perez-Robles, and J. Gonzalez-Hernandez, J. Chem. Phys., 109 (1998) 7511.
26. T. Usami, K. shimokawa, and M. Yoshimaru, Jpn. J. App. Phys., 33 (1994) 408.
27. H. Kitoh, M. Muroyama, M. Sasaki, M. Iwasawa, and H. Kimura, Jpn. J. App. Phys., 35 (1996) 1464.
28. M. Yoshimaru, S. Koizumi, and K. Shimokawa, J. Vac. Sci. Technol. A, 15(6) (1997) 2908.
29. T.M. Duncan, D.C. Douglass, R. Csencsits, and K.L. Walker, J. App. Phys., 60 (1986) 1.

30. M. Yoshimaru, S. Koizumi, and K. Shimokawa, J. Vac. Sci. Technol. A, 15(6) (1997) 2915.
31. Y. Nakasaki, J. Soc. App. Phys., (1992) 589.
32. C. Kaneta, J. Soc. App. Phys., (1995) 591.
33. S.M. Han, and E.S. Aydil, J. Vac. Sci. Technol. A, 15(6) (1997) 2893.
34. M.K. Bhan, J. Huang, and D. Cheung, Thin Solid Films, 308-309 (1997) 507.
35. V.V.S. Rana, M. Bhan, A. Gupta, S. Hong, and P. Lee, Mat. Res. Soc. Symp. Proc., Vol. 476 (1997) 239.
36. G. Lucovsky, and H. Yang, J. Vac. Sci. Technol. A, 15(3) (1997) 836.
37. H. Yang, and G. Lucovsky, Mat. Res. Soc. Symp. Proc., Vol. 476, (1997) 273.
38. H. Yang, and G. Lucovsky, Mat. Res. Soc. Symp. Proc., Vol. 511, (1998) 371.
39. B. Campostrini, M. Ischia, G. Carturan, and L. Armelao, J. Sol Gel Sci. Technol., 23 (2002) 107.
40. S. Mizuno, A. Verma, H. Tran, P. Lee, and B. Nguyen, Thin Solid Films, 283 (1996).
41. S. W. Lim, Y. Shimogaki, Y. Nakano, K. Tada, and H. Komiyama, Jpn. J. App. Phys., 35 (1996) 1468.
42. J. Lubguban, Jr., Y. Kurata, T. Inokuma, and S. Hasegawa, J. App. Phys., 87 (2000) 3715.
43. Y. Kim, M.S. Hwang, H. J. Kim, J.Y. Kim, and Y. Lee, J. App. Phys., 90 (2001) 3367.
44. S.M. Han, and E.S. Aydil, J. App. Phys., 83 (1998) 2172.

45. K. Mosig, T. Jacobs, P. Kofron, M. Daniels, K. Brennan, A. Gonzales, R. Augur, J. Wetzel, R. Havemann, and A. Shiota, Proc. of IEEE 2001 Inter. Inter. Technol. Conf., 2001, 292.
46. D. Smith, MRS meeting, Low-k Dielectric Symposium, April 16-20, 2001.
47. H. Dong, B.P. Gorman, Z. Zhang, R.A. Orozco-Teran, M.J. Kim, D.W. Dennis, and R.F. Reidy, 7th Intl. Symp. Aerogel, Alexandria, Virginia, Nov. 2003 (poster).
48. J.C. Alonso, E. Pichardo, V. Pankov, and A. Ortiz, J. Vac. Sci. Technol. A, 18 (2000) 2827.
49. H.G. Tompkins, and P.W. Deal, J. Vac. Sci. Technol. B, 11 (1993) 727.
50. J. Gallardo, P. Galliano, and A. Duran, J. Sol Gel Sci. Technol. 19, 393 (2000)
51. D.R. Denison, J.C. Barbour, and J.H. Burkhart, J. Vac. Sci. Technol. A, 14 (1996) 1124.
52. H. Dong, R.A. Orozco-Teran, J.A. Roepsch, D.W. Mueller, and R.F. Reidy, Proc. Thin Film Materials, (Electrochemical Society) 2001.
53. Z. Zhang, B.P. Gorman, H. Dong, Rosa A. Orozco-Teran, D.W. Mueller, R.F. Reidy, J. Sol Gel Sci. Technol., 28 (2003) 159.
54. E.P. Barrett, L.G. Joyner, and P.P. Halenda, J. Am. Chem. Soc., 73 (1951) 373.
55. J. Klein, and E. Kumacheva, Physica A, 249 (1998) 206.
56. S.K. Mah, and I.J. Chung, J. Non-Cryst. Solids, 183 (1995) 252.
57. F. Babonneau, L.Bois, and J. Livage, J. Non-Cryst. Solids, 147&148 (1992) 280.
58. J. Brus, and M. Skrdlantova, J. Non-Cryst. Solids, 182 (2001) 61.
59. A. Benninghoven, J. Giber, J. Laszlo, M. Riedel, and H.W. Werner, Secondary Ion Mass Spectrometry (III), page 172 – 185.

60. C.M. Herzinger, P.G. Snyder, B. Johs, and J.A. Woollam, J. App. Phys., 77 (1995) 1715.
61. C. Jin, S. Lin, and J.T. Weztel, J. Electron. Mater., 30 (2001) 284.
62. G.M. Pharr, Mater. Sci. & Engineering A, 253 (1998) 151.
63. S.I. Bulychev, V.P. Alekhin, M.Kh. Shorshorov, A.P. Ternovskii, and G.D. Shnyrev, Zavod. Lab., 41 (1975) 1137.
64. W.C. Oliver, and G.M. Pharr, J. Mater. Res., 7 (1992) 1564.
65. X. Jiang, K. Reichelt, and B. Stritzker, J. App. Phys., 66 (1989) 5805.
66. L. Shen, K. Zeng, Y. Wang, B. Narayanan, and R. Kumar, Microelectron. Engineering, 70 (2003) 115.
67. R.B. King, Int. J. Solids Struct., 23 (1987) 1657.
68. W.C. Oliver, MRS Bull., 11 (1986) 15.
69. J.L. Loubet, J.M. Georges, O. Marchesini, and G. Meille, J. Tribology (Trans. ASME), 106 (1984) 43.
70. M.F. Doerner and W.D. Nix, J. Mater. Res., 1 (1986) 601.
71. A. Bolshakov, W.C. Oliver, and G.M. Pharr, MRS Symp. Proc., Vol 356, (1995) 675.
72. G.M. Pharr, and W.C. Oliver, J. Mater. Res., 4 (1989) 94.
73. J.B. Wella, I.S. Adhihetty, K, Junker, and A.A. Volinsky, Int. J. Fract., 119/120 (2003) 487.
74. A.B. Seddon, IEE Proc. -Circuits Devices Syst., 145 (1998) 369.
75. F. Babonneau, V. Gualandris, and M. Pauthe, MRS Proc., vol. 435 (1996) 119.

CHAPTER 6

CONCLUSIONS

DMDES hydrolysis and condensation at R = 4, r = 4 and 0.01 M HCl catalyst were analyzed by liquid ^{29}Si NMR. Linear species (i.e., monomers, dimers, trimers) and cyclic species (i.e., three-membered and four-membered rings) were identified. During the initial time period, fully hydrolyzed monomer (D_0^2), partially hydrolyzed monomer (D_0^1) and unhydrolyzed monomer (D_0^0) coexisted in solution. After about an hour, all unreacted monomer (D_0^0) was consumed. Dimers (D_1) dominated for over seventeen hours while longer linear species and ringed moieties began to form. After twenty-four hours, DMDES hydrolysis and condensation reactions produced mainly C_4 structures. From seventeen to twenty-four hours, C_4 formation resulted from dimer-dimer reactions. Other mechanisms are deemed less likely because during that time span the system lacked monomers for monomer-trimer reactions.

Introducing DMDES reaction products into a TEFS silica network improved hydrophobicity and decreased average pore size. Linear species from DMDES linked onto the TEFS silica network and made the film hydrophobic. Based on FTIR results which show a decrease in Si-OH groups, we believe that the linear species bridge between TEFS silanols. This slight densification is reflected in ellipsometry results. Cyclic species from DMDES were hoped to function as nano-templating agents; however, these species appeared to create larger scaled voids than anticipated. We believe that individual C_4 species or clusters of C_4 prevent gelation in their intermediate vicinity by repelling water and create voids in which hydrolysis is limited.

To benefit from both linear and cyclic species from DMDES hydrolysis and condensation, DMDES must be pregelled. While DMDES will not form a gel individually, a reaction period will permit formation of desired products. Introducing these DMDES products will decrease TEFS concentration because the ratio of solvent (EtOH) to silicon (from both DMDES and TEFS) is maintained (R = 15). From FTIR spectra, increasing DMDES concentration increased Si – CH_3 peak intensity but decreased the Si – F peak intensity. Both hydrophobicity (Si – CH_3) and robustness (Si – F) are desirable for low-k applications. At 35 – 45 mole percent DMDES, Si – CH_3 and Si – F peak intensities were comparable in FTIR spectra. By maintaining the DMDES concentration at 35 mole percent but changing DMDES pregel time (t), S – CH_3 peak intensity increased considerably when t was zero (i.e., addition of unreacted DMDES) to about two hours. A weaker increase was observed for two to about six hours, but the methyl intensity decreased when t was longer than six hours. This is because at different pregel times, the DMDES system has fractions of monomers, dimers, trimers, and larger species (based on NMR spectra), and each species can have different interactions with the TEFS-based network. Therefore, the DMDES pregel time was set to four to six hours. However, sols with 35 mole percent of DMDES are not spinnable due to phase separation. Cyclic species from DMDES are nonpolar and immiscible in water (water is needed for TEFS hydrolysis). To create viable spin-on hybrid low-k films, DMDES concentration was decreased to 10 mole percent, and DMDES pregel time was set to four to six hours.

The hybrid film properties were compared to TEFS film properties determined by contact angle, thermal stability, modulus (E), hardness (H), and dielectric constant measurements.

Hybrid films have higher contact angle (i.e., higher hydrophobicity) due to Si–CH_3 groups introduced by DMDES linear species. Both hybrid and TEFS films were annealed in air, oxygen, and nitrogen environments. FTIR results showed a loss in methyl groups and water after annealing. TGA analysis exhibits two regions:

- room temperature to 200°C where mainly ethanol and water outgas, and
- 200°C to 400°C where proximal silanols condense forming silloxanes and the condensation product EtOH is given off.

DMDES incorporation impacts the dielectric constant of TEFS films. Due to the porous nature of a xerogel film, deposited metal may penetrate into pores during electrode dot deposition. Dielectric constant values decreased in capacitor structures if the films were silylated with HMDS prior to metal deposition. FTIR results showed considerable SiOH and water peak intensity decreases in the silylated films. It is not clear if the k value decrease resulted from pore sealing or from the replacement of OH groups with trimethyl silyls. By changing the top electrode metal from gold to copper, the decrease in dielectric constant was different. The differences may come out of metal diffusivity difference because film conditions are identical.

Mechanical properties for both TEFS and hybrid films were measured by nanoindentation and analyzed using the Oliver and Pharr method. [1] Curves for E and H versus indentor penetration showed an increase at very shallow depth, followed by a plateau. To minimize surface effects, E and H values were averaged between penetration depths at the plateau region and less than 10% of film thickness. Hybrid films showed a little increase in E and H values, especially after 400°C annealing. This mechanical enhancement was attributed to:

- Si – CH_3 segments introduced by DMDES relaxed silica network, leading to lower porosity and higher strength.
- After 400°C annealing, lost Si – CH_3 bonds may be changed to Si – O – Si bonding and strengthen films.

However, absolute E and H values in this study are lower than published for TEFS film. Published TEFS mechanical properties (E and H) were measured using continuous stiffness mode (CSM) reference but in this study, they were measured using dynamic stiffness mode (DSM). Testing equipment is not the same nor is the analysis software. In addition, film processing is quite different. However, E and H for both TEFS and hybrid films in this study were measured and analyzed under identical conditions. Conclusions based on their relative magnitudes can be justified.

1. W.C. Oliver, and G.M. Pharr, J. Mater. Res., 7 (1992) 1564

.

CHAPTER 7

FUTURE WORK

Average pore size diameter and pore size distribution are critical to low-k film applications. Average pores size will affect a film's mechanical properties. Combining pore size measurements from SAW (surface acoustic wave) or SAS (small angle x-ray or neutron scattering) with mechanical properties may explain their interdependence.

In this study, DMDES hydrolysis and condensation products were used as structural modifiers. It would be interesting to introduce hydrophobicity via DMDES monomer, D_1, and to create voids from C_4 moieties. Comparing resulting pore properties and mechanical properties will give more insight in nano templeting behavior and pore size-mechanical property relations.

During heating hybrid films showed structural and compositional changes. It is desirable to measure the structural changes (in situ FTIR) and compositional changes (measuring outgas by mass spectrometry).

HMDS silylation reduced the dielectric constant through reaction with –OH groups. In the experiments to limit metal penetration, work could be done to distinguish between pore sealing effects and OH removal such as changing functional group length (replacing triethylchlorosilane, tributylchlorosilane for HMDS). Near surface pore size changes in the film could be examined after metal deposition by TEM.